CENTRO DE INVESTIGACIÓN Y DE ESTUDIOS AVANZADOS DEL INSTITUTO POLITÉCNICO NACIONAL

UNIDAD ZACATENCO

PROGRAMA DE DOCTORADO EN
NANOCIENCIAS Y NANOTECNOLOGÍA

Remoción de metales pesados en fase acuosa mediante nanocompuestos de TiO_2 / óxidos de hierro

T E S I S

Que presenta

MERCYRANI BABUDURAI

Para obtener el grado de

Doctorado en Ciencias
En Nanociencias y Nanotecnología

Director de la Tesis

Dr. Velumani Subramaniam

Ciudad de México Marzo 2021

CENTER FOR RESEARCH AND ADVANCED STUDIES OF THE NACIONAL POLYTECHNIC INSTITUTE

UNIT ZACATENCO

DOCTORAL PROGRAM OF
NANOSCIENCES AND NANOTECHNOLOGY

Heavy metal removal in aqueous phase using TiO_2/Iron-oxidenanocomposites

T H E S I S

presented by

MERCYRANI BABUDURAI

To obtain the grade of

Doctorate in Science

In Nanoscience and Nanotechnology

Thesis Director

Dr. Velumani Subramaniam

Mexico City, Mexico March 2021

ABSTRACT

One of the most significant challenges of this century is providing safe drinking water. The dyes and heavy metals contamination in drinking water resulting from industrialization and urbanization is a global concern. Nanotechnology provides an effective way to remove the toxic contaminants within a cost-framework. Therefore, this study has been dedicated to studying nano-adsorbents and nano-photocatalysts to remove both inorganic and organic pollutants from water to reach more efficient water treatment. In this work, the tetragonal TiO_2 anatase and cubic iron oxide nanomaterials were synthesized through the co-precipitation and sol-gel methods. The synthesized nanomaterials were used to form TiO_2/Iron-oxide nanocomposites, and it is used to remove the dye and heavy metals in water with the advantage of magnetic separation. To extend the photocatalytic activity of TiO_2 to the visible spectrum, its bandgap must be decreased that suppresses the recombination reactions. Hence, TiO_2/Fe_3O_4 (T/M) NCs, with three different ratios (0.2/0.8, 0.5/0.5, and 0.8/0.2) was synthesized by the ultrasonication method. Our studies showed that $(TiO_2)_{0.2}(Fe_3O_4)_{0.8}$ NCs, having a small crystallite size and bandgap, gave the best photocatalytic activity under visible light. However, it does not show any activity for arsenic; hence, the TiO_2/Iron oxide NCs synthesized using the ball-milling route were used to study the adsorption of arsenic. This resulted in a non-toxic, low-cost, and easily accessible method for synthesizing NCs in large quantities for adsorption, with promising results for arsenic species removal from water.

The ball-milling synthesis provides a comparatively cost-effective strategy and for modulating the properties of nanostructured materials. The milling time and ball-to-powder (BPR) ratio variations allowed modifying the T/M NCs properties during the synthesis. The enhanced performances obtained for the NCs of anatase TiO_2 and γ-Fe_2O_3 with the most intense phase peak ratio ($I_{(101)}/I_{(311)}$) was 1.2. To achieve the WHOs maximum contamination limit (MCL), a methodical adsorption study was performed by optimizing the different parameters that affect arsenic removal (pH, dosage, initial As concentration, and time). Adsorption studies using the optimized conditions (8 g/L adsorbent dosage, 15 minutes contact time, and 4.0 pH value) produced 100% of arsenic (III) and (V) removal, suggesting the synthesized nanomaterial as perfect for water treatment. The synthesized materials also offered reusability potentials and magnetic separation, making them more economical than competing adsorption techniques and materials.

Keywords: Adsorption, photocatalysis, ultrasonication, ball milling, orange G, arsenic, nano-photocatalyst, nano-adsorbent, TiO_2/Iron oxide NCs, magnetic separation.

RESUMEN

Uno de los desafíos más significativos de este siglo es el suministro de agua potable. La contaminación por colorantes y metales pesados en el agua potable, resultante de la industrialización y la urbanización es una gran preocupación a nivel mundial. La nanotecnología proporciona una forma eficaz de eliminar los contaminantes dentro de un esquema asequible. Por tanto, el presente estudio se ha dedicado a estudiar nano-adsorbentes y nano-fotocatalizadores para eliminar contaminantes tanto inorgánicas como orgánicas, para alcanzar un tratamiento de aguas más eficiente. En este trabajo se sintetizaron nanomateriales tetragonales de óxido de titanio (TiO_2) anatasa y óxido de hierro cúbico (Fe_3O_4) mediante el método de co-precipitación y el método sol-gel. Los nanomateriales obtenidos se utilizaron para formar nanocompositos (NC) de TiO_2 / Fe_3O_4 utilizando el método de molienda de bolas y ultrasonido. Los NC obtenidos se utilizaron para eliminar colorantes y metales pesados en agua, con la ventaja que implica su sencilla separación magnética. Es bien conocido que para extender la actividad fotocatalítica del TiO_2 al espectro de luz visible se debe disminuir su energía de banda prohibida y ralentizar la recombinación de los portadores de carga fotogenerados. Por lo tanto, en este trabajo se sintetizaron los NC de TiO_2 / Fe_3O_4 con tres proporciones diferentes (0.2 / 0.8, 0.5 / 0.5 y 0.8 / 0.2). El ensayo de degradación del colorante naranja G fue llevado a cabo dentro de un simulador solar bajo diferentes tiempos de exposición utilizando los tres nanocompuestos sintetizados. Los resultados mostraron que, de entre las otras proporciones, el nanocomposito $(TiO_2)_{0.2}(Fe_3O_4)_{0.8}$ con tamaño de cristalito pequeño y bajo valor de banda prohibida exhibió la mejor actividad fotocatalítica bajo luz visible. Pero no muestra actividaa para el arsénico, por lo tanto, NC de TiO_2 / óxido de hierro sintetizados mediante molienda mecánica se utilizaron para estudiar la adsorción de especies de arsénico.

La formación de NC mediante molienda mecánica representa un método no tóxico, de bajo costo y de fácil acceso para sintetizar NC en grandes cantidades, los cuales ofrecen resultados prometedores para la eliminación de arsénico del agua. Los estudios de adsorción que utilizaron las diversas relaciones TiO_2 / γ-Fe_2O_3 (T/M) muestran rendimientos variables. Los rendimientos más altos fueron obtenidos para el NC de anatasa TiO_2 y γ-Fe_2O_3 con la relación de pico de fase más intensa (I $_{(101)}$ / I $_{(311)}$) de 1.2. La eliminación de As (III) y As (V) utilizando los NC sintetizados confirma que la técnica de molienda de bolas puede producir nanomateriales con propiedades deseables para fines de adsorción. Para alcanzar el límite máximo de contaminación (MCL) marcado por la organización mundial de la salud (WHO), se realizó un estudio metódico de adsorción optimizando los diferentes parámetros que afectan la remoción de arsénico (pH, dosis, concentración y tiempo). Los estudios de adsorción que utilizaron la proporción y las condiciones optimizadas (dosis de adsorbente de 8 g/L, tiempo de contacto de 15 minutos y valor de pH de 4.0) produjeron una eliminación de cerca del 100% de arsénico (III) y arsénico (V), lo que sugiere que el nanomaterial sintetizado es ideal para el tratamiento del agua contaminada con este metaloide. Los materiales sintetizados también ofrecen posibilidades de reutilización y separación magnética, lo que los hace más económicos que las técnicas y materiales de adsorción más comúnmente empleados.

Palabras clave: Adsorción, fotocatálisis, ultrasonido, molienda de bolas, Orange G, arsénico, nano-fotocatalizador, nano-adsorbente, nanocompositos de TiO_2 / óxido de hierro, separación magnética.

ACKNOWLEDGEMENT

First and foremost, I would like to thank God, the almighty, who has granted this opportunity and strength to accomplish the thesis. I extend my sincere gratitude to my research supervisor Prof. Dr. Velumani Subramaniam, for his constant support, valuable suggestions, encouragement, guidance, motivation, and advice throughout my Ph.D. journey. I also express gratitude to my committee members Dr. Arturo Maldonado Alvarez, Dr. Mauricio Ortega Lopez, Dr. Juan Carlos Duran Alverez, Dra. Maria de la Luz Olvera and Dr. Miguel Garcia Rocha, for their valuable suggestions, motivation, and guidance throughout the work.

I would like to thank CINVESTAV-IPN (Centro de Investigación y de Estudios Avanzados del Instituto Politécnico Nacional) and Nanoscience and nanotechnology program; without the institution, the work will be impossible. I would like to thank Consejo Nacional de Ciencia y Tecnologia (National Council of Science and Technology, CONACyT-Mexico) for providing the financial support from the CONACYT-SENER 263043 project SEP-CINVESTAV-200.

I wish to thank Dr. Jose Gerardo Cabanas Moreno for his complete support throughout the Ph.D. program. I also like to express my gratitude to Jaime Santoyo Salazar, Francisco Alvarado Cesar, and Miguel A. Avendaño Ibarra from CINVESTAV-IPN for TEM, SEM, and RAMAN characterizations and Lazaro Huerta from UNAM for helping me with XPS analysis. I convey my thanks to Alma Mercedes Zamudio Martínez and Roxana Yasmin De Lorentz for helping me in various documentation works.

I wish to thank MREB (Materials for Renewable Energy and Biomedical Applications) group members (Dra. Araceli Romero Nunez, Dra. Myriam Solis Lopez, Dr. Jose Jorge Rios

Ramirez, Karthick Sekar, Onyekachi Nwakanma Michel, Ashok Adhikari, Ganesh Regmi, Drisya Damodaran, Christeena Theresa Thomas, Fernanda, Josue Ramirez, Alejandra Muniz, Hugo Cesar, Alan Moron, Dorian Valencia, and Francisco) for their care and support throughout the work. Special thanks to Srikanth Chakravarthy, Ravichandran Manisekaran, Karthick Sekar, Onyekachi Michael, Goban Kumar, Sandheep, Ivonne Lucia, Liliana Resendiz, Amron Amicrag, Ana Martinez, and Stefany Granados for their care, help, and support. A special thanks to Mrs. Malathi Velumani for her care, affection, and support. A special thanks to all my professors, especially to Dr. Sathyamoorthy, for motivating me always and to utilize this PhD opportunity.

Finally, I would like to thank my family, Father (Babudurai), Mother (Rebecca), Brother (Melchi Raja), Fiance (Ezekiel Paul), and his family for their unconditional love, encouragement, and support. With their love, support and prayers, I can go through all the difficulties anytime. I also like to thank my relatives, Indian and Mexican friends for their continuous love and support.

You all people made this journey successful; my heartfelt thanks to everyone!

"Difficulties in your life do not come to destroy you, but to help you realize your hidden potential and power, let difficulties know that you too are difficult."

"An arrow can only be shot by pulling it backward. When life is dragging you back with difficulties, it means it will launch you into something great. So focus, and keep aiming."

THANK YOU ALL!

With Regards,

MERCYRANI BABUDURAI.

TABLE OF CONTENTS

LIST OF FIGURES

LIST OF TABLES

LIST OF ABBREVIATIONS

NPs	Nanoparticles
IOs	Iron oxides
T	TiO_2
M	Magnetite, Maghemite
NCs	Nanocomposites
As	Arsenic
PC	Photocatalysis
VB	Valence Band
CB	Conduction Band
AOPs	Advanced Oxidation Process
BPR	Ball to Powder Ratio
RPM	Rotation Per Minute
MCL	Maximum Contamination Limit
WHO	World Health Organization
NaOH	Sodium hydroxide
HCl	Hydrochloric acid
H_2SO_4	Sulphuric acid
H_2O	Water
$KMnO_4$	Potassium permanganate
$TiCl_4$	Titanium chloride

C_2H_5OH	Reagent alcohol
ICDD	International Center for Diffraction Data
SAED	Selected Area Electron Diffraction
FFT	Fast Fourier Transform
XRD	X-Ray Diffraction
UV-Vis	Ultraviolet Visible
DRS	Diffuse Reflectance Spectra
SEM	Scanning Electron Microscope
STEM	Scanning Transmission Electron Microscope
EDAX	Energy Dispersive Analysis of X-rays
HRTEM	High Resolution Transmission Electron Microscope
XPS	X-ray Photoelectron Spectroscopy

1. CHAPTER 1 - INTRODUCTION

1.1 Safe drinking water: A global problem

Water is regarded as one of humankind's essential needs. It is an abundant resource on mother earth. Humans can live without food, but without water, life is impossible. To sustain a healthy life, clean and pure drinking water is mandatory [1]. Water comprises 70% of the earth's surface, in that less than 1% of the world's water is available to us [2]. All over the world, 2 billion people do not have access to safe and clean drinking water [3]. As per various organizations like the WHO, the water shortage may affect people up to 4 billion by 2050 [4]. The water pollution sources are dyes, heavy metals, pathogens, pesticides, fluorides, and pharmaceuticals shown in figure 1.1 [5].

Figure 1.1Main sources of water pollution

(Reproduced with permission from ref. 5)

It will cause water-borne diseases, including typhoid, cholera, hepatitis, skin infection, gastrointestinal problems, etc. [6]. According to WHO, 80% of human diseases are waterborne, and it has provided drinking water guidelines that may compromise drinking water safety [7]. Increasing the population increases the demand for good quality water. One of the most significant challenges of this century is providing safe drinking water [8].

1.2 Nanotechnology for water treatment

Nanotechnology is one of the most explored technologies of the 21st century [9]. For drinking water treatment, it has gained the potential to resolve the current water crisis. It offers an effective way to remove the toxic contaminants within an affordable cost-framework [10]. It promises to ensure viable availability of clean drinking water and conservation of water resources by applying advanced materials and techniques for water purification, conservation, and reuse. It is used in critical areas such as bioremediation and water disinfection [11]. It also creates new economic opportunities for developed, underdeveloped, and developing countries [12].

Based on structural components, the nanomaterials are sized between 1 and 100 nm. Their size provides them with properties, such as mechanical, electrical, optical, and magnetic, which are significantly different from bulk materials [10]. Nanomaterials have been widely useful in many fields, such as adsorption [13], photocatalysis [14], medicine [10], and sensing [15]. The nanomaterials typically possess a high specific surface area, small size, highly organized structure, strong adsorption capacities, and outstanding reactivity [16]. Hence it is widely used to degrade organic pollutants [17], transform inorganic pollutants into innocuous substances [18], and inactivate microorganisms [19].

Nanomaterials can be used as adsorbents, catalysts, and membranes [10]. The nanocatalyst for water treatment involves photocatalytic activities that include light energy interaction with metallic nanoparticles (NPs), which can destroy the organic substances via the reaction with hydroxyl radicals [20]. The metal oxide semiconductors are widely used as nano-catalysts, while the nano adsorbents for water treatment utilize organic or inorganic nanomaterials. Nano-adsorbents are classified into metallic NPs, magnetic NPs, nanostructured mixed oxides, and metallic oxide NPs [21] [22]. These adsorbents are highly capable of removing contaminants even at trace levels [23]. NPs provide high surface area, but their agglomeration may limit their use. This limitation can be minimized by the conversion of nanoparticles into nanocomposites [24] [25].

1.3 Water pollution due to dyes and heavy metals

The presence of non-biodegradable effluents such as heavy metal and metalloid ions (arsenic, zinc, copper, nickel, mercury, cadmium, lead, and chromium) are not only classified as carcinogens but are also harmful to the environment [26] [5] [27] [28]. Also, various industrial pollutants (e.g., organic dyes) such as methylene blue (MB), rhodamine B (RhB), rhodamine 6G (Rh6G), methyl orange (MO), and organic chemicals like phenols pose a severe threat to the global ecosystem that needs to be addressed [29] [30] [31].

1.3.1 Azo Dyes

Dyes are of significant concern to environmental health. These contaminants are found in the water resources from various industries like paper, leather, plastics, and textiles [32]. The textile industry is spread globally, especially the global apparel market generating around 1.5 trillion dollars in 2020. It will be around 2.25 trillion by 2025 [33]. It contributes 7% of the total world exportations employs around 35 million workers [34]. However, it is one of the biggest global

polluters through washing, bleaching, and dyeing. More than 3,000 different types of dyes are available in the market; half of them belong to the azo dyes compounds [29] [30].

Azo dyes are organic compounds characterized by one or more azo groups (-N=N-) [35]. It forms a bridge between organic residues in that one is generally an aromatic nucleus. It is linked to phenyl and naphthyl radicals, which are replaced with some functional groups including amino ($-NH_2$), chlorine (-Cl), hydroxyl (-OH), methyl ($-CH_3$), nitro ($-NO_2$), sulphonic acid, and sodium salts ($-SO_3Na$) [36]. Several countries, such as German, Sweden, France, and Denmark, have formulated their environmental legislation to restrict hazardous dyes in textiles and clothing production. According to the legislation, the allergenic azo dyes are (Disperse Yellow 1/3; Disperse Orange 3/37/76; Disperse Red 1; Disperse Blue 1/35/106/124), and some are carcinogenic (Acid Red 26, Basic Red 9, Basic Violet 14, Direct Black 38, Direct Red 28, Direct Blue 6, Disperse Yellow 3, Disperse Orange 11, Disperse Blue 1) [37].

Exposure to these dyes has been related to the development of bladder cancer, splenic sarcomas, hepatocellular carcinomas, cell anomalies, and chromosome aberrations; they also represent an aesthetic problem in the aquatic bodies [38]. These dyes are toxic or carcinogenic, which causes skin allergy, nausea, skin irritation, and breathing difficulties [39]. These dyes are considered persistent in water due to their bright color, acidic nature, and water-soluble reactive characteristics [40]. The minor quantities of dyes change massive water bodies' color and decrease light penetration needed for photosynthesis [41]. Due to the complex aromatic molecular structures, these dyes are more stable and difficult to biodegrade [31]. These dyes are stable in air and under light; hence they did not respond to ordinary biological or chemical degradation [42]. Hence, the removal of dyes from water resources has gained environmental importance.

1.3.2 Heavy metals

Heavy metals include metals and metalloids with relatively high density (4×10^6 mg/L) and are very poisonous, even in very low concentrations [43]. Natural and anthropogenic are the two primary sources of heavy metals in drinking water. Natural sources include soil erosion, volcanic activities, weathering of rocks and minerals, whereas anthropogenic sources include mining, industrial and agricultural activities [26] [44]. These heavy metals cause serious health effects to human beings. Hence, WHO has provided guidelines to define safe drinking water and the permissible limit of heavy metals in drinking water shown in table 1.1 [45].

Table 1.1 WHOs heavy metals maximum permissible limit in drinking water

Heavy metals	WHOs permissible limit (mg/L)
Arsenic (As)	0.01
Cadmium (Cd)	0.003
Chromium (Cr)	0.05
Lead (Pb)	0.05
Manganese (Mn)	0.5
Zinc (Zn)	5.0
Copper (Cu)	0.1
Mercury (Hg)	0.001
Nickel (Ni)	0.1

Arsenic is a crystalline "metalloid," a natural element that ranks the 20th most occurring element in the Earth's crust. Arsenic (As) exists in various oxidation states (-III, 0, +III, +V), but Arsenite (III) and Arsenate (V) are mostly present in the aqueous media [46] [47]. These can be leached from industrial wastes, biological activity, soils, mining activities, and fertilizers,

containing minerals and occurring naturally [48] [47]. Inorganic contaminants, especially in metallic forms, are carcinogenic, with heavy metals like arsenic (As) being top on the list [43]. Several studies disclose that millions of people worldwide get exposed to heavy metals through contaminated drinking water and groundwater used for domestic purposes [23] [49]. Recent studies disclose that over 200 million people worldwide are affected by arsenic-contaminated drinking water and groundwater, which has been reported in the USA, China, Chile, Bangladesh, Nepal, Vietnam, Taiwan, Mexico, Argentina, Poland, Italy, Finland, Spain, Canada, Hungary, New Zealand, Japan, and India [23][49]. The varying degrees of pollution severity on different parts of the globe show that arsenic ranks tops, justifying the numerous attempts to develop methods, such as ion exchange, oxidation, adsorption, precipitation, etc. for removing it from potable water sources [50] [51] [52] [53] [54].

As (III) is a hard acid and forms complexes with oxygen and nitrogen. On the contrary, As (V) behaves like a soft acid, forming complexes with sulfides [55]. As (III) is present in the form of uncharged arsenous acid H_3AsO_3, under reducing conditions at pH 6.5 - 8.5, and neutral in most of the other pH ranges [56] [57]. The As (V) is present in the form of $H_2AsO_4^-$ and $HAsO_4^{2-}$ anions in oxidizing waters, as shown in figure 1.2 [58]. The arsenic atoms may combine with a complex carbon atom framework to form harmless organic structures or exist as highly toxic inorganic arsenic compounds that do not contain carbon [59]. The presence of arsenic in the environment, especially in water bodies, comes from arsenic-bearing minerals and the reductive dissolution of As (V) to the much more soluble As (III). Both As (III) and As (V) anions are toxic, with the As (III) being more toxic, very water-soluble, and thus mobile in water environments. As (V) occurs in more stable aerobic or oxidizing conditions, such as surface waters, while As (III) compounds are stable under anaerobic or mild-reduced conditions, like subsurface waters [60] [61]. A primary

method used to remove As from water is surface complexation of As (III) and As (V) with solid sorbents, e.g., materials containing titanium and iron. For instance, Fe reacts with As anions and form insoluble and eventually very stable Fe-As complexes that remove As from water [62] [63].

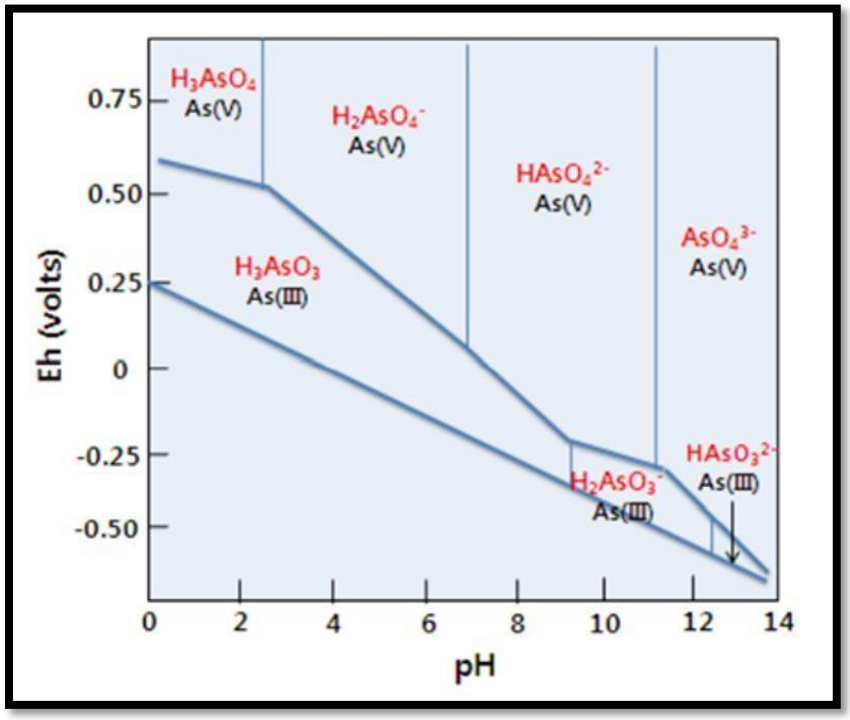

Figure 1.2 Speciation of Arsenic in water depending on pH

(Reproduced with permission from ref. 58)

Owing to their prevalence in the environment, the European Union (EU), the United States (US), and the World Health Organization (WHO) established a maximum threshold for this contaminant at 10 μg/L in drinking water. Other countries retained the WHO guideline's earlier limit at 50 μg/L, as their interim target [55]. The long-term exposure or intake of As-contaminated food or water will lead to many serious diseases. Acute and chronic poisoning involves respiratory, gastro-intestinal, conjunctivitis, hyperkeratosis, hyperpigmentation, cardiovascular diseases,

disturbance in the peripheral vascular and nervous systems. Arsenic is highly carcinogenic, leading to cancer in the lungs, bladder, liver, kidneys, and skin [64] [27] [64]. The effects of As on human health are shown in figure 1.3 [65]. Hence there is a significant need to remove these contaminants from drinking water.

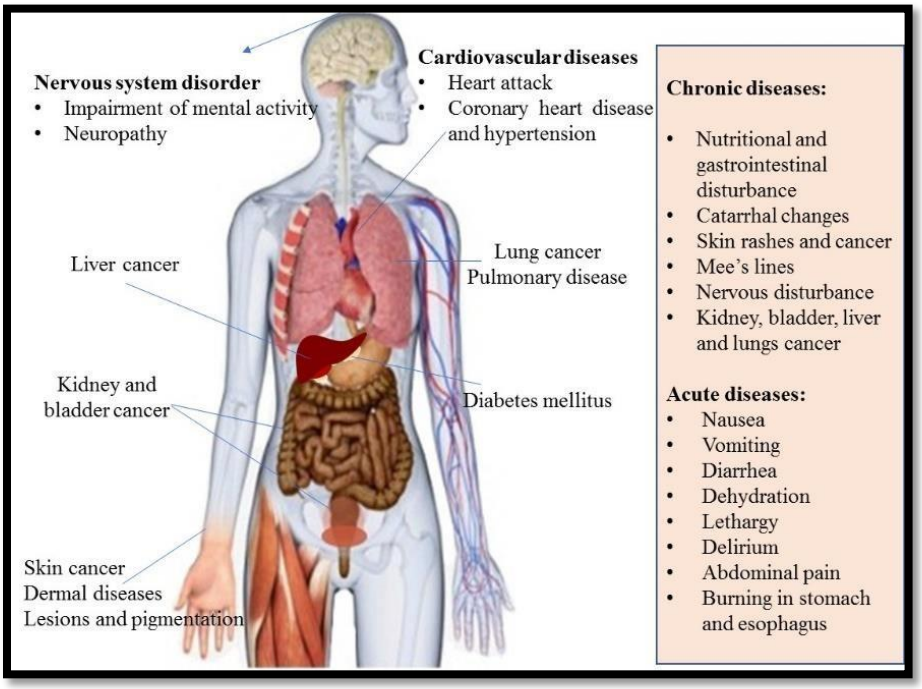

Figure 1.3 Arsenic health effects on humans

(Reproduced with permission from ref. 65)

1.4 Water treatment removal methods for Arsenic

Various water treatment methods have been developed and categorized based on physical, chemical, thermal, electrical, and biological principles [66] [67] [68] [69] [70]. The broadly used water treatment methods, their advantages, and disadvantages are presented in table 1.2.

Table 1.2 Advantages and disadvantages of water treatment methods

Water treatment methods	Advantages	Disadvantages	Ref.
Chemical precipitation	• It is widely used to remove soluble contaminants.	• It requires a large number of chemicals. Hence the cost of precipitation becomes high. • It is not a convenient method for domestic purposes because it contains a low metal concentration	[71]
Ion exchange	• An effective and efficient technique used in water treatment	• It increases the acidity of water, which makes water unsafe for drinking. • Ion exchange resins are costly than adsorbents.	[72]
Membrane filtration	• It is widely employed in the industries. • It works effectively at low temperatures.	• It is costly • When the concentration of metal increases, the elimination of the membrane is decreased.	[1]
Electro - coagulation	• It removes soluble and insoluble dyes and ions from water. • It breaks down all the toxic compounds in the electrolytic cell.	• It produces a large amount of sludge, which will cause secondary pollution. • It needs a large amount of electricity.	[73]
Photo - catalysis	• Widely used in water treatment • It treats nearly all organic materials and some heavy metals	• It is inefficient to oxidize some contaminants • Induction of light may produce harmful by-products	[74]

		• It needs additional steps to recover the catalyst like adsorption, filtration, etc.	
Adsorption	• Low-cost and provides high efficiency • Easy operating conditions within a wide pH range • High metal-binding capacities when adsorbents own high surface area • Removes both inorganic and organic pollutants.	• Generation of hazardous wastes	[75]

Most of the technologies are expensive and produce toxic by-products. Nevertheless, they are not efficient enough to remove the contaminants to meet the WHO's water quality standards [76]. Therefore, a growing need to establish a well-defined technology to cope with the local and regional scarcity of safe potable water. This work focuses on photocatalysis and adsorption techniques to remove dyes and heavy metals from water for human consumption.

1.5 Photocatalysis

Among Advanced Oxidation Processes (AOPs), heterogeneous photocatalysis is an efficient tool for degrading organic and inorganic contaminants. It involves the acceleration of a photo-reaction in the presence of a semiconductor photocatalyst [77]. It includes various reactions such as organic synthesis, water splitting, photo-reduction, hydrogen transfer, disinfection, metal deposition, anti-cancer therapy, water detoxification, gaseous pollutant removal, etc. [78] [79] [80] [81]. It employs a semiconductor material, like ZnS, ZnO, Fe_3O_4, CdS, GaP, TiO_2, and $BiVO_4$, as

a catalyst [82] [83] [84]. These semiconductor catalysts present different efficiencies for degrading a wide range of hazardous refractory organics into non-toxic, biodegradable compounds. Finally, they can mineralize them by converting them into carbon dioxide, other mineral components, and water [85]. Titania-based photocatalytic materials have received more attention in water treatment [86] [87].

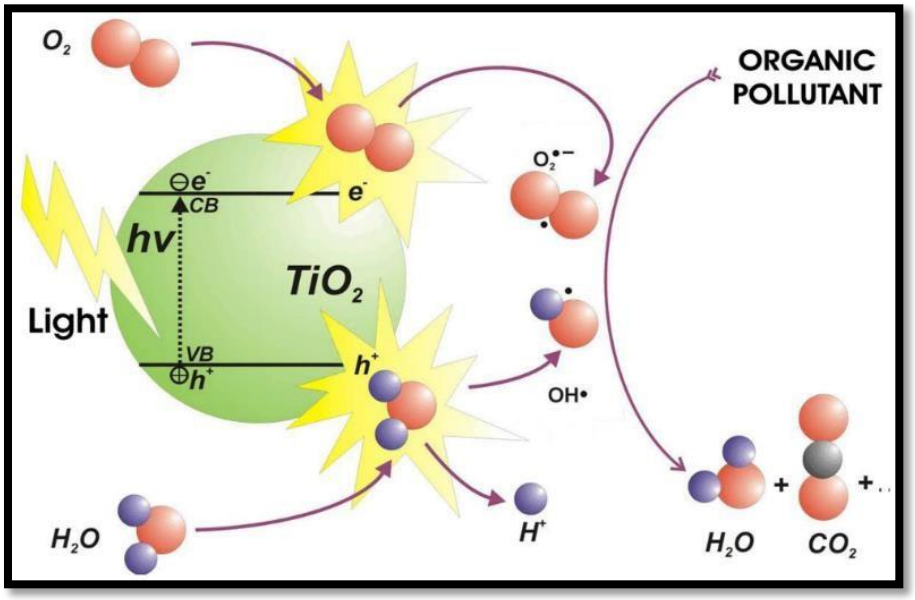

Figure 1.4 Mechanism of Photocatalysis

(Reproduced with permission from ref. 77)

The photocatalytic reaction is originated when the photons fall on the surface of a semiconductor; if the incident light energy is equal to or more than the bandgap energy of the semiconductor, the electrons in the valence band are agitated and move to the conduction band, and the holes will be left in the valence band. These holes in the valence band can oxidize donor molecules and react with water molecules to generate hydroxyl radicals (•OH). The conduction band's photo-electrons react with dissolved oxygen species to form superoxide ions ($•O_2^-$). These excited electrons induce redox reactions. Photo-generated holes and electrons can undergo

consecutive oxidation and reduction reactions with any species adsorbed onto the photocatalyst's surface, producing reaction intermediaries [84] [88]. The mechanism of photocatalysis is shown in figure 1.4 [77].

1.5.1 TiO_2 as photocatalyst

Among various semiconductors, Titania (TiO_2) has gained much attention in photocatalysis processes. It is the most active photocatalysts, with bandgap energy between 300 and 390 nm, remaining stable even after the repeated catalytic cycles [89]. TiO_2 owns chemical and thermal stability that is crucial for the photocatalytic treatment. In nature, TiO_2 exists in three polymorphs, namely, anatase, rutile, and brookite, shown in figure 1.5 [90]. The cell volume of anatase is smaller than that of rutile and brookite. The structure of TiO_2 is formed by each Ti atom surrounded by six oxygen atoms. The unit cell of tetragonal anatase contains four TiO_2 units, i.e., 12 atoms, while the unit cell of tetragonal rutile contains two TiO_2 units, i.e., 6 atoms, and the unit cell of orthorhombic brookite contains eight TiO_2 units, i.e., 24 atoms [91] [92] [93].

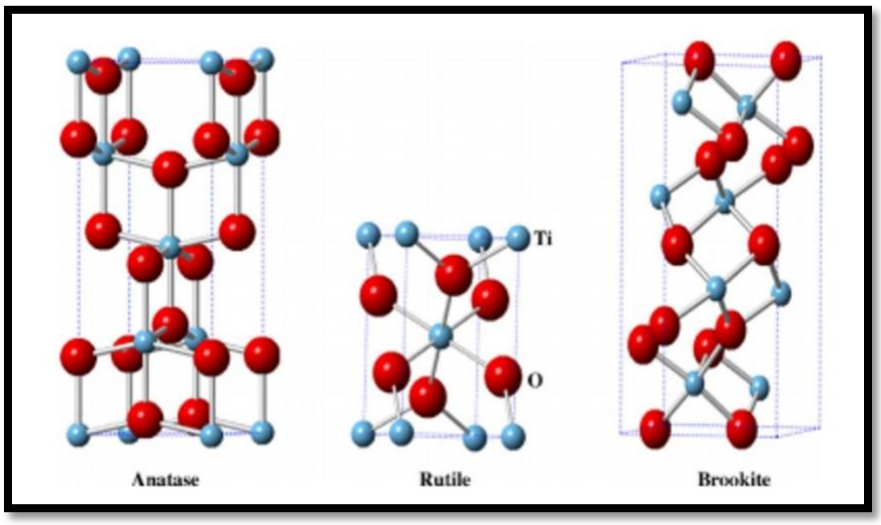

Figure 1.5 TiO_2 polymorphs anatase, rutile, and brookite

(Reproduced with permission from ref. 90)

Among these polymorphs, the anatase displays much higher photocatalytic activity; it is because of the phase structure, crystallite size, specific surface area, pore structure, small grain size, high surface area, adsorption capacity towards hydroxyl groups, and lower charge carrier recombination [94] [95] [96]. The TiO_2 anatase (E_g = 3.2 eV) is an indirect bandgap semiconductor, while rutile (E_g = 3 eV) and brookite (E_g = 3.3 eV) are direct bandgap semiconductors. The anatase (101) surface has comparable OH• radical generation activity to that on the rutile (001) surface [97] [86]. Semiconductors with indirect bandgap generally exhibit longer charge carrier lifetimes compared to direct bandgap materials. The lifetime of photo-generated electrons and holes in anatase is about an order of magnitude larger than that of the photo-generated electrons and holes in rutile, thus significantly enhancing the chance of photo-excited electrons and holes in anatase to reach the crystal surface to perform chemical reactions [98].

The transfer rate of photogenerated electrons and holes is inversely proportional to their effective masses; when the effective mass of photogenerated carriers is large, carriers' transfer rate will be slow. Thus, the small effective mass can promote the migration of charge carriers and inhibit charge carriers' recombination. According to the literature, the average effective mass of photogenerated electrons and holes in anatase is smaller than that of rutile and brookite; thus, the holes and electrons' transfer rate is the fastest among the three materials. It indicates that the photo-excited charge carriers of anatase more easily migrate and transfer to the bulk's surface to participate in photocatalytic reactions [91]. Although TiO_2 itself is the best photocatalyst, its large bandgap energy (E_g ~3.23 eV) severely limits its photocatalytic application under sunlight-driven conditions [99] [83] [100] [101]. The photocatalytic activity is reduced by recombination of photo-generated electron-hole pairs [102]. Once the TiO_2 nanoparticles are suspended in water, it is

difficult to recollect the dispersed TiO_2 nanoparticles. Therefore, a better approach is adopted to resolve this critical issue without compromising the photocatalytic activity. In recent days, the iron oxide-based photocatalyst is trending because it enhances PC activity by reducing the wide bandgap of TiO_2. After the PC process, the suspended nanomaterials can be recollected by a strong external magnetic field in the suspension system [102] [41] [24].

1.5.2 Iron oxide as photocatalyst

Magnetic nanomaterials that are also photocatalysts come in handy when necessary to enhance the photocatalytic activity and retrieve the photocatalysts [103]. Compared to other semiconductor materials, magnetic iron oxide NPs have better optical, chemical, magnetic, electrical, and thermal properties that enabled them to be used in numerous applications such as in consumer electronics, catalysis, ferrofluids, data storage, and biomedical and pigments [104] [105].

Among 16 different types of iron oxide polymorphs, Fe_3O_4 and Fe_2O_3 are highly explored. Magnetite (Fe_3O_4) is the most naturally occurring mineral on earth. It possesses a cubic inverse spinel structure, belonging to the space group Fd3m. It gained much attention among the various iron oxide phases because of its high saturation magnetization at room temperature (84 emu g^{-1}) [106]. In Fe_2O_3 polymorph, γ-Fe_2O_3 (maghemite) and α-Fe_2O_3 (hematite) phases are widely studied [107]. γ-Fe_2O_3 exhibits the cubic spinel structure. It is a ferrimagnetic material at room temperature with a Curie temperature of 928 K [108] [109]. The α-Fe_2O_3 (hematite) is thermodynamically the most stable phase of Fe_2O_3. It is weakly ferromagnetic at room temperature and is antiferromagnetic below 263 K [110] [111]. At an elevated temperature of > 950 K, i.e., Curie temperature, it will show paramagnetic behavior [112]. Magnetite (Fe_3O_4) containing iron in both divalent Fe (II) and trivalent Fe (III) in its structure. However, it may oxidize by air even at room temperatures. Hence it is not considered a stable phase. Maghemite is an oxidized form of

magnetite, and it contains iron in the trivalent state Fe (III). Hematite is another stable iron oxide, but it contains only Fe (II) state [107] [113]. These properties are responsible for the change in iron oxide behaviors.

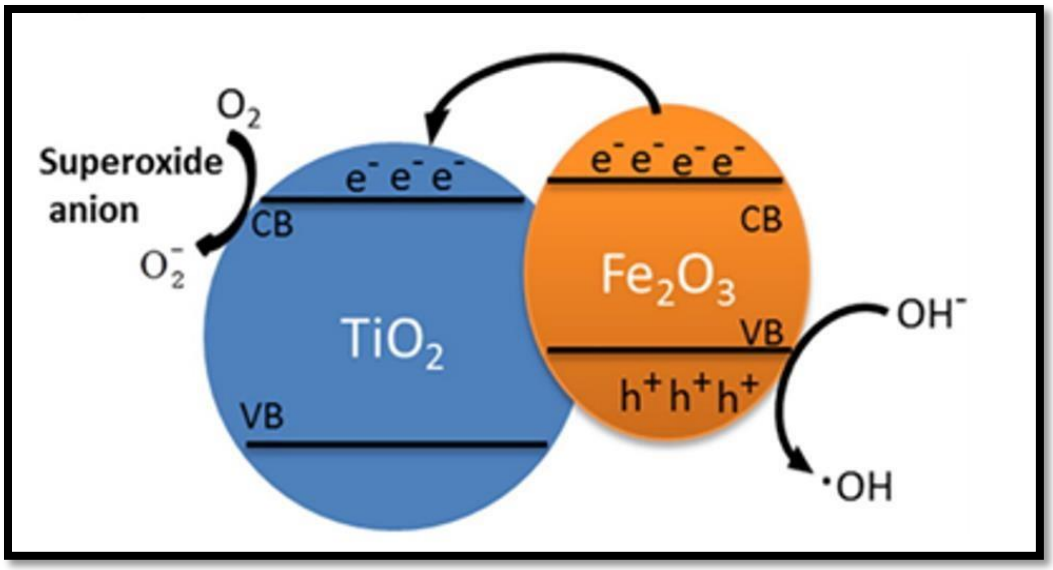

Figure 1.6 Charge transfer between TiO_2 and Fe_2O_3 during the photocatalytic process under visible light irradiation

(Reproduced with permission from ref. 117)

However, the large surface-to-volume ratio of iron oxide NPs results in high surface energies and aggregation. Iron oxide NPs are readily oxidized in the air due to their high reactivity, decreasing their dispensability and magnetic behavior [114]. Therefore, it is essential to maintain the iron oxide stability through the passivation of the NPs with organic ligands, polymers, and monomers [115]. Aggregation of Fe_3O_4 NPs results in the reduction of surface-active regions that are required for an improved light scattering. Therefore, the pristine magnetite NPs have to be modified with TiO_2 to achieve the highest photocatalytic activity. A high surface area can result in more affinity to hydroxyl groups (OH^-) and produce hydroxyl radicals (•OH). The produced

hydroxyl radicals are the essential oxidants needed for degrading organic compounds, like various dyes [116]. When iron oxide modifies TiO_2 NPs, it will give rise to small particle size and low bandgap nanocomposites, as shown in figure 1.6 [117]. The addition of iron-oxide to titania promotes the interband transition of electrons from the valence band to the conduction band resulting in the decrease of the bandgap of TiO_2 [118]. The presence of titania coating over magnetic NPs acts as a charge scavenger that reduces the recombination rate and increases the photocatalytic activity [119].

1.6 Adsorption

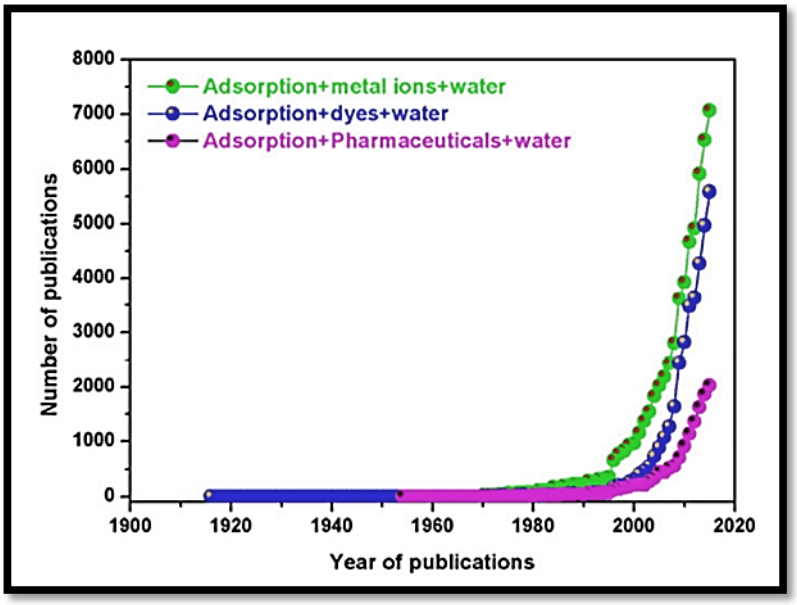

Figure 1.7 Number of publications on adsorption in recent years

(Reproduced with permission from ref. 75)

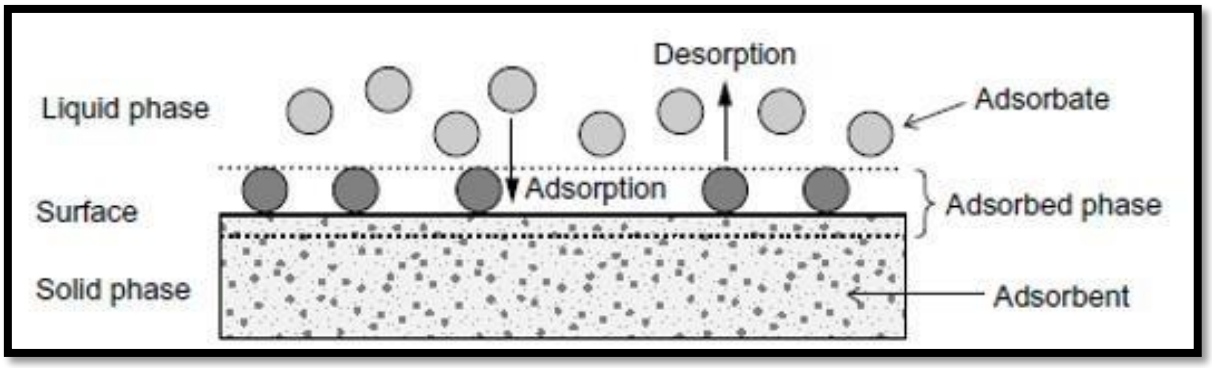

Figure 1.8 Basic terms of adsorption

(Reproduced with permission from ref. 123)

Among various techniques, adsorption is considered a universal water treatment and reclamation technique. It removes the organic, inorganic, and biological pollutants, which are soluble and insoluble in water. Recently, the tremendous interest in adsorption led to numerous publications, shown in figure 1.7 [75]. Adsorption has been successfully applied to remove aqueous phase heavy metals and dyes [120] [121]. As compared with other conventional methods, the adsorption process offers numerous advantages of stability, durability, wide pH range, high surface, easy operation, cost-effective, and selective approach for water treatment and analysis [60] [122]. Adsorption is the deposition of molecular species onto the surface of solid adsorbent material. The molecular species that get adsorbed on the surface are known as adsorbate, and the surface on which adsorption occurs is known as adsorbent. It is a surface phenomenon, which is shown in figure 1.8 [123]. The removal of the adsorbate from the surface of the adsorbent is known as desorption [13]. Adsorption can be either chemical or physical. In chemical adsorption, the adsorbate and adsorbent forces are of a chemical bond owing to electron transfer, and the bond may be considered ionic, metallic, or covalent. In physical adsorption, pollutants get accumulated on the adsorbent surface by physical forces, such as Van der Waals forces, hydrogen bonds,

electrostatic interactions, and dipole-dipole ∏–∏ interaction [13]. An adsorption isotherm is defined as the amount of material adsorbed on a substrate (solid, liquid, or gas) as a function of the equilibrium concentration remaining after adsorption at a constant temperature [124]. The well-known models used to explain adsorption studies' results are Langmuir, Freundlich, Elovich, intraparticle diffusion, and Lagergren [125] [126]. The kinetic study is carried out by scheming enthalpy, free energy, entropy, and activation energy [125] [127]. The adsorption technique is developed by the batch process, followed by the column studies. It is applied first at the pilot and later on industrial scales [56] [128].

1.6.1 Adsorbents

The nano adsorbent with smaller particle size, higher surface area, a large number of active sites, porous, and amorphous nature, can significantly adsorb the contaminants in water. Activated carbon (AC), a highly porous and amorphous solid, is the most commonly used adsorbent, but it is costly and limits its application. Metal oxides and iron hydroxides, aluminum, and manganese exist abundantly in the natural aquatic environment; these oxides are environment friendly and widely used as an adsorbent for removing various water contaminants. The use of some metals and metal oxides, for example, Fe_2O_3, TiO_2, CeO_2, CuO, and ZrO_2, have been extensively employed considering the low-cost, high adsorption capacity and affinity towards arsenic [129][130][131]. Other studies employ the combination of two or more metal oxides to enhance the adsorption behavior, and that has attracted considerable interest from researchers recently [132][133][134]. The use of metals and metallic oxides for the adsorption of arsenic oxyanions depends strongly on the properties of the active sites of d-block elements (i.e., Fe, Cu, Mn, Zn, Ni, and Ti) [135].

1.6.1.1 TiO_2 as adsorbent

TiO_2 anatase phase has been widely investigated in adsorption due to its low toxicity, physicochemical stability, facile preparation, low-cost, and eco-friendly [136] [137]. Still, it has certain limitations; the surface area decreases due to agglomeration; fortunately, this drawback can be overcome by forming nanocomposites or coating with other metals or metal oxides [138]. The proposed reaction mechanism of Pb (II), Cu (II), and As (III) on the anatase nano-adsorbent surface is shown in figure 1.9 [120]. It indicates that As (III) is not oxidized to As (V) during the adsorption process. Only the metal oxide and hydroxyl groups on the anatase nano-adsorbent are responsible for the heavy metal adsorption. The nano adsorbents surface groups can react with heavy metals and directly form a stable inner-sphere and outer-sphere complex through electrostatic binding. It forms superficial monodentate and bidentate complexes [120].

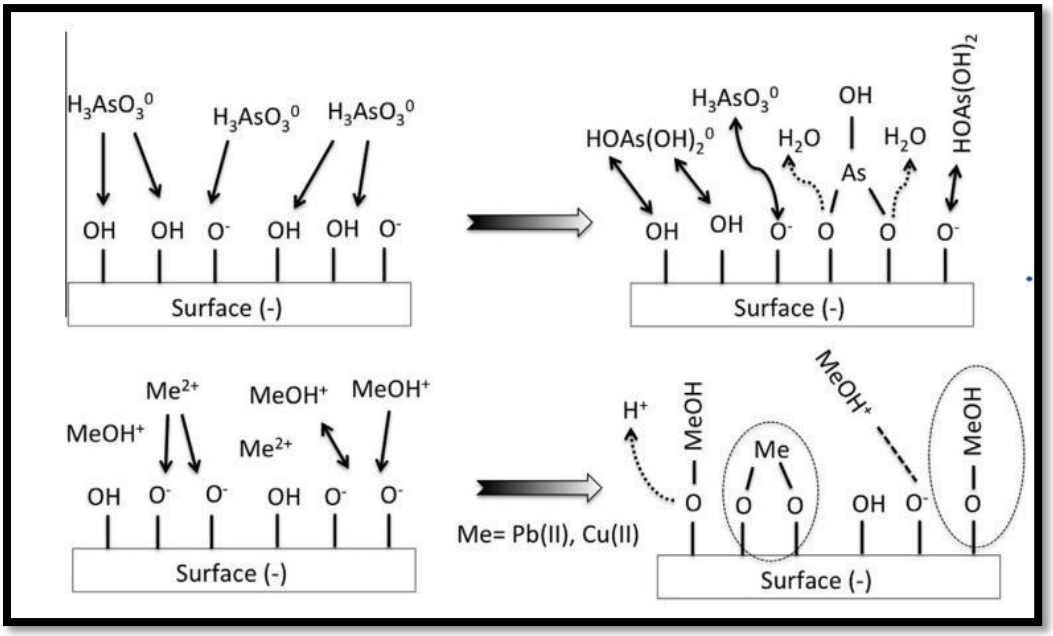

Figure 1.9 The reaction mechanism of Pb (II), Cu (II), and As (III) on the anatase nano adsorbent

(Reproduced with permission from ref. 120)

1.6.1.2 Iron oxide as an adsorbent

Among iron oxide nanomaterials, Fe_3O_4 (Magnetite), α - Fe_2O_3 (Hematite), and γ – Fe_2O_3 (Maghemite) are the most common, highly explored, and widely used adsorbents in water treatment applications [139]. The crystal structure and crystallographic data of hematite, magnetite, and maghemite are shown in figure 1.10 [140]. Fe_3O_4 is a face-centered cubic (FCC) spinel structure based on 32 O_2^- ions and close-packed along the direction. It contains both divalent and trivalent iron. The Fe^{2+} ions occupy half of the octal, Fe^{3+} is split evenly across the remaining octahedral sites and the tetrahedral sites. In comparison, the ferric ions are distributed over tetrahedral sites (eight Fe ions per unit cell) and octahedral sites (the remaining Fe ions and vacancies).

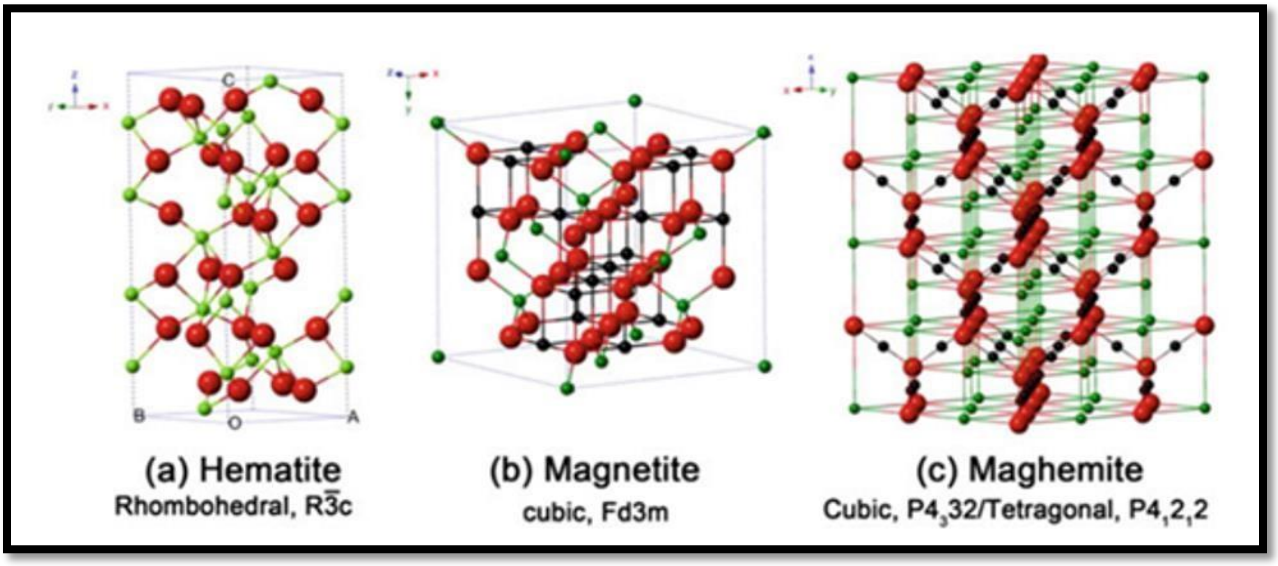

Figure 1.10 Crystal structure and crystallographic data's of hematite, magnetite, and maghemite

(Reproduced with permission from ref. 140)

Among that, γ – Fe_2O_3 is the most stable polymorph of iron oxide. Maghemite exhibits a cubic crystal structure with each cell containing 32 O^{2-} ions, $21^{(1/3)}$ Fe^{III} ions, and $2^{(1/3)}$ positive vacancies. The cationic vacancies are located in the octahedral sites, which provide stability and homogeneous ion distribution in γ – Fe_2O_3 and significantly increases the adsorption efficiency compared to other phases that contain only singly coordinated reactive hydroxyl moieties [141]. Predominantly, iron oxides provide excellent adsorption properties, with high surface-area-to-volume ratio and modifiable surfaces, better biocompatibility, excellent magnetic properties, reusability, ease of separation using an external magnetic field, and comparatively low cost [142] [143]. The adsorption mechanism of iron oxide-based nano-adsorbents depends on heavy metals' migration, deprotonation, and surface complexation. The mechanisms mainly occur through ligand exchange, i.e., hydroxyl (OH^-) or hydroxide (OH_2) groups in the coordination sphere of surface structural Fe atoms, and explained through zero-point charge [144]. In the ion exchange process, specific adsorption to OH^- groups and recoverability due to their magnetic properties positioned the iron-based adsorbents significantly for the adsorption process [145]. They can coordinate easily with other elements due to variable oxidation states.

1.6.1.3 TiO_2/Fe_2O_3 nanocomposite as adsorbent

To enhance the adsorption behavior, composites comprised of two or more metal oxides combined have attracted considerable attention from researchers recently [132] [133] [134]. As mentioned before, the anatase TiO_2 phase is widely employed to remove contaminants through adsorption due to its low toxicity, physicochemical stability, facile preparation, low-cost, and being eco-friendly [136]. However, it has certain limitations, posing a significant drawback, such as the surface area, which decreases due to agglomeration, removed by forming nanocomposites or coating with other metals or metal oxides [138]. Also, the separation of the adsorbed materials

needs additional steps, such as filtration, precipitation, membrane separation, etc. Combining the TiO_2 nanomaterials with other nanomaterials, e.g., iron-based adsorbents eliminates these common challenges. The iron-based adsorbents play a significant role in adsorption due to their ion-exchange and specific adsorption to hydroxyl groups. They can also help recover and recycle the NPs because of their magnetic property after arsenic adsorption [145] [146]. Hence, one of the most suitable iron-oxide adsorbents is the maghemite (γ-Fe_2O_3), which is more stable than magnetite (Fe_3O_4) combined with TiO_2 anatase, to overcome the limitation of TiO_2 and also to increase the efficiency of heavy metal adsorption.

1.6.2 Overview of factors affecting adsorption

Adsorption is determined by various parameters, such as pH, initial concentration of adsorbate, time, and dosage of the adsorbent. The systematic study of these conditions provides an understanding of the better-operating conditions. Furthermore, efficient applications can allow for better utilization and reusability of the adsorbent materials. The brief overview presented in this subsection elucidates these factors and their influence on arsenic adsorption.

1.6.2.1 Effect of adsorbate concentration

The initial concentration of the adsorbate significantly influences the adsorption process. At low concentrations of the adsorbate, the surface area, adsorption sites of the adsorbents, and availability are relatively high; hence, allowing for readily adsorbing the contaminants [147]. However, higher concentrations can signify that all available adsorption sites are less, decreasing the adsorption. Consequently, the percentage removal of an adsorption process depends upon the ratio of the number of adsorbate moieties to the adsorbent's available active sites in a particular environment [148]. This ratio also relates to the adsorbent's surface coverage (number of active sites occupied/number of active sites available), increasing the number of adsorbate moieties per

volume unit at a fixed dose adsorbent. A lesser ratio depicts more sites' availability, which gradually increases with the decrease in adsorbate resulting from increased percentage removal.

1.6.2.2 Effect of adsorbent dosage

The dosage refers to the adsorbents' concentration used in the adsorption process, determining an adsorbent's capacity for an initial adsorbate concentration. The optimal dose is mainly related to the active site's availability and surface functional groups' occurrence. The solute's adsorption magnitude increases with increased adsorbent concentration due to increased active exchangeable adsorption sites [149]. The increased dosage for nanomaterials increases the adsorbent surface area, and, therefore, more adsorption sites are available.

The adsorption may decrease with excess in adsorbent concentration due to interference resulting from the interaction of active sites of the adsorbent [150] [151] [152] [153]. The decrease in adsorption with an increase in adsorbent dosage may also be due to adsorption sites remaining unsaturated during the adsorption process [154]. Therefore, there is a vital need to optimize the dose of an adsorbent for achieving effective removal.

1.6.2.3 Effect of pH

The media's pH remains a critical variable affecting the adsorption of contaminants, mainly due to the ionization of both the adsorbate and the adsorbent's surface. The pH modifies the adsorbent's surface and the present functional groups, e.g., a hydroxyl. This potential modification aids the adsorbent to be efficient enough to adsorb in a slightly acidic environment and causes electrostatic repulsion by changing the pH values [155]. Other studies also report adsorption of arsenic and other metals (e.g., La) at pH values preferentially below 9.0 [154], supporting the findings that acidic and not alkaline conditions were beneficial for heavy metals' removal. The

constraints posed by pH in the aqueous media significantly affect the degree of speciation of arsenic and the charge of the adsorbent surface. The interaction between the iron oxides' surface containing hydroxyl group becomes protonated as $FeOH^{2+}$, causing the surface to acquire a positive charge [156]. It creates an electrostatic attraction between negatively charged ions and the positively charged iron oxide surface.

The acidic pH (around 4.0) favors the adsorption of anions onto the iron oxide surface and reportedly favors maximum adsorption capacity for As (V) due to their anionic forms [157]. Possible combinations, e.g., Fe and Ti, provide other functional groups at the surface, causing them to acquire more positive charge at various pH. These materials have large efficiency for arsenic removal from polluted water at various pH values. Some literature reports include maximum adsorption capacity for As (III) and As (V) using a composite of Fe-Me (Me = Sn, Cr, Cu, Mn, Ti) binary oxides [158] [59] [159] [160] [161].

1.6.2.4 Effect of contact time

The contact time is an essential factor affecting the adsorption process. It can also influence the economic efficiency of the process and the adsorption kinetics [162]. Initial stages always produce high adsorption, mostly due to the presence of many available sites for adsorption. However, increasing the contact time causes the adsorbents' active sites to get saturated with more adsorbates, decreasing the percentage of adsorption and efficiency.

1.7 Objectives of the work

The above discussions tell us that there is a significant need for innovative environmental technologies and clean, cost-effective, and industrial ecological processes to meet global contending water pollution efforts.

The objectives of the work are,

- Combining TiO_2 anatase with iron oxide using the ultrasonication method and enhance its photocatalytic activity to the visible region spectrum by reducing the bandgap of TiO_2 and studying its degradation properties for orange G.
- Optimizing the ball milling parameters, the ball to powder ratio, and milling time for the TiO_2/iron oxide nanocomposite and study the modulated nanostructured materials' effect on the arsenic adsorption.
- Optimizing the different ratios of TiO_2/iron-oxide nanocomposite using optimized ball milling parameters and study the effect of the different ratios on arsenic adsorption.
- Study the factors that influence arsenic adsorption, such as pH, dosage, time, concentration, and optimization, to achieve the WHOs maximum contamination limit (0.01ppm) using a novel, magnetically separable, mechanically synthesized TiO_2 /Iron oxide nanocomposites to achieve an effective removal of arsenic species from water.

1.8 References

[1] A. Boretti and L. Rosa, "Reassessing the projections of the World Water Development Report," *npj Clean Water*, vol. 2, no. 1, p. 15, Dec. 2019, doi: 10.1038/s41545-019-0039-9.

[2] R. Saha, N. C. Dey, M. Rahman, P. Bhattacharya, and G. H. Rabbani, "Geogenic Arsenic and Microbial Contamination in Drinking Water Sources: Exposure Risks to the Coastal Population in Bangladesh," *Front. Environ. Sci.*, vol. 7, no. May, p. 57, May 2019, doi: 10.3389/fenvs.2019.00057.

[3] R. Bain, R. Johnston, and T. Slaymaker, "Drinking water quality and the SDGs," *npj Clean*

Water, vol. 3, no. 1, p. 37, Dec. 2020, doi: 10.1038/s41545-020-00085-z.

[4] A. Boretti and L. Rosa, "Reassessing the projections of the World Water Development Report," *npj Clean Water*, vol. 2, no. 1, p. 15, Dec. 2019, doi: 10.1038/s41545-019-0039-9.

[5] R. Abdeldayem, "A preliminary study of heavy metals pollution risk in water," *Appl. Water Sci.*, vol. 10, no. 1, p. 1, Jan. 2020, doi: 10.1007/s13201-019-1058-x.

[6] T. Fever, H. E. Virus, D. Water, F. Poisoning, J. K. Griffiths, and J. K. Griffiths, "Waterborne Diseases Waterborne Diseases Clinical Syndromes and Cardinal Fea- tures of Infectious Diseases : Approach to Diagnosis and Initial Management," 2008.

[7] E. Funari, T. Kistemann, S. Herbst, and a Rechenburg, "Technical guidance on water-related disease surveillance," *World Heal. Organ. Eur.*, pp. 1–139, 2011.

[8] R. Jain, "Providing safe drinking water: a challenge for humanity," *Clean Technol. Environ. Policy*, vol. 14, no. 1, pp. 1–4, Feb. 2012, doi: 10.1007/s10098-011-0446-1.

[9] G. Tegart, "Nanotechnology : The Technology for the 21 st Century," *Second Int. Conf. Technol. foresight.*, pp. 1–12, 2003.

[10] R. G. Suthar and B. Gao, "Nanotechnology for drinking water purification," in *Water Purification*, Elsevier, 2017, pp. 75–118.

[11] S. Baruah, M. Najam Khan, and J. Dutta, "Perspectives and applications of nanotechnology in water treatment," *Environ. Chem. Lett.*, vol. 14, no. 1, pp. 1–14, Mar. 2016, doi: 10.1007/s10311-015-0542-2.

[12] V. A. Basiuk and E. V. Basiuk, *Green Processes for Nanotechnology*, no. January. Cham:

Springer International Publishing, 2015.

[13] E. Worch, *Adsorption Technology in Water Treatment*. Berlin, Boston: DE GRUYTER, 2012.

[14] E. RA, "Advances in Photo-catalytic Materials for Environmental Applications," *Res. Rev. J. Mater. Sci.*, vol. 04, no. 02, 2016, doi: 10.4172/2321-6212.1000145.

[15] W. Zeng, H. Wang, and Z. Li, "Nanomaterials for Sensing Applications," *J. Nanotechnol.*, vol. 2016, pp. 1–2, 2016, doi: 10.1155/2016/2083948.

[16] "(7) (PDF) A Review of Removal of Pollutants from Water/Wastewater Using Different Types of Nanomaterials," Accessed: Aug. 02, 2020. [Online]. Available: https://www.researchgate.net/publication/275064304_A_Review_of_Removal_of_Pollutants_from_WaterWastewater_Using_Different_Types_of_Nanomaterials.

[17] I. Beniah Obinna and *Enyoh Christian Ebere, "A review: Water pollution by heavy metal and organic pollutants: Brief review of sources, effects and progress on remediation with aquatic plants," *Anal. Methods Environ. Chem. J.*, vol. 2, no. 3, pp. 5–38, Sep. 2019, doi: 10.24200/amecj.v2.i03.66.

[18] M. Václavíková and M. Vaclavikova, *Water Treatment Technologies for the Removal of High-Toxity Pollutants*, vol. 49, no. 0. 2010.

[19] C. McCullagh, J. M. C. Robertson, D. W. Bahnemann, and P. K. J. Robertson, "The application of TiO2 photocatalysis for disinfection of water contaminated with pathogenic micro-organisms: a review," *Res. Chem. Intermed.*, vol. 33, no. 3–5, pp. 359–375, Mar. 2007, doi: 10.1163/156856707779238775.

[20] W. Jiang, X. Zhang, X. Gong, F. Yan, and Z. Zhang, “Sonochemical synthesis and characterization of magnetic separable Fe 3O4-TiO2 nanocomposites and their catalytic properties,” *Int. J. Smart Nano Mater.*, vol. 1, no. 4, pp. 278–287, 2010, doi: 10.1080/19475411.2010.528873.

[21] A. Dhillon and D. Kumar, *New Generation Nano-Based Adsorbents for Water Purification*. Elsevier Inc., 2018.

[22] P. Z. Ray and H. J. Shipley, “Inorganic nano-adsorbents for the removal of heavy metals and arsenic: a review,” *RSC Adv.*, vol. 5, no. 38, pp. 29885–29907, 2015, doi: 10.1039/C5RA02714D.

[23] R. Singh, S. Singh, P. Parihar, V. P. Singh, and S. M. Prasad, “Arsenic contamination, consequences and remediation techniques: A review,” *Ecotoxicol. Environ. Saf.*, vol. 112, pp. 247–270, 2015, doi: 10.1016/j.ecoenv.2014.10.009.

[24] S. Khashan, S. Dagher, N. Tit, A. Alazzam, and I. Obaidat, “Novel method for synthesis of Fe 3 O 4 @TiO 2 core/shell nanoparticles,” *Surf. Coatings Technol.*, vol. 322, no. October, pp. 92–98, Aug. 2017, doi: 10.1016/j.surfcoat.2017.05.045.

[25] K. K. Kefeni and B. B. Mamba, “Photocatalytic application of spinel ferrite nanoparticles and nanocomposites in wastewater treatment: Review,” *Sustain. Mater. Technol.*, vol. 23, p. e00140, Apr. 2020, doi: 10.1016/j.susmat.2019.e00140.

[26] S. Chowdhury, M. A. J. Mazumder, O. Al-Attas, and T. Husain, “Heavy metals in drinking water: Occurrences, implications, and future needs in developing countries,” *Sci. Total Environ.*, vol. 569–570, pp. 476–488, Nov. 2016, doi: 10.1016/j.scitotenv.2016.06.166.

[27] C. V Mohod and J. Dhote, “Review of Heavy Metals in Drinking Water and Their Effect on Human Health,” *Int. J. Innov. Res. Sci. Eng. Technol.*, vol. 2, no. 7, pp. 2992–2996, 2013.

[28] M. Baláž, Z. Bujňáková, P. Baláž, A. Zorkovská, Z. Danková, and J. Briančin, “Adsorption of cadmium(II) on waste biomaterial,” *J. Colloid Interface Sci.*, vol. 454, pp. 121–133, 2015, doi: 10.1016/j.jcis.2015.03.046.

[29] B. Lellis, C. Z. Fávaro-Polonio, J. A. Pamphile, and J. C. Polonio, “Effects of textile dyes on health and the environment and bioremediation potential of living organisms,” *Biotechnol. Res. Innov.*, vol. 3, no. 2, pp. 275–290, Jul. 2019, doi: 10.1016/j.biori.2019.09.001.

[30] A. Gürses, M. Açıkyıldız, K. Güneş, and M. S. Gürses, “Classification of Dye and Pigments,” pp. 31–45, 2016, doi: 10.1007/978-3-319-33892-7_3.

[31] P. Gregory, “Classification of Dyes by Chemical Structure,” *Chem. Appl. Dye.*, pp. 17–47, 1990, doi: 10.1007/978-1-4684-7715-3_2.

[32] B. D. C. Ventura-camargo and M. A. Marin-morales, “Azo Dyes: Characterization and Toxicity– A Review,” *Text. Light Ind. Sci. Technol.*, no. October, 2013, doi: www.tlist-journal.org.

[33] “Global Apparel Market - Statistics & Facts | Statista.” https://www.statista.com/topics/5091/apparel-market-worldwide/ (accessed Mar. 04, 2021).

[34] A. Desore and S. A. Narula, “An overview on corporate response towards sustainability issues in textile industry,” *Environ. Dev. Sustain.*, vol. 20, no. 4, pp. 1439–1459, Aug. 2018,

doi: 10.1007/s10668-017-9949-1.

[35] A. Yellow, M. Brown, and B. Brown, “3 The chemistry of azo dyes H , N-O-N ~ N-O-N ~ N-b-NH ’,” pp. 21–22, 1971.

[36] R. L. M. Allen, “The chemistry of azo dyes,” in *Colour Chemistry*, Boston, MA: Springer US, 1971, pp. 21–36.

[37] K. M. Norrie, “October 2000,” in *Professor Norrie’s Commentaries on Family Law*, no. October 2000, Edinburgh University Press, 2011, pp. 35–40.

[38] I. J. Puentes-Cárdenas *et al.*, “Adsorptive Removal of Acid Blue 80 Dye from Aqueous Solutions by Cu-TiO2,” *J. Nanomater.*, vol. 2016, 2016, doi: 10.1155/2016/3542359.

[39] S. Afroze and T. K. Sen, “A Review on Heavy Metal Ions and Dye Adsorption from Water by Agricultural Solid Waste Adsorbents,” *Water. Air. Soil Pollut.*, vol. 229, no. 7, 2018, doi: 10.1007/s11270-018-3869-z.

[40] R. V. Kandisa and N. Saibaba KV, “Dye Removal by Adsorption: A Review,” *J. Bioremediation Biodegrad.*, vol. 07, no. 06, 2016, doi: 10.4172/2155-6199.1000371.

[41] M. B., R. Hernandez-Maya, M. Solís-López, C. Th-Th, and V. S., “Photocatalytic degradation of Orange G using TiO2/Fe3O4 nanocomposites,” *J. Mater. Sci. Mater. Electron.*, vol. 29, no. 18, pp. 15436–15444, Sep. 2018, doi: 10.1007/s10854-018-9069-1.

[42] K.-T. Chung, “Azo dyes and human health: A review,” *J. Environ. Sci. Heal. Part C*, vol. 34, no. 4, pp. 233–261, Oct. 2016, doi: 10.1080/10590501.2016.1236602.

[43] E. Weidner and F. Ciesielczyk, “Removal of Hazardous Oxyanions from the Environment Using Metal-Oxide-Based Materials,” *Materials (Basel).*, vol. 12, no. 6, p. 927, Mar. 2019,

doi: 10.3390/ma12060927.

[44] M. A. Barakat, “New trends in removing heavy metals from industrial wastewater,” *Arab. J. Chem.*, vol. 4, no. 4, pp. 361–377, 2011, doi: 10.1016/j.arabjc.2010.07.019.

[45] R. W. Herschy, “Water Quality for Drinking: WHO Guidelines,” in *Encyclopedia of Earth Sciences Series*, 2012, pp. 876–883.

[46] C. Ucar, M. B. Baskan, and A. Pala, “Arsenic removal from drinking water by electrocoagulation using iron electrodes,” *Korean J. Chem. Eng.*, vol. 30, no. 10, pp. 1889–1895, Oct. 2013, doi: 10.1007/s11814-013-0128-2.

[47] R. K. Gautam, S. K. Sharma, S. Mahiya, and M. C. Chattopadhyaya, “CHAPTER 1. Contamination of Heavy Metals in Aquatic Media: Transport, Toxicity and Technologies for Remediation,” in *Heavy Metals In Water*, Cambridge: Royal Society of Chemistry, 2014, pp. 1–24.

[48] H. Erdogan, Ö. Yalçinkaya, and A. R. Türker, “Determination of inorganic arsenic species by hydride generation atomic absorption spectrometry in water samples after preconcentration/separation on nano ZrO2/B2O3 by solid phase extraction,” *Desalination*, vol. 280, no. 1–3, pp. 391–396, 2011, doi: 10.1016/j.desal.2011.07.029.

[49] C. K. Jain and R. D. Singh, “Technological options for the removal of arsenic with special reference to South East Asia,” *J. Environ. Manage.*, vol. 107, pp. 1–18, Sep. 2012, doi: 10.1016/j.jenvman.2012.04.016.

[50] E. Stopelli *et al.*, “Spatial and temporal evolution of groundwater arsenic contamination in the Red River delta, Vietnam: Interplay of mobilisation and retardation processes,” *Sci.*

Total Environ., vol. 717, p. 137143, May 2020, doi: 10.1016/j.scitotenv.2020.137143.

[51] G. Gong, S. Mattevada, and S. E. O'Bryant, "Comparison of the accuracy of kriging and IDW interpolations in estimating groundwater arsenic concentrations in Texas," *Environ. Res.*, vol. 130, pp. 59–69, Apr. 2014, doi: 10.1016/j.envres.2013.12.005.

[52] S. Bhowmick, S. Pramanik, P. Singh, P. Mondal, D. Chatterjee, and J. Nriagu, "Arsenic in groundwater of West Bengal, India: A review of human health risks and assessment of possible intervention options," *Sci. Total Environ.*, vol. 612, pp. 148–169, Jan. 2018, doi: 10.1016/j.scitotenv.2017.08.216.

[53] M. A. Hashim *et al.*, "Arsenic removal by adsorption on activated carbon in a rotating packed bed," *J. Water Process Eng.*, vol. 30, no. March, p. 100591, Aug. 2019, doi: 10.1016/j.jwpe.2018.03.006.

[54] J. PARGA *et al.*, "Arsenic removal via electrocoagulation from heavy metal contaminated groundwater in La Comarca Lagunera México," *J. Hazard. Mater.*, vol. 124, no. 1–3, pp. 247–254, Sep. 2005, doi: 10.1016/j.jhazmat.2005.05.017.

[55] Y. Xu, Y. Dai, J. Zhou, Z. P. Xu, G. Qian, and G. Q. M. Lu, "Removal efficiency of arsenate and phosphate from aqueous solution using layered double hydroxide materials: intercalation vs. precipitation," *J. Mater. Chem.*, vol. 20, no. 22, p. 4684, 2010, doi: 10.1039/b926239c.

[56] D. D. La, H. P. N. Thi, T. A. Nguyen, and S. V. Bhosale, "Effective removal of Pb(<scp>ii</scp>) using a graphene@ternary oxides composite as an adsorbent in aqueous media," *New J. Chem.*, vol. 41, no. 23, pp. 14627–14634, 2017, doi: 10.1039/C7NJ03064A.

[57] C. Suryanarayana, “Mechanical alloying and milling,” *Prog. Mater. Sci.*, vol. 46, no. 1–2, pp. 1–184, 2001, doi: 10.1016/S0079-6425(99)00010-9.

[58] M. Lim, G.-C. Han, J.-W. Ahn, K.-S. You, and H.-S. Kim, “Leachability of Arsenic and Heavy Metals from Mine Tailings of Abandoned Metal Mines,” *Int. J. Environ. Res. Public Health*, vol. 6, no. 11, pp. 2865–2879, Nov. 2009, doi: 10.3390/ijerph6112865.

[59] T. Basu and U. C. Ghosh, “Influence of groundwater occurring ions on the kinetics of As(III) adsorption reaction with synthetic nanostructured Fe(III)–Cr(III) mixed oxide,” *Desalination*, vol. 266, no. 1–3, pp. 25–32, Jan. 2011, doi: 10.1016/j.desal.2010.07.064.

[60] E. Gutiérrez-Segura, M. Solache-Ríos, A. Colín-Cruz, and C. Fall, “Adsorption of cadmium by Na and Fe modified zeolitic tuffs and carbonaceous material from pyrolyzed sewage sludge,” *J. Environ. Manage.*, vol. 97, no. 1, pp. 6–13, Apr. 2012, doi: 10.1016/j.jenvman.2011.11.010.

[61] M. A. Alaei Shahmirzadi, S. S. Hosseini, J. Luo, and I. Ortiz, “Significance, evolution and recent advances in adsorption technology, materials and processes for desalination, water softening and salt removal,” *J. Environ. Manage.*, vol. 215, pp. 324–344, Jun. 2018, doi: 10.1016/j.jenvman.2018.03.040.

[62] S. Ahamed, A. Hussam, and A. K. M. Munir, “Groundwater Arsenic Removal Technologies Based on Sorbents,” in *Handbook of Water Purity and Quality*, Elsevier, 2009, pp. 379–417.

[63] S. D. Kelly, “and Sediments,” *Dev. Soil Sci.*, vol. 34, pp. 411–466, 2010, [Online]. Available: http://dx.doi.org/10.1016/S0166-2481(10)34014-1.

[64] N. Chakrabarty, *Arsenic Toxicity*, vol. 7, no. 7. CRC Press, 2015.

[65] M. Shahid, C. Dumat, N. Khan Niazi, S. Khalid, and Natasha, "Global scale arsenic pollution : increase the scientific knowledge to reduce human exposure," *VertigO*, no. Hors-série 31, Sep. 2018, doi: 10.4000/vertigo.21331.

[66] S. Lata and S. R. Samadder, "Removal of arsenic from water using nano adsorbents and challenges: A review," *J. Environ. Manage.*, vol. 166, no. 1, pp. 387–406, Jan. 2016, doi: 10.1016/j.jenvman.2015.10.039.

[67] F. Kabir and S. Chowdhury, "Arsenic removal methods for drinking water in the developing countries: technological developments and research needs," *Environ. Sci. Pollut. Res.*, vol. 24, no. 31, pp. 24102–24120, Nov. 2017, doi: 10.1007/s11356-017-0240-7.

[68] E. Çermikli *et al.*, "Performances of novel chelating ion exchange resins for boron and arsenic removal from saline geothermal water using adsorption-membrane filtration hybrid process," *Desalination*, vol. 491, p. 114504, Oct. 2020, doi: 10.1016/j.desal.2020.114504.

[69] M. Pessoa Lopes, C. F. Galinha, J. G. Crespo, and S. Velizarov, "Optimisation of arsenate removal from water by an integrated ion-exchange membrane process coupled with Fe co-precipitation," *Sep. Purif. Technol.*, vol. 246, p. 116894, Sep. 2020, doi: 10.1016/j.seppur.2020.116894.

[70] A. Abejón, A. Garea, and A. Irabien, "Arsenic removal from drinking water by reverse osmosis: Minimization of costs and energy consumption," *Sep. Purif. Technol.*, vol. 144, pp. 46–53, Apr. 2015, doi: 10.1016/j.seppur.2015.02.017.

[71] "Chemical Precipitation - an overview | ScienceDirect Topics."

https://www.sciencedirect.com/topics/engineering/chemical-precipitation (accessed Feb. 02, 2021).

[72] J. Gregory and R. . Dhond, “Wastewater treatment by ion exchange,” *Water Res.*, vol. 6, no. 6, pp. 681–694, Jun. 1972, doi: 10.1016/0043-1354(72)90183-2.

[73] A. Tahreen, M. S. Jami, and F. Ali, “Role of electrocoagulation in wastewater treatment: A developmental review,” *J. Water Process Eng.*, vol. 37, p. 101440, Oct. 2020, doi: 10.1016/j.jwpe.2020.101440.

[74] R. Saravanan, F. Gracia, and A. Stephen, “Basic Principles, Mechanism, and Challenges of Photocatalysis,” 2017, pp. 19–40.

[75] D. Harikishore Kumar Reddy, K. Vijayaraghavan, J. A. Kim, and Y.-S. Yun, “Valorisation of post-sorption materials: Opportunities, strategies, and challenges,” *Adv. Colloid Interface Sci.*, vol. 242, pp. 35–58, Apr. 2017, doi: 10.1016/j.cis.2016.12.002.

[76] A. Elena *et al.*, “Waste Water Treatment Methods,” in *Water Treatment*, no. tourism, InTech, 2013, p. 13.

[77] A. Ibhadon and P. Fitzpatrick, “Heterogeneous Photocatalysis: Recent Advances and Applications,” *Catalysts*, vol. 3, no. 1, pp. 189–218, Mar. 2013, doi: 10.3390/catal3010189.

[78] S. A. Messele, F. Stüber, C. Bengoa, A. Fortuny, A. Fabregat, and J. Font, “Phenol Degradation by Heterogeneous Fenton-Like Reaction Using Fe Supported Over Activated Carbon,” *Procedia Eng.*, vol. 42, pp. 1373–1377, Jan. 2012, doi: 10.1016/j.proeng.2012.07.529.

[79] A. Ikekawa, M. Kamiya, Y. Fujita, and T. Kwan, “On the Competition of Homogeneous

and Heterogeneous Chain Terminations in Heterogeneous Photooxidation Catalysis by Zinc Oxide," *Bull. Chem. Soc. Jpn.*, vol. 38, no. 1, pp. 32–36, Jan. 1965, doi: 10.1246/bcsj.38.32.

[80] F. T. Wagner and G. A. Somorjai, "Photocatalytic and photoelectrochemical hydrogen production on strontium titanate single crystals," *J. Am. Chem. Soc.*, vol. 102, no. 17, pp. 5494–5502, Aug. 1980, doi: 10.1021/ja00537a013.

[81] X.-L. Dong *et al.*, "Preparation of CdS–TiO2/Fe3O4 photocatalyst and its photocatalytic properties," *J. Sol-Gel Sci. Technol.*, vol. 66, no. 2, pp. 231–237, May 2013, doi: 10.1007/s10971-013-2998-5.

[82] R. Venkatesan, S. Velumani, K. Ordon, M. Makowska-Janusik, G. Corbel, and A. Kassiba, "Structural and morphological data of RF-Sputtered BiVO4 thin films," *Data Br.*, vol. 17, pp. 526–528, Apr. 2018, doi: 10.1016/j.dib.2018.01.070.

[83] X. Yang, L. Zhang, Z. Chen, H. Jing, Y. Chen, and Q. Li, "Synthesis of magnetic photocatalyst and sensitization properties of polypyrrole," *Sci. Eng. Compos. Mater.*, vol. 23, no. 3, pp. 269–275, May 2016, doi: 10.1515/secm-2014-0035.

[84] M. M. Khan, S. F. Adil, and A. Al-Mayouf, "Metal oxides as photocatalysts," *J. Saudi Chem. Soc.*, vol. 19, no. 5, pp. 462–464, Sep. 2015, doi: 10.1016/j.jscs.2015.04.003.

[85] M. N. Chong, B. Jin, C. W. Chow, and C. Saint, "Recent developments in photocatalytic water treatment technology: A review," *Water Res.*, vol. 44, no. 10, pp. 2997–3027, May 2010, doi: 10.1016/j.watres.2010.02.039.

[86] J. Moma and J. Baloyi, "Modified Titanium Dioxide for Photocatalytic Applications," in *Photocatalysts - Applications and Attributes*, IntechOpen, 2019.

[87] V. Etacheri, C. Di Valentin, J. Schneider, D. Bahnemann, and S. C. Pillai, “Visible-light activation of TiO2 photocatalysts: Advances in theory and experiments,” *J. Photochem. Photobiol. C Photochem. Rev.*, vol. 25, pp. 1–29, 2015, doi: 10.1016/j.jphotochemrev.2015.08.003.

[88] E. jbes Kowsari, “Semiconductor Nanocomposites for application of Photocatalysis,” pp. 203–249, 2016, doi: 10.1007/978-3-319-62446-4.

[89] Y.-S. Li, J. S. Church, and A. L. Woodhead, “Infrared and Raman spectroscopic studies on iron oxide magnetic nano-particles and their surface modifications,” *J. Magn. Magn. Mater.*, vol. 324, no. 8, pp. 1543–1550, Apr. 2012, doi: 10.1016/j.jmmm.2011.11.065.

[90] V. Etacheri, C. Di Valentin, J. Schneider, D. Bahnemann, and S. C. Pillai, “Visible-light activation of TiO2 photocatalysts: Advances in theory and experiments,” *J. Photochem. Photobiol. C Photochem. Rev.*, vol. 25, pp. 1–29, Dec. 2015, doi: 10.1016/j.jphotochemrev.2015.08.003.

[91] J. Zhang, P. Zhou, J. Liu, and J. Yu, “New understanding of the difference of photocatalytic activity among anatase, rutile and brookite TiO 2,” *Phys. Chem. Chem. Phys.*, vol. 16, no. 38, pp. 20382–20386, Aug. 2014, doi: 10.1039/C4CP02201G.

[92] L. E. Oi, M.-Y. Choo, H. V. Lee, H. C. Ong, S. B. A. Hamid, and J. C. Juan, “Recent advances of titanium dioxide (TiO 2) for green organic synthesis,” *RSC Adv.*, vol. 6, no. 110, pp. 108741–108754, 2016, doi: 10.1039/C6RA22894A.

[93] S. M. Gupta and M. Tripathi, “A review of TiO2 nanoparticles,” *Chinese Sci. Bull.*, vol. 56, no. 16, pp. 1639–1657, 2011, doi: 10.1007/s11434-011-4476-1.

[94] W. Wu, Q. He, and C. Jiang, “Magnetic Iron Oxide Nanoparticles: Synthesis and Surface Functionalization Strategies,” *Nanoscale Res. Lett.*, vol. 3, no. 11, pp. 397–415, Nov. 2008, doi: 10.1007/s11671-008-9174-9.

[95] A. K. Gupta and M. Gupta, “Synthesis and surface engineering of iron oxide nanoparticles for biomedical applications,” *Biomaterials*, vol. 26, no. 18, pp. 3995–4021, Jun. 2005, doi: 10.1016/j.biomaterials.2004.10.012.

[96] L. Liu, H. Zhao, J. M. Andino, and Y. Li, “Photocatalytic CO 2 Reduction with H 2 O on TiO 2 Nanocrystals: Comparison of Anatase, Rutile, and Brookite Polymorphs and Exploration of Surface Chemistry,” *ACS Catal.*, vol. 2, no. 8, pp. 1817–1828, Aug. 2012, doi: 10.1021/cs300273q.

[97] A. Y. Ahmed, T. A. Kandiel, T. Oekermann, and D. Bahnemann, “Photocatalytic Activities of Different Well-defined Single Crystal TiO 2 Surfaces: Anatase versus Rutile,” *J. Phys. Chem. Lett.*, vol. 2, no. 19, pp. 2461–2465, Oct. 2011, doi: 10.1021/jz201156b.

[98] T. Luttrell, S. Halpegamage, J. Tao, A. Kramer, E. Sutter, and M. Batzill, “Why is anatase a better photocatalyst than rutile? - Model studies on epitaxial TiO2 films,” *Sci. Rep.*, vol. 4, no. 1, p. 4043, May 2015, doi: 10.1038/srep04043.

[99] J. Zhan, H. Zhang, and G. Zhu, “Magnetic photocatalysts of cenospheres coated with Fe3O4/TiO2 core/shell nanoparticles decorated with Ag nanopartilces,” *Ceram. Int.*, vol. 40, no. 6, pp. 8547–8559, Jul. 2014, doi: 10.1016/j.ceramint.2014.01.069.

[100] S. Mohammadi-Aghdam, B. Sarkhosh, and N. N. Tajoddin, “Recyclable Fe3O4/SiO2/TiO2/Cu nanocomposites: synthesis, characterization and investigation of the photocatalytic and magnetic property,” *J. Mater. Sci. Mater. Electron.*, vol. 28, no. 13, pp.

9456–9463, Jul. 2017, doi: 10.1007/s10854-017-6688-x.

[101] S. Bagheri and N. M. Julkapli, “Magnetite hybrid photocatalysis: advance environmental remediation,” *Rev. Inorg. Chem.*, vol. 36, no. 3, pp. 135–151, Jan. 2016, doi: 10.1515/revic-2015-0014.

[102] Z. Liu, H. Bai, and D. D. Sun, “Facile fabrication of porous chitosan/TiO 2 /Fe 3 O 4 microspheres with multifunction for water purifications,” *New J. Chem.*, vol. 35, no. 1, pp. 137–140, Jan. 2011, doi: 10.1039/C0NJ00593B.

[103] Z. Li, L. Cheng, S. Zhang, Z. Wang, and C. Fu, “Enhanced photocatalytic and magnetic recovery performance of Co-doped BiFeO3 based on MOFs precursor,” *J. Solid State Chem.*, vol. 279, p. 120978, Nov. 2019, doi: 10.1016/j.jssc.2019.120978.

[104] A. S. Teja and P.-Y. Koh, “Synthesis, properties, and applications of magnetic iron oxide nanoparticles,” *Prog. Cryst. Growth Charact. Mater.*, vol. 55, no. 1–2, pp. 22–45, Mar. 2009, doi: 10.1016/j.pcrysgrow.2008.08.003.

[105] V. M. Vinosel *et al.*, “Enhanced photocatalytic activity of Fe3O4/SnO2 magnetic nanocomposite for the degradation of organic dye,” *J. Mater. Sci. Mater. Electron.*, vol. 30, no. 10, pp. 9663–9677, May 2019, doi: 10.1007/s10854-019-01300-5.

[106] P. Bhavani, N. R. Reddy, I. V. S. Reddy, and M. Sakar, “Manipulation Over Phase Transformation in Iron Oxide Nanoparticles via Calcination Temperature and Their Effect on Magnetic and Dielectric Properties,” *IEEE Trans. Magn.*, vol. 53, no. 9, pp. 1–5, Sep. 2017, doi: 10.1109/TMAG.2017.2715320.

[107] E. A. Campos, D. V. B. Stockler Pinto, J. I. S. de Oliveira, E. da C. Mattos, and R. de C. L.

Dutra, “Synthesis, Characterization and Applications of Iron Oxide Nanoparticles - a Short Review,” *J. Aerosp. Technol. Manag.*, vol. 7, no. 3, pp. 267–276, Sep. 2015, doi: 10.5028/jatm.v7i3.471.

[108] S.-M. Zhou, S.-Y. Lou, Y.-Q. Wang, X.-L. Chen, L.-S. Liu, and H.-L. Yuan, “Preparation of Cu-doped γ-Fe 2 O 3 nanowires with high coercivity by chemical vapor deposition,” *J. Mater. Res.*, vol. 26, no. 13, pp. 1634–1638, Jul. 2011, doi: 10.1557/jmr.2011.129.

[109] J. Tucek, S. Ohkoshi, and R. Zboril, “Room-temperature ground magnetic state of ε-Fe 2 O 3 : In-field Mössbauer spectroscopy evidence for collinear ferrimagnet,” *Appl. Phys. Lett.*, vol. 99, no. 25, p. 253108, Dec. 2011, doi: 10.1063/1.3671114.

[110] I. Dzyaloshinsky, “A thermodynamic theory of ‘weak’ ferromagnetism of antiferromagnetics,” *J. Phys. Chem. Solids*, vol. 4, no. 4, pp. 241–255, Jan. 1958, doi: 10.1016/0022-3697(58)90076-3.

[111] T. Moriya, “Anisotropic Superexchange Interaction and Weak Ferromagnetism,” *Phys. Rev.*, vol. 120, no. 1, pp. 91–98, Oct. 1960, doi: 10.1103/PhysRev.120.91.

[112] L. Néel, “Antiferromagnetism and Ferrimagnetism,” *Proc. Phys. Soc. Sect. A*, vol. 65, no. 11, pp. 869–885, Nov. 1952, doi: 10.1088/0370-1298/65/11/301.

[113] A. M. Jubb and H. C. Allen, “Vibrational Spectroscopic Characterization of Hematite, Maghemite, and Magnetite Thin Films Produced by Vapor Deposition,” *ACS Appl. Mater. Interfaces*, vol. 2, no. 10, pp. 2804–2812, Oct. 2010, doi: 10.1021/am1004943.

[114] S. I. Siddiqui and S. A. Chaudhry, “Iron oxide and its modified forms as an adsorbent for arsenic removal: A comprehensive recent advancement,” *Process Saf. Environ. Prot.*, vol.

111, no. August 2017, pp. 592–626, 2017, doi: 10.1016/j.psep.2017.08.009.

[115] A. Ali *et al.*, "Synthesis, characterization, applications, and challenges of iron oxide nanoparticles," *Nanotechnol. Sci. Appl.*, vol. Volume 9, pp. 49–67, Aug. 2016, doi: 10.2147/NSA.S99986.

[116] M. M. Mohamed, W. A. Bayoumy, M. E. Goher, M. H. Abdo, and T. Y. Mansour El-Ashkar, "Optimization of α-Fe 2 O 3 @Fe 3 O 4 incorporated N-TiO 2 as super effective photocatalysts under visible light irradiation," *Appl. Surf. Sci.*, vol. 412, pp. 668–682, Aug. 2017, doi: 10.1016/j.apsusc.2017.03.200.

[117] H. Fu *et al.*, "A facile coating method to construct uniform porous α-Fe2O3@TiO2 core-shell nanostructures with enhanced solar light photocatalytic activity," *Powder Technol.*, vol. 328, pp. 389–396, Apr. 2018, doi: 10.1016/j.powtec.2018.01.067.

[118] W. Wu, X. Xiao, S. Zhang, F. Ren, and C. Jiang, "Facile method to synthesize magnetic iron oxides/TiO2 hybrid nanoparticles and their photodegradation application of methylene blue," *Nanoscale Res. Lett.*, vol. 6, no. 1, p. 533, 2011, doi: 10.1186/1556-276X-6-533.

[119] D. Beydoun, R. Amal, G. K. C. Low, and S. McEvoy, "Novel Photocatalyst: Titania-Coated Magnetite. Activity and Photodissolution," *J. Phys. Chem. B*, vol. 104, no. 18, pp. 4387–4396, May 2000, doi: 10.1021/jp992088c.

[120] Z. Özlem Kocabaş-Ataklı and Y. Yürüm, "Synthesis and characterization of anatase nanoadsorbent and application in removal of lead, copper and arsenic from water," *Chem. Eng. J.*, vol. 225, pp. 625–635, Jun. 2013, doi: 10.1016/j.cej.2013.03.106.

[121] F. Ferrero, "Dye removal from aqueous solution using coal fly ash for continuous flow

adsorption," *Clean Technol. Environ. Policy*, vol. 17, no. 7, pp. 1907–1915, 2015, doi: 10.1007/s10098-015-0908-y.

[122] G. Crini, "Non-conventional low-cost adsorbents for dye removal: A review," *Bioresour. Technol.*, vol. 97, no. 9, pp. 1061–1085, 2006, doi: 10.1016/j.biortech.2005.05.001.

[123] N. B. Singh, G. Nagpal, S. Agrawal, and Rachna, "Water purification by using Adsorbents: A Review," *Environ. Technol. Innov.*, vol. 11, pp. 187–240, Aug. 2018, doi: 10.1016/j.eti.2018.05.006.

[124] T. Tadros, "Adsorption Isotherm," in *Encyclopedia of Colloid and Interface Science*, Berlin, Heidelberg: Springer Berlin Heidelberg, 2013, pp. 2–2.

[125] N. Ayawei, A. N. Ebelegi, and D. Wankasi, "Modelling and Interpretation of Adsorption Isotherms," *J. Chem.*, vol. 2017, pp. 1–11, 2017, doi: 10.1155/2017/3039817.

[126] R. T. M. Dharmendirakumar, G.Vijayakumar, G. Vijayakumar, R. Tamilarasan, and M. Dharmendirakumar, "Adsorption , Kinetic , Equilibrium and Thermodynamic studies on the removal of basic dye Rhodamine-B from ...," *J. Mater. Environ. Sci.*, vol. 3, no. June, pp. 157–170, 2015.

[127] S. Nethaji, A. Sivasamy, and A. B. Mandal, "Adsorption isotherms, kinetics and mechanism for the adsorption of cationic and anionic dyes onto carbonaceous particles prepared from Juglans regia shell biomass," *Int. J. Environ. Sci. Technol.*, vol. 10, no. 2, pp. 231–242, 2013, doi: 10.1007/s13762-012-0112-0.

[128] P. Pandey, S. S. Sambi, S. K. Sharma, and S. Singh, "Batch Adsorption Studies for the Removal of Cu(II) Ions by ZeoliteNaX from Aqueous Stream," *Lect. Notes Eng. Comput.*

Sci., vol. 2178, no. 1, pp. 122–127, 2009.

[129] S. Lata and S. R. Samadder, "Removal of arsenic from water using nano adsorbents and challenges: A review," *J. Environ. Manage.*, vol. 166, pp. 387–406, Jan. 2016, doi: 10.1016/j.jenvman.2015.10.039.

[130] S. I. Siddiqui and S. A. Chaudhry, "Iron oxide and its modified forms as an adsorbent for arsenic removal: A comprehensive recent advancement," *Process Saf. Environ. Prot.*, vol. 111, pp. 592–626, 2017, doi: 10.1016/j.psep.2017.08.009.

[131] D. D. La, T. A. Nguyen, L. A. Jones, and S. V. Bhosale, "Graphene-Supported spinel CuFe2O4 composites: Novel adsorbents for arsenic removal in aqueous media," *Sensors (Switzerland)*, vol. 17, no. 6, 2017, doi: 10.3390/s17061292.

[132] D. D. La, J. M. Patwari, L. A. Jones, F. Antolasic, and S. V. Bhosale, "Fabrication of a GNP/Fe-Mg Binary Oxide Composite for Effective Removal of Arsenic from Aqueous Solution," *ACS Omega*, vol. 2, no. 1, pp. 218–226, 2017, doi: 10.1021/acsomega.6b00304.

[133] W. Zhou *et al.*, "Mesoporous TiO 2 /α-Fe 2 O 3 : Bifunctional Composites for Effective Elimination of Arsenite Contamination through Simultaneous Photocatalytic Oxidation and Adsorption," *J. Phys. Chem. C*, vol. 112, no. 49, pp. 19584–19589, Dec. 2008, doi: 10.1021/jp806594m.

[134] M. C. Ceballos-Chuc, C. M. Ramos-Castillo, J. J. Alvarado-Gil, G. Oskam, and G. Rodríguez-Gattorno, "Influence of Brookite Impurities on the Raman Spectrum of TiO 2 Anatase Nanocrystals," *J. Phys. Chem. C*, vol. 122, no. 34, pp. 19921–19930, Aug. 2018, doi: 10.1021/acs.jpcc.8b04987.

[135] M. J. Uddin and Y.-K. Jeong, “Review: Efficiently performing periodic elements with modern adsorption technologies for arsenic removal,” *Environ. Sci. Pollut. Res.*, vol. 27, no. 32, pp. 39888–39912, Nov. 2020, doi: 10.1007/s11356-020-10323-z.

[136] J. Miao, R. Zhang, and L. Zhang, “Photocatalytic degradations of three dyes with different chemical structures using ball-milled TiO2,” *Mater. Res. Bull.*, vol. 97, no. January 2017, pp. 109–114, 2018, doi: 10.1016/j.materresbull.2017.08.032.

[137] L. B. Kong, J. Ma, H. Huang, and R. F. Zhang, “Effect of excess PbO on microstructure and electrical properties of PLZT7/60/40 ceramics derived from a high-energy ball milling process,” *J. Alloys Compd.*, vol. 345, no. 1–2, pp. 238–245, 2002, doi: 10.1016/S0925-8388(02)00400-0.

[138] Q. Han, R. Setchi, and S. L. Evans, “Synthesis and characterisation of advanced ball-milled Al-Al2O3 nanocomposites for selective laser melting,” *Powder Technol.*, vol. 297, pp. 183–192, 2016, doi: 10.1016/j.powtec.2016.04.015.

[139] M. I. Dar and S. A. Shivashankar, “Single crystalline magnetite, maghemite, and hematite nanoparticles with rich coercivity,” *RSC Adv.*, vol. 4, no. 8, pp. 4105–4113, 2014, doi: 10.1039/C3RA45457F.

[140] R. Nisticò, “A synthetic guide toward the tailored production of magnetic iron oxide nanoparticles,” *Boletín la Soc. Española Cerámica y Vidr.*, pp. 1–12, Feb. 2020, doi: 10.1016/j.bsecv.2020.01.011.

[141] R. Grau-Crespo, A. Y. Al-Baitai, I. Saadoune, and N. H. De Leeuw, “Vacancy ordering and electronic structure of γ - Fe 2 O 3 (maghemite): a theoretical investigation,” *J. Phys. Condens. Matter*, vol. 22, no. 25, p. 255401, Jun. 2010, doi: 10.1088/0953-

8984/22/25/255401.

[142] J. T. Mayo *et al.*, "The effect of nanocrystalline magnetite size on arsenic removal," *Sci. Technol. Adv. Mater.*, vol. 8, no. 1–2, pp. 71–75, Jan. 2007, doi: 10.1016/j.stam.2006.10.005.

[143] P. N. Dave and L. V. Chopda, "Application of iron oxide nanomaterials for the removal of heavy metals," *J. Nanotechnol.*, vol. 2014, 2014, doi: 10.1155/2014/398569.

[144] L. Cumbal and A. K. SenGupta, "Arsenic Removal Using Polymer-Supported Hydrated Iron(III) Oxide Nanoparticles: Role of Donnan Membrane Effect †," *Environ. Sci. Technol.*, vol. 39, no. 17, pp. 6508–6515, Sep. 2005, doi: 10.1021/es050175e.

[145] T. T. Bui, X. Q. Le, D. P. To, and V. T. Nguyen, "Investigation of typical properties of nanocrystalline iron powders prepared by ball milling techniques," *Adv. Nat. Sci. Nanosci. Nanotechnol.*, vol. 4, no. 4, p. 045003, Aug. 2013, doi: 10.1088/2043-6262/4/4/045003.

[146] R. M. El-sherif, T. A. Lasheen, and E. A. Jebril, "Fabrication and characterization of CeO 2 -TiO 2 -Fe 2 O 3 magnetic nanoparticles for rapid removal of uranium ions from industrial waste solutions," *J. Mol. Liq.*, vol. 241, pp. 260–269, Sep. 2017, doi: 10.1016/j.molliq.2017.05.119.

[147] M. M. A. El-Latif, A. M. Ibrahim, M. S. Showman, and R. R. A. Hamide, "Alumina/Iron Oxide Nano Composite for Cadmium Ions Removal from Aqueous Solutions," *Int. J. Nonferrous Metall.*, vol. 02, no. 02, pp. 47–62, 2013, doi: 10.4236/ijnm.2013.22007.

[148] P. Mondal, C. B. Majumder, and B. Mohanty, "Effects of adsorbent dose, its particle size and initial arsenic concentration on the removal of arsenic, iron and manganese from

simulated ground water by Fe3+ impregnated activated carbon," *J. Hazard. Mater.*, vol. 150, no. 3, pp. 695–702, Feb. 2008, doi: 10.1016/j.jhazmat.2007.05.040.

[149] C. Kütahyali, Ş. Sert, B. Çetinkaya, S. Inan, and M. Eral, "Factors Affecting Lanthanum and Cerium Biosorption on Pinus brutia Leaf Powder," *Sep. Sci. Technol.*, vol. 45, no. 10, pp. 1456–1462, Jun. 2010, doi: 10.1080/01496391003674266.

[150] A. Esposito, F. Pagnanelli, A. Lodi, C. Solisio, and F. Vegliò, "Biosorption of heavy metals by Sphaerotilus natans: an equilibrium study at different pH and biomass concentrations," *Hydrometallurgy*, vol. 60, no. 2, pp. 129–141, Apr. 2001, doi: 10.1016/S0304-386X(00)00195-X.

[151] N. Das and D. Das, "Recovery of rare earth metals through biosorption: An overview," *J. Rare Earths*, vol. 31, no. 10, pp. 933–943, Oct. 2013, doi: 10.1016/S1002-0721(13)60009-5.

[152] J. Xie, Y. Lin, C. Li, D. Wu, and H. Kong, "Removal and recovery of phosphate from water by activated aluminum oxide and lanthanum oxide," *Powder Technol.*, vol. 269, pp. 351–357, Jan. 2015, doi: 10.1016/j.powtec.2014.09.024.

[153] M. Torab-Mostaedi, M. Asadollahzadeh, A. Hemmati, and A. Khosravi, "Biosorption of lanthanum and cerium from aqueous solutions by grapefruit peel: equilibrium, kinetic and thermodynamic studies," *Res. Chem. Intermed.*, vol. 41, no. 2, pp. 559–573, Feb. 2015, doi: 10.1007/s11164-013-1210-4.

[154] S. Iftekhar, D. L. Ramasamy, V. Srivastava, M. B. Asif, and M. Sillanpää, "Understanding the factors affecting the adsorption of Lanthanum using different adsorbents: A critical review," *Chemosphere*, vol. 204, pp. 413–430, Aug. 2018, doi:

10.1016/j.chemosphere.2018.04.053.

[155] B. Z. Can, R. Boncukcuoglu, A. E. Yilmaz, and B. A. Fil, "Effect of some operational parameters on the arsenic removal by electrocoagulation using iron electrodes," *J. Environ. Heal. Sci. Eng.*, vol. 12, no. 1, p. 95, Dec. 2014, doi: https://doi.org/10.1007/s40097-021-00388-8.

[156] R. Cornell and U. Schwertmann, "Colour Plates," in *The Iron Oxides*, Wiley, 2003.

[157] S. Lin, J. Jin, S. Sun, and J. Yu, "Removal of arsenic contaminants using a novel porous nanoadsorbent with superior magnetic recovery," *Chem. Eng. Sci. X*, vol. 8, p. 100069, Nov. 2020, doi: 10.1016/j.cesx.2020.100069.

[158] S. A. Chaudhry, M. Ahmed, S. I. Siddiqui, and S. Ahmed, "Fe(III)–Sn(IV) mixed binary oxide-coated sand preparation and its use for the removal of As(III) and As(V) from water: Application of isotherm, kinetic and thermodynamics," *J. Mol. Liq.*, vol. 224, pp. 431–441, Dec. 2016, doi: 10.1016/j.molliq.2016.08.116.

[159] G. Zhang, Z. Ren, X. Zhang, and J. Chen, "Nanostructured iron(III)-copper(II) binary oxide: A novel adsorbent for enhanced arsenic removal from aqueous solutions," *Water Res.*, vol. 47, no. 12, pp. 4022–4031, Aug. 2013, doi: 10.1016/j.watres.2012.11.059.

[160] C. Zhang, C. Shan, Y. Jin, and M. Tong, "Enhanced removal of trace arsenate by magnetic nanoparticles modified with arginine and lysine," *Chem. Eng. J.*, vol. 254, pp. 340–348, Oct. 2014, doi: 10.1016/j.cej.2014.05.133.

[161] F. Beduk, "Superparamagnetic nanomaterial Fe 3 O 4 –TiO 2 for the removal of As(V) and As(III) from aqueous solutions," *Environ. Technol.*, vol. 37, no. 14, pp. 1790–1801, Jul.

2016, doi: 10.1080/09593330.2015.1132777.

[162] V. Srivastava, Y. C. Sharma, and M. Sillanpää, “Green synthesis of magnesium oxide nanoflower and its application for the removal of divalent metallic species from synthetic wastewater,” *Ceram. Int.*, vol. 41, no. 5, pp. 6702–6709, Jun. 2015, doi: 10.1016/j.ceramint.2015.01.112.

2. CHAPTER 2 - EXPERIMENTAL AND CHARACTERIZATION TECHNIQUES

2.1 Experimental methods

2.1.1 Materials

All the chemicals used in this work were analytical grade and purchased from Sigma-Aldrich, Mexico, and used without any further purification. Iron (III) chloride hexahydrate, ($FeCl_3 \cdot 6H_2O$, ≥98%), Iron (II) chloride tetrahydrate ($FeCl_2 \cdot 4H_2O$, ≥99.0%), Ammonium hydroxide (NH_4OH, 28-30% NH_3 basis), Ethanol ($C_2H_5O_H$), Titanium chloride, $TiCl_4$ (99.9%), Arsenic (III) oxide (AS_2O_3, ≥99.0%), Sodium arsenate dibasic heptahydrate ($HAsNa_2O_4.7H_2O$, ≥ 98.0%), Ammonium molybdate tetrahydrate ($H_{24}MO_7N_8O_{24}.4H_2O$, 99.98), Potassium antimonyl tartrate trihydrate ($C_8H_4K_2O_{12}Sb_2.3H_2O$, ≥99%), Potassium permanganate ($KMnO_4$, ≥99%), sodium hydroxide (NaOH, ≥ 98%), L-ascorbic acid ($C_6H_8O_6$), Sulphuric acid (H_2SO_4), Hydrochloric acid (HCl) and Acetic acid (CH_3COOH). The nitrogen gas cylinder (99.99% purity) was bought from INFRA, Mexico. MA-type PM400, Retsch ball mill, was used for the milling studies. The deionized water was used throughout the experiment.

2.1.2 Iron oxide synthesis using co-precipitation method

Among various synthesizing methods for iron-oxide nanoparticles, the co-precipitation method is considered the best due to,

- High productivity and good dispersed NPs [1].

- For the iron oxide synthesis, It is the simplest and effective chemical path to obtain magnetic nanoparticles because it offers a room temperature substitute to traditional powder synthesis techniques in the preparation of NPs [2].
- This method results in Iron oxide NPs with a large surface-to-volume ratio and high surface energies, with iron oxide NPs smaller than 20 nm, i.e., superparamagnetic materials [3].

In this process, two stages are involved; when the reactants' concentration reaches the critical supersaturation state and the rapid nucleation occurs. The slow growth of the nuclei by diffusion of the solute substances to the surface occurs in the second stage of the crystal. Iron oxides (Fe_3O_4 or γ - Fe_2O_3) are a stoichiometric mixture of ferric and ferrous salts. The chemical reaction of the magnetite (Fe_3O_4) formation can be written as,

$Fe^{2+} + 2Fe^{3+} + 8OH^- \rightarrow Fe_3O_4 + 4H_2O$…..2.1

This reaction's thermodynamics will give complete precipitation of Fe_3O_4. It will occur in the pH range from 8 to 14, with a molar ratio of 1:2 (Fe^{2+}/Fe^{3+}) in an environment free of oxygen. However, magnetite (Fe_3O_4) is not very stable, and it can transform to maghemite (γ-Fe_2O_3) in the presence of oxygen [4].

For magnetite synthesis, the ferric chloride (Fe^{2+}) and ferrous chloride (Fe^{3+}) were mixed in a 1:2 ratio in 100 mL of deionized water at room temperature. Ammonium hydroxide solution was added, dropwise, to that mixture under continuous stirring and constant nitrogen flow until black precipitates were formed. The black precipitate was then recovered and washed several times with deionized water. The final precipitate and the suspended particles were collected with a strong magnet, and the material was dried in an oven at 70˚C overnight. Then, the obtained black crystals were powdered using a pestle and mortar [5]. Since Fe_3O_4 (magnetite) easily oxidizes and is not stable, γ-Fe_2O_3 (maghemite), the stable phase, was used for adsorption experiments. The synthesis

procedure was similar to that of magnetite. After the synthesis, the magnetite was calcined at 150°C for 2 hours to obtain the maghemite phase [6]. The synthesis protocol is shown in figure 2.1.

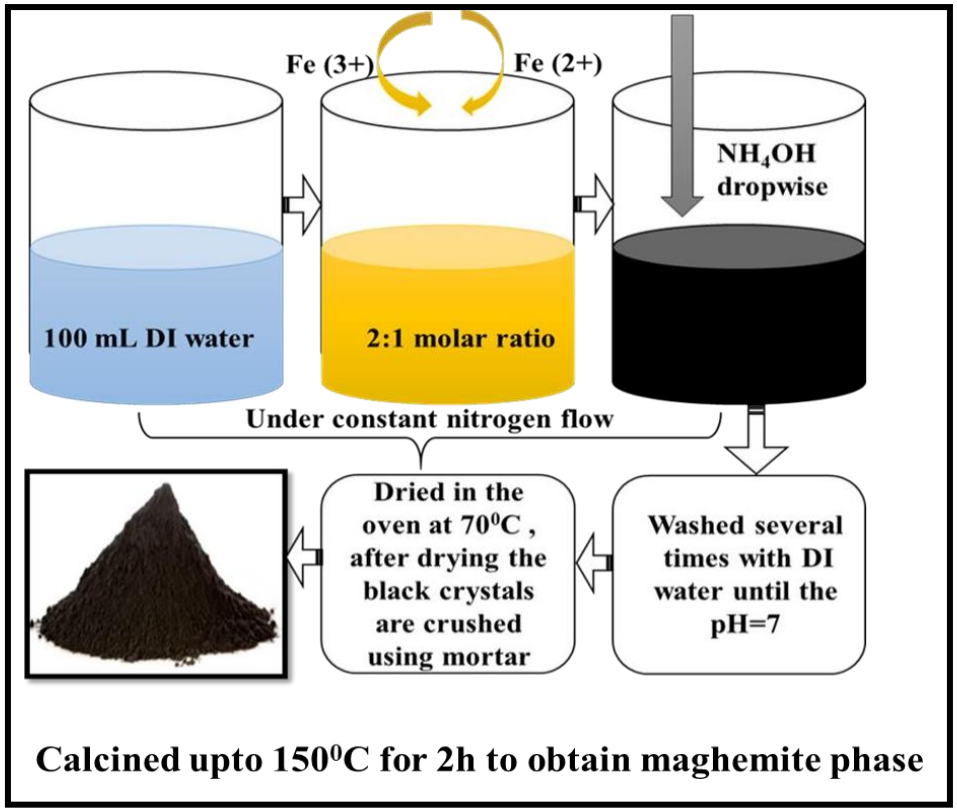

Figure 2.1 Synthesis of magnetite using co-precipitation method

2.1.3 TiO_2 Anatase synthesis using sol-gel method

The sol-gel technique involves the conversion of small molecules (precursors) into a colloidal solution (sol) and then into an integrated network (gel). This process involves four stages: hydrolysis, condensation/polymerization of monomers, growth of particles, and gel formation. The advantages of the sol-gel technique are [7] [8] [9] [10] [8],

- It is a low-cost and simple process compared to other techniques
- It allows the addition of transition metals or doping process

- It will give nanoparticles with high purity and homogeneity
- It will give uniform and small-sized powders at lower temperatures
- It has now become a widespread technique in scientific research with general acceptance

Some traditional precursors of the sol-gel method are tetramethyl orthosilicate (TMOS) and alkoxysilanes, such as tetraethyl orthosilicate (TEOS); efforts are made to find less toxic and more environmentally friendly precursors. In this study, the nano-sized TiO_2 anatase powders were synthesized using $TiCl_4$ as a precursor due to the low cost and easier control of hydrolysis. The results confirmed an excellent way to prepare nano-sized anatase TiO_2 powder using $TiCl_4$ as a precursor [11].

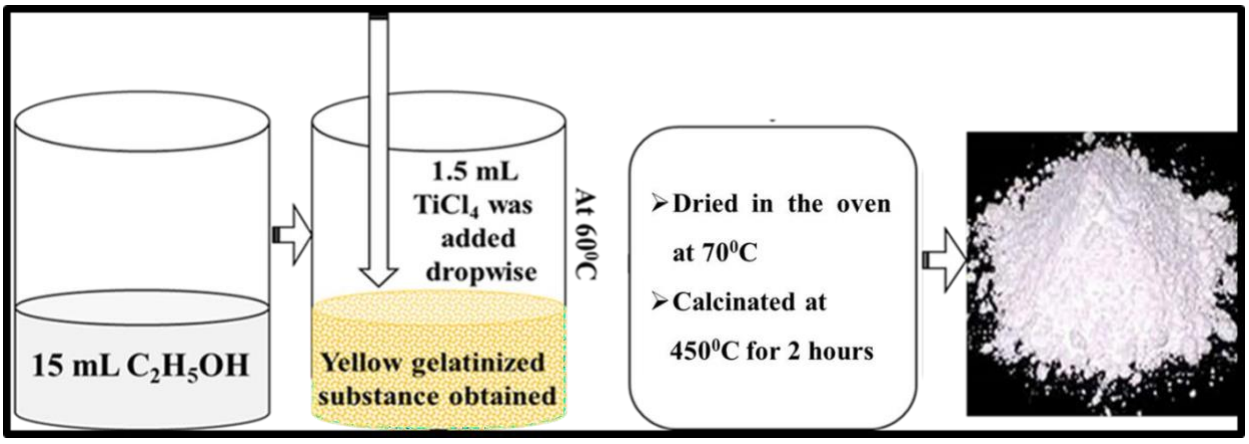

Figure 2.2 Synthesis of TiO_2 Anatase using sol-gel method

The synthesis protocol for TiO_2 anatase using the sol-gel method is shown in figure 2.2. It was obtained by adding 5 mL of $TiCl_4$ dropwise into 15 mL of ethanol at 60°C under continuous stirring. A large amount of HCl gas released during the mixing process was safely extracted using the laboratory fume exhaust. After 30 minutes, a light-yellow gel was obtained, kept in the oven at 70°C for 24h. The dry-gel precursor was calcined at 450°C in the furnace and grounded to obtain the TiO_2 powder [12].

2.1.4 Synthesis of TiO_2/Fe_3O_4 nanocomposite using ultrasonication method

A simple ultrasonication technique was tried to synthesize the TiO_2/Fe_3O_4 nanocomposite because of its simplicity and high dispersion of the obtained nanoparticles. The $(TiO_2)_x(Fe_3O_4)_{1-x}$ (x = 0.2, 0.5, and 0.8) NCs were prepared by the following method as shown in figure 2.3. Solution A consisted of TiO_2 in 20 mL of ethanol, while Solution B consisted of Fe_3O_4 in 5 mL of deionized water. Both solutions were individually ultrasonicated for 30 min to get a uniform dispersion. Subsequently, solution B (magnetite) was slowly added to solution A (TiO_2) under ultrasonication for 60 minutes until the formation of a uniform dispersion. The final precipitate was washed several times with deionized water and dried in an oven at 70°C overnight to get the TiO_2/Fe_3O_4 nanocomposite powder.

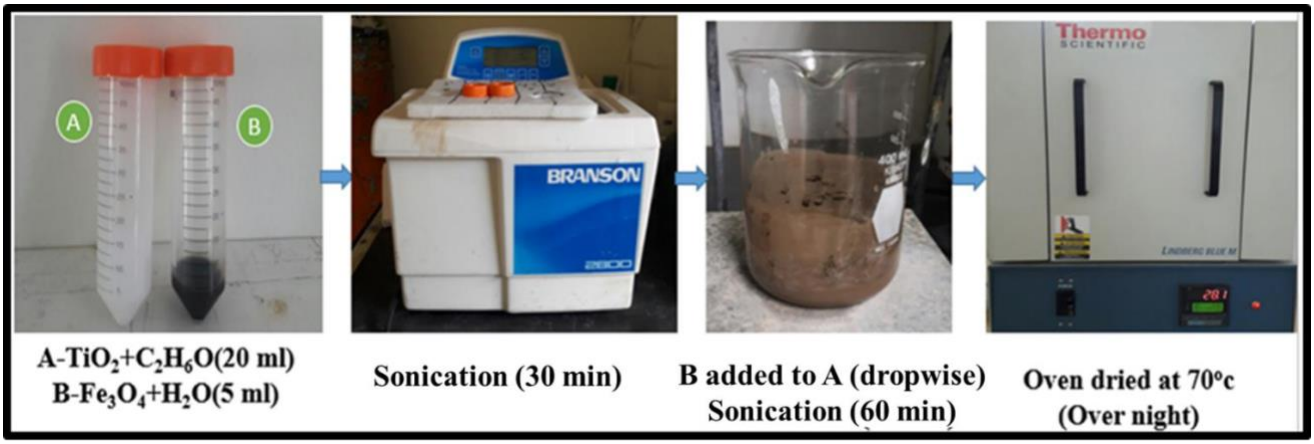

Figure 2.3 Synthesis of the nanocomposite material of $(TiO_2)_x(Fe_3O_4)_{1-x}$ (x = 0.2, 0.5 and 0.8) using ultrasonication method

(Thermo Scientific, Lindberg/Blue M VO914, BRANSON ultrasonicator) LENE, CINVESTAV

2.1.5 Synthesis of TiO_2/Fe_2O_3 nanocomposite using ball milling method

The ball milling method provides an effective mechanical milling process with several advantages over other synthesis methods preparing NCs, especially the cost-to-efficiency ratios.

This process does not require any solvents. Other advantages include the relatively low installation cost, low power and grinding medium, suitability for batch and continuous operation, and capability to treat materials displaying different hardness [13] [14]. The ball-milling process has also gained high importance over other synthesis methods because of its greener and facile technique. Hence, it eliminates waste generation from multi-step procedures, high temperature, and pressure conditions and requires no hazardous and expensive chemicals. Also, it yields a more considerable amount of the target product with short processing time at ambient conditions and is better suitable for large-scale industrial production [15] [16] [17] [18]. During milling, the balls constriction provides the required friction to produce fine nanomaterials, and the generated heat contributes effectively to the reaction, essentially resulting in a reactive milling process. The process effectiveness depends on several factors, including the ball to powder ratio (BPR) and milling time, which determines the properties of the synthesized nanostructures [19] [20] [21] [22].

In this work, the titania/maghemite (T/M) NCs were synthesized by varying the BPR (10:1, 20:1, and 30:1) using different milling times (2 and 6 h) by mixing appropriate quantities of TiO_2 and γ-Fe_2O_3. The synthesis was performed using a planetary ball mill at 300. rpm After optimizing the BPR and milling time, the 5 ratios (1/9, 3/7, 5/5, 7/3, and 9/1) of the T/M NCs were synthesized using 10:1 BPR and 2 hour milling time by mixing appropriate quantities of TiO_2 and γ-Fe_2O_3 and processed using ball milling. Figure 2.4 shows the planetary ball mill used and T/M nanocomposite synthesis using the ball milling by varying BPR and milling time.

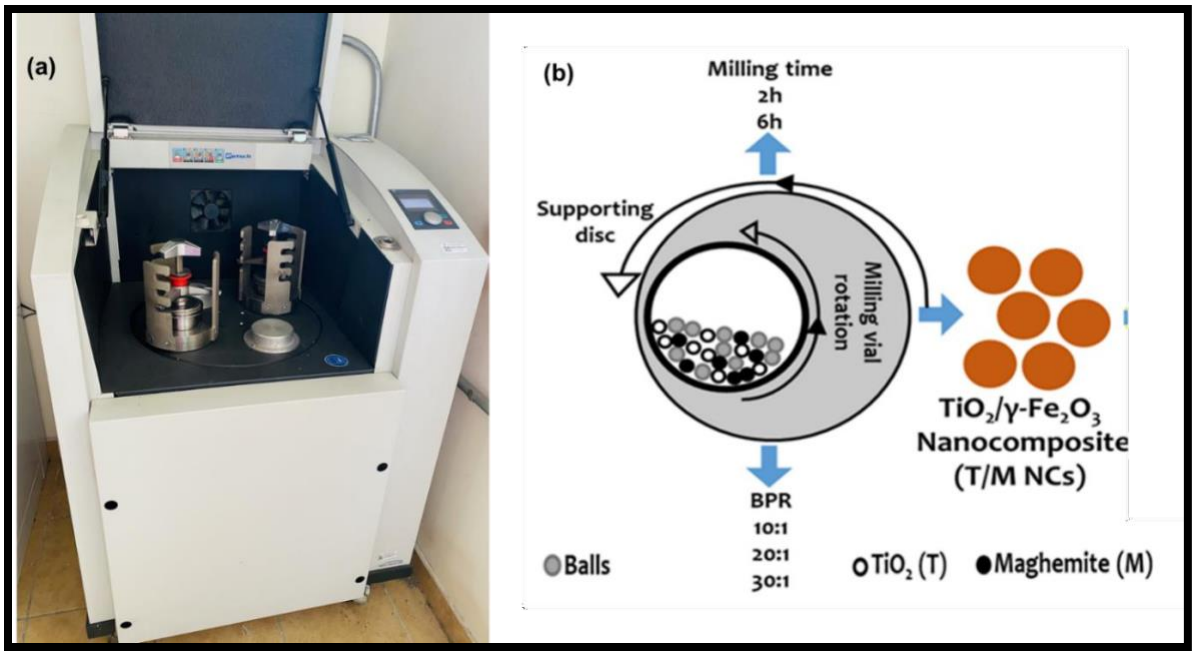

Figure 2.4 Synthesis of the T/M nanocomposite using ball milling method

(LENE, CINVESTAV, Mexico City)

2.1.6 Photocatalytic studies

The photocatalysis experiments of TiO_2, Fe_3O_4, and the $(TiO_2)_x(Fe_3O_4)_{1-x}$ (x = 0.2, 0.5, and 0.8) NC synthesized by sonication method were carried out using a solar simulator equipped with a 1.6 kW xenon arc lamp. The catalyst (1g/L) was added to the Orange G (50 mg/L) solution and mechanically stirred in the dark for 20 min to ensure the adsorption/desorption equilibrium. Subsequently, the suspension was irradiated by visible light using a solar simulator at various periods (0 to 120 min). After the experiment, 4 ml of aliquot sample were taken and filtered. The filtered sample is used to determine the final concentration of Orange G after degradation. It was determined by measuring the value at 476 nm in the spectrophotometer [23]. After the experiment, the powders were collected with a strong magnet, washed several times with deionized water, and dried in an oven at 70°C for further use.

2.1.7 Spectrophotometric determination of As (III) and As (V) in water samples

- The standard solutions of 100 mL of 1000 ppm of As (III) and As (V) were prepared by dissolving 0.1302g of As_2O_3, 1g of NaOH, and 20 mL of concentered HCl in deionized water, and 0.4245g of $HAsNa_2O_4.7H_2O$ in deionized water, respectively.
- Ammonium molybdate tetrahydrate solution was prepared by mixing 6.5g of $H_{24}MoO_7N_8O_{24}.4H_2O$ in 50 mL deionized water (part 1). Potassium antimonyl tartrate trihydrate solution was prepared by mixing 0.175g $C_8H_4K_2O_{12}Sb_2.3H_2O$ in 50 mL of deionized water (part 2).
- Solution A was prepared by mixing 5 mL of part 1 solution and 5 mL of part 2 solution, and 15 mL of 9M H_2SO_4.
- Solution B was prepared by dissolving 1g of ascorbic acid in 10 mL of deionized water and 0.1 M of the $KMnO_4$ solution.
- 0.1M NaOH and acetic acid solutions were used to adjust the pH to 7.
- For the determination of As (III), 200 µl of solution A, 100 µl of Solution B, and 700 µl of H_2O were added to 4 ml of the sample.
- For the As (V) determination, 100 µl of the $KMnO_4$ solution was added to the 4 mL sample; then, after 5 min, 200 µl of solution A, 100 µl of Solution B, and 600 µl of H_2O were added to 4 ml of the sample.

2.1.8 Adsorption studies

The Batch adsorption experiments of TiO_2, γ-Fe_2O_3, and the TiO_2/γ-Fe_2O_3 (T/M) NC to remove arsenic were carried out using a shaking incubator (Labnet). A constant 300 RPM and the room temperature were maintained in the shaking incubator for all the studies. Initially, 2ppm As (III) and As (V) solutions were prepared by diluting the arsenic stock solution. To the As (III) and As (V) solutions, the adsorbents were added and kept in the shaking incubator for the required time period. After the experiment, the samples were collected and filtered. The required reagents were added for the spectrophotometric measurement, as mentioned in the previous section (2.1.7). The reaction time will take minimum 2 hours, the sample has to be kept in the dark for 2 hours, and absorbance was measured at 870 nm in the spectrophotometer. A detailed description of the adsorbents used and adsorption conditions are presented in table 2.1.

Table 2.1 Experimental conditions for arsenic adsorption studies

<table>
<tr><th>Milling Time</th><th>BPR</th><th>Experimental Conditions</th><th>Description</th></tr>
<tr><td>2h</td><td>10:1
20:1
30:1</td><td rowspan="2">Adsorbate concentration
As (III) - 2ppm
As (v) - 2ppm
pH - 7
adsorbent dosage - 0.5 g/L
Time - 5min</td><td rowspan="2">Studies for the optimization of BPR and milling time</td></tr>
<tr><td>6h</td><td>10:1
20:1
30:1</td></tr>
<tr><th colspan="2">10 : 1 BPR 2h milling time for T/M NC</th><th>Experimental Conditions</th><th>Description</th></tr>
<tr><td>TiO_2 Anatase</td><td>Maghemite</td><td>Adsorbate concentration
As (III) - 2ppm
As (v) - 2ppm
pH - 7</td><td>Studies on the optimization of the best ratio</td></tr>
</table>

10 30 50 70 90	90 70 50 30 10	adsorbent dosage - 0.5 g/L Time - 5min	
S.no	**Adsorption Parameters**	**Experimental Conditions**	**Description**
1	Effect of Dosage	Dose = 0.5, 2,4,6 and 8g/L pH - 7 Time - 5min As (III) and (v) - 2ppm	Studies on the optimization of complete removal of arsenic using the best ratio
2	Effect of Time	Time = 5,15,30,60min pH=7 Dose - 8g/L As (III) and (v) - 2ppm	
3	Effect of concentration	Concentration = 2,4 and 6 ppm Dose = 8 g/L , pH=7 Time = 15min	
4	Effect of pH	pH = 4,7 and 10 Time = 15min Dose = 8 g/L As (III) and (v) - 2ppm	
5	Reusability test for 5 times using optimized parameters	As (III) and (v) - 2ppm Dose - 8 g/L pH = 4 Time = 15min	

2. 2 Characterization of the nanomaterials

2.2.1 X-Ray Diffraction (XRD)

XRD is a characterization technique that is used to determine the structure and composition of crystalline structures. It is used to determine the crystallite size, d-spacing, lattice parameters, crystal structure, strain, and dislocation density. The powder samples used in the experiments were analyzed using a Bruker D2-phaser X-ray diffractometer ($Cu_{K\alpha}$ λ=1.5406Å) in the range from 10°-80° which is shown in figure 2.5.

The crystallite size (D_p) was calculated using the Scherrer equation [24],

$$D_p = \frac{K\lambda}{\beta \cos\theta} \quad \text{.....2.2}$$

Where K is the shape factor (0.94, assuming spherical crystallites), β is the full width at half maximum (FWHM), while θ is Bragg's diffraction angle. The interplanar distance (*d*) was measured using equation 2.3,

$$d = \frac{n\lambda}{2\sin\theta} \quad \text{.....2.3}$$

which allows for calculating the lattice parameters (a, c) for tetragonal structure using the relation presented below

$$\frac{1}{d^2} = \frac{h^2+k^2}{a^2} + \frac{l^2}{c^2} \quad \text{.....2.4}$$

while for cubic structures, the relation used is represented in equation 2.5,

$$\frac{1}{d^2} = \frac{h^2+k^2+l^2}{a^2} \quad \text{.....2.5}$$

where *hkl* is the miller indices from the X-ray diffractogram. The dislocation density, δ, measuring the number of dislocation lines in a unit area, is calculated using the relation [25],

$$\delta = \frac{1}{D_p^2} \quad \text{.....2.6}$$

and the microstrain was calculated by using equation 2.7 [26],

$$\varepsilon = \frac{\beta}{4\tan\theta} \quad \text{.....2.7}$$

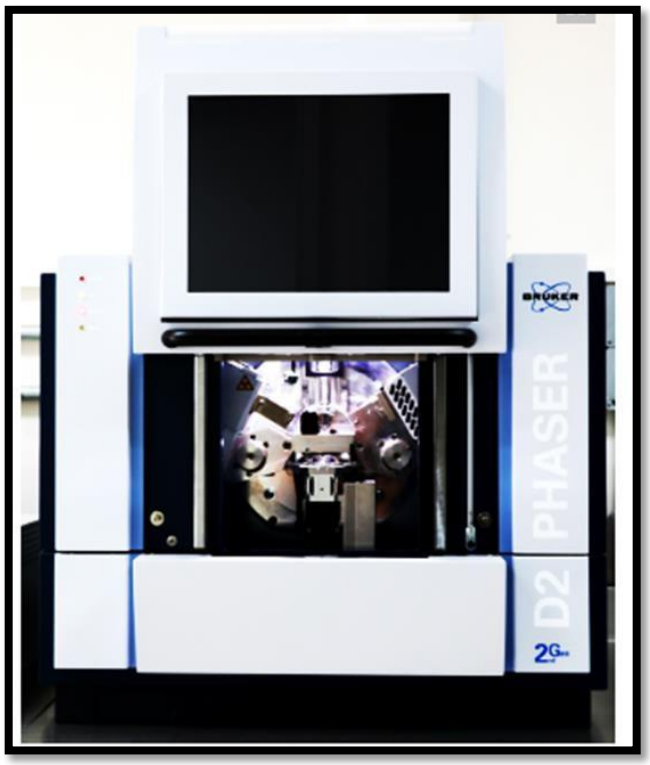

Figure 2.5 Bruker D2-phaser X-ray diffractometer

(LENE, CINVESTAV-IPN, Mexico City)

2.2.2 Field Emission Scanning Electron Microscopy (FESEM)

Figure 2.6 Tescan-Vega 3 SEM, equipped with STEM and Bruker EDX detectors

(LENE, CINVESTAV-IPN, Mexico City)

This technique analyses the morphology and chemical composition of the sample using a high-energy beam of electrons. The electrons interact with the sample, giving rise to signals on the sample's topographical information, elemental composition, and homogeneity [27]. The elemental composition and morphological analyses of the samples were determined using a Tescan-Vega 3 SEM, at an accelerating 10 kV, equipped with STEM and Bruker EDX detectors shown in figure 2.6. A dispersion of the powder material was prepared in an aqueous sodium dodecyl sulfate (10 g/L) solution, and a drop was deposited on an amorphous carbon-coated copper grid. The dried sample was analyzed with the STEM at an accelerating voltage of 30 kV.

2.2.3 High-resolution transmission electron microscopy (HR-TEM)

Figure 2.7 HRTEM (JEM – 2010, JEOL)

(FISICA, CINVESTAV-IPN, México city)

It is a powerful technique to probe the matter at its atomic level and nanoscale resolution. This technique associates electron diffraction tools to probe the crystallinity, determining the d-spacing, the Miller indices, the morphology, and the crystal orientation [28]. The high-resolution transmission electron microscopy (HRTEM) was performed at 200 keV, using JEM – 2010, JEOL Inc shown in figure 2.7.

2.2.4 Raman spectroscopy

Raman spectroscopy is a non-destructive technique used to study the samples' vibrational, rotational, and other low-frequency modes [29]. It is used as a support of XRD to determine the composition and crystalline phase of the materials. The NT-MDT INTEGRA system shown in figure 2.8 helped identify the phases and vibrational modes of the synthesized materials.

Figure 2.8 NT-MDT INTEGRA Raman equipment

(SEES, CINVESTAV-IPN, Mexico City)

2.2.5 X-ray photoelectron spectroscopy (XPS)

It is also a non-destructive spectroscopic technique for studying the chemical composition of the surface of solids. An energy analyzer measures the photoelectrons' kinetic energies and determines the materials' elemental composition [30] [31]. The binding energy is indicative of a specific element and a particular structural feature of electron distribution. XPS microprobe PHI 5000 Versa Probe II (Al X-ray source: 1486.6 eV) was used to characterize the materials.

2.2.6 UV-Visible Diffuse Reflectance Spectra

The reflectance measurements were performed in the wavelength range of 200-800 nm, using a JascoV-670 spectrophotometer coupled to an integrating sphere shown in figure 2.9, which is used to estimate the bandgap energy of the samples. The bandgap of the materials was calculated using Kubelka–Munk function, which is given by equation 2.8 [32] [33],

$$F(R) = \frac{(1-R)^2}{2R} \quad 2.8$$

Where R is the reflectance, F(R) is proportional to the extinction coefficient (α). This equation applies to highly light scattering materials and absorbing particles.

The bandgap of the materials was obtained by plotting the modified Kubelka-Munk function, $(F(R)*h\upsilon)^{n}$, vs. hυ and extrapolating the linear part of the graphics to the abscissa, where n = 1/2 for the direct transition, and n = 2 for an indirect transition [34]. For the experiments, the indirect transition values are used. The hυ is the energy in terms of eV and was obtained from equation 2.9,

$$E_g = h\upsilon = \frac{hc}{\lambda} = \frac{1243}{\lambda} \quad 2.9$$

Where h and c are constants, and λ is the wavelength followed.

Figure 2.9 JascoV-670 spectrophotometer coupled with the integrating sphere

(LENE, CINVESTAV-IPN, México City)

2.3 References

[1] F. Dong, W. Guo, and C.-S. Ha, "Monodisperse single-crystal mesoporous magnetite nanoparticles induced by nanoscale gas bubbles," *J. Nanoparticle Res.*, vol. 14, no. 12, p. 1303, Dec. 2012, doi: 10.1007/s11051-012-1303-9.

[2] S. Lin, J. Jin, S. Sun, and J. Yu, "Removal of arsenic contaminants using a novel porous nanoadsorbent with superior magnetic recovery," *Chem. Eng. Sci. X*, vol. 8, p. 100069, Nov. 2020, doi: 10.1016/j.cesx.2020.100069.

[3] R. Nisticò, "A synthetic guide toward the tailored production of magnetic iron oxide nanoparticles," *Boletín la Soc. Española Cerámica y Vidr.*, pp. 1–12, Feb. 2020, doi: 10.1016/j.bsecv.2020.01.011.

[4] A. F. Al-Alawy, E. E. Al-Abodi, and R. M. Kadhim, "Synthesis and Characterization of Magnetic Iron Oxide Nanoparticles by Co-Precipitation Method at Different Conditions," *J. Eng.*, vol. 24, no. 10, p. 60, 2018, doi: 10.31026/j.eng.2018.10.05.

[5] F. Yazdani and M. Seddigh, "Magnetite nanoparticles synthesized by co-precipitation method: The effects of various iron anions on specifications," *Mater. Chem. Phys.*, vol. 184, pp. 318–323, Dec. 2016, doi: 10.1016/j.matchemphys.2016.09.058.

[6] M. B., R. Hernandez-Maya, M. Solís-López, C. Th-Th, and V. S., "Photocatalytic degradation of Orange G using TiO2/Fe3O4 nanocomposites," *J. Mater. Sci. Mater. Electron.*, vol. 29, no. 18, pp. 15436–15444, Sep. 2018, doi: 10.1007/s10854-018-9069-1.

[7] P. G. Jamkhande, N. W. Ghule, A. H. Bamer, and M. G. Kalaskar, "Metal nanoparticles synthesis: An overview on methods of preparation, advantages and disadvantages, and applications," *J. Drug Deliv. Sci. Technol.*, vol. 53, no. June, p. 101174, Oct. 2019, doi:

10.1016/j.jddst.2019.101174.

[8] S. Ashraf, A. Siddiqa, S. Shahida, and S. Qaisar, “Titanium-based nanocomposite materials for arsenic removal from water: A review,” *Heliyon*, vol. 5, no. 5, p. e01577, 2019, doi: 10.1016/j.heliyon.2019.e01577.

[9] S. M. Gupta and M. Tripathi, “A review of TiO2 nanoparticles,” *Chinese Sci. Bull.*, vol. 56, no. 16, pp. 1639–1657, 2011, doi: 10.1007/s11434-011-4476-1.

[10] M. Dahl, Y. Liu, and Y. Yin, “Composite titanium dioxide nanomaterials,” *Chem. Rev.*, vol. 114, no. 19, pp. 9853–9889, 2014, doi: 10.1021/cr400634p.

[11] Z. Xu, Q. Li, S. Gao, and J. K. Shang, “As(III) removal by hydrous titanium dioxide prepared from one-step hydrolysis of aqueous TiCl4 solution,” *Water Res.*, vol. 44, no. 19, pp. 5713–5721, 2010, doi: 10.1016/j.watres.2010.05.051.

[12] Y. Zhu, L. I. Zhang, C. Gao, and L. Cao, “The synthesis of nanosized TiO2 powder using a sol-gel method with TiCl4 as a precursor,” *J. Mater. Sci.*, vol. 35, no. 16, pp. 4049–4054, Aug. 2000, doi: 10.1023/A:1004882120249.

[13] M. Cantarella *et al.*, “Mechanical milling: a sustainable route to induce structural transformations in MoS2 for applications in the treatment of contaminated water,” *Sci. Rep.*, vol. 9, no. 1, p. 974, Dec. 2019, doi: 10.1038/s41598-018-37798-8.

[14] T. T. Bui, X. Q. Le, D. P. To, and V. T. Nguyen, “Investigation of typical properties of nanocrystalline iron powders prepared by ball milling techniques,” *Adv. Nat. Sci. Nanosci. Nanotechnol.*, vol. 4, no. 4, p. 045003, Aug. 2013, doi: 10.1088/2043-6262/4/4/045003.

[15] J. A. Castrillón Arango, A. A. Cristóbal, C. P. Ramos, P. G. Bercoff, and P. M. Botta,

"Mechanochemical synthesis and characterization of nanocrystalline Ni1-xCoxFe2O4 ($0 \leq x \leq 1$) ferrites," *J. Alloys Compd.*, vol. 811, p. 152044, Nov. 2019, doi: 10.1016/j.jallcom.2019.152044.

[16] J. Hu, X. Geng, Y. Duan, W. Zhao, M. Zhu, and S. Ren, "Effect of Mechanical–Chemical Modification Process on Mercury Removal of Bromine Modified Fly Ash," *Energy & Fuels*, vol. 34, no. 8, pp. 9829–9839, Aug. 2020, doi: 10.1021/acs.energyfuels.0c01509.

[17] H. Li, Y. Chen, Y. Cao, G. Liu, and B. Li, "Comparative study on the characteristics of ball-milled coal fly ash," *J. Therm. Anal. Calorim.*, vol. 124, no. 2, pp. 839–846, 2016, doi: 10.1007/s10973-015-5160-5.

[18] C. Suryanarayana, "Mechanical alloying and milling," *Prog. Mater. Sci.*, vol. 46, no. 1–2, pp. 1–184, 2001, doi: 10.1016/S0079-6425(99)00010-9.

[19] J. Jiang and J. Li, "Mechanically Induced N -arylation of Amines with Diaryliodonium Salts," *ChemistrySelect*, vol. 5, no. 2, pp. 542–548, Jan. 2020, doi: 10.1002/slct.201904188.

[20] J.-L. Do and T. Friščić, "Mechanochemistry: A Force of Synthesis," *ACS Cent. Sci.*, vol. 3, no. 1, pp. 13–19, Jan. 2017, doi: 10.1021/acscentsci.6b00277.

[21] H. Shin, S. Lee, H. Suk Jung, and J. B. Kim, "Effect of ball size and powder loading on the milling efficiency of a laboratory-scale wet ball mill," *Ceram. Int.*, vol. 39, no. 8, pp. 8963–8968, 2013, doi: 10.1016/j.ceramint.2013.04.093.

[22] M. J. Yu, X. L. Cai, L. Zhou, C. Hu, Z. Li, and F. Yi, "Effect of Balls/Powder Weight Ratio in Milling on Microstructure and Properties of MWCNTs/Cu Composites," *Key Eng. Mater.*, vol. 609–610, pp. 394–399, Apr. 2014, doi: 10.4028/www.scientific.net/KEM.609-

610.394.

[23] I. Singhvi and S. Pillai, “Application of orange G dye for quantitation of citalopram hydrobromide, donepezil hydrochloride and rabeprazole sodium from tablet formulation,” *Indian J. Pharm. Sci.*, vol. 68, no. 5, p. 682, Feb. 2006, doi: 10.4103/0250-474X.29652.

[24] A. Valério and S. L. Morelhão, “Usage of Scherrer’s formula in X-ray diffraction analysis of size distribution in systems of monocrystalline nanoparticles.”

[25] M. Ohring, “MECHANICAL BEHAVIOR OF SOLIDS,” in *Engineering Materials Science*, Elsevier, 1995, pp. 299–V.

[26] A. Morán, O. Nwakanma, S. Velumani, and H. Castaneda, “Comparative study of optimised molybdenum back-contact deposition with different barriers (Ti, ZnO) on stainless steel substrate for flexible solar cell application,” *J. Mater. Sci. Mater. Electron.*, vol. 31, no. 10, pp. 7524–7538, May 2020, doi: 10.1007/s10854-020-03058-7.

[27] A. D. Weiss, “Scaning electron microscopes,” *Met. Finish.*, vol. 101, no. 12, p. 63, Dec. 2003, doi: 10.1016/S0026-0576(03)90123-1.

[28] M. Rezaee, S. M. Mousavi Khoie, and K. H. Liu, “The role of brookite in mechanical activation of anatase-to-rutile transformation of nanocrystalline TiO2: An XRD and Raman spectroscopy investigation,” *CrystEngComm*, vol. 13, no. 16, pp. 5055–5061, 2011, doi: 10.1039/c1ce05185g.

[29] G. Gouadec and P. Colomban, “Raman Spectroscopy of nanomaterials: How spectra relate to disorder, particle size and mechanical properties,” *Prog. Cryst. Growth Charact. Mater.*, vol. 53, no. 1, pp. 1–56, 2007, doi: 10.1016/j.pcrysgrow.2007.01.001.

[30] P. Parthasarathy and S. K. Narayanan, “Effect of Hydrothermal Carbonization Reaction Parameters on,” *Environ. Prog. Sustain. Energy*, vol. 33, no. 3, pp. 676–680, 2014, doi: 10.1002/ep.

[31] S. Wu *et al.*, “Enhanced adsorption of cadmium ions by 3D sulfonated reduced graphene oxide,” *Chem. Eng. J.*, vol. 262, pp. 1292–1302, 2015, doi: 10.1016/j.cej.2014.10.092.

[32] P. Makuła, M. Pacia, and W. Macyk, “How To Correctly Determine the Band Gap Energy of Modified Semiconductor Photocatalysts Based on UV-Vis Spectra,” *Journal of Physical Chemistry Letters*, vol. 9, no. 23. American Chemical Society, pp. 6814–6817, Dec. 06, 2018, doi: 10.1021/acs.jpclett.8b02892.

[33] J. Yan, Y. Zhang, S. Liu, G. Wu, L. Li, and N. Guan, “Facile synthesis of an iron doped rutile TiO 2 photocatalyst for enhanced visible-light-driven water oxidation,” *J. Mater. Chem. A*, vol. 3, no. 43, pp. 21434–21438, 2015, doi: 10.1039/C5TA07003A.

[34] A. Escobedo-Morales, I. I. Ruiz-López, M. deL. Ruiz-Peralta, L. Tepech-Carrillo, M. Sánchez-Cantú, and J. E. Moreno-Orea, “Automated method for the determination of the band gap energy of pure and mixed powder samples using diffuse reflectance spectroscopy,” *Heliyon*, vol. 5, no. 4, p. e01505, Apr. 2019, doi: 10.1016/j.heliyon.2019.e01505.

3. CHAPTER 3 - PHOTOCATALYTIC DEGRADATION OF ORANGE G USING TiO_2/Fe_3O_4 (T/M) NANOCOMPOSITES SYNTHESIZED BY ULTRASONICATION METHOD

3. Brief Description

Azo dyes are the most notorious widespread environmental pollutants associated with textile, cosmetic, food colorants, printing, and pharmaceutical industries [1] [2]. These compounds are electron deficient xenobiotic compounds as they have electron-withdrawing groups that generate electron deficiency in the molecule resulting in degradation resistance [3] [4]. It poses a significant threat to the ecosystem because of its non-degradability, toxicity, potential mutagenicity, and carcinogenicity [5] [6]. Hence, there is a considerable need to treat these azo dyes effluents with cost-effective processes. In this study, Orange G was selected as the model dye, which is also an azo dye. In this work, we have deliberated the synthesis of magnetite using the co-precipitation method and $(TiO_2)_x(Fe_3O_4)_{1-x}$ (x = 0.2, 0.5, and 0.8) nanocomposites by a modified ultrasonication method. When TiO_2/ Fe_3O_4 (T/M) NC is annealed at high temperature, the Fe_3O_4 phase changes to the antiferromagnetic α-Fe_2O_3 phase, whereas the anatase phase will changes to rutile phase [7] [8] [9]. Therefore, a low-temperature method was followed to maintain Fe_3O_4 and TiO_2 phases, which are easy to synthesize and yields good results, and there is no phase change of Fe_3O_4. There was a superior photocatalytic activity under visible light by modified magnetic nanoparticles with titanium dioxide. The used materials can be easily retrieved and reused after the photocatalytic

activity due to their strong magnetic properties [10] [11] [12]. The nanocomposites exhibited a superior photocatalytic activity under visible light, and the results are thus discussed in detail.

3.1 RESULTS AND DISCUSSIONS

3.1.1 XRD analysis

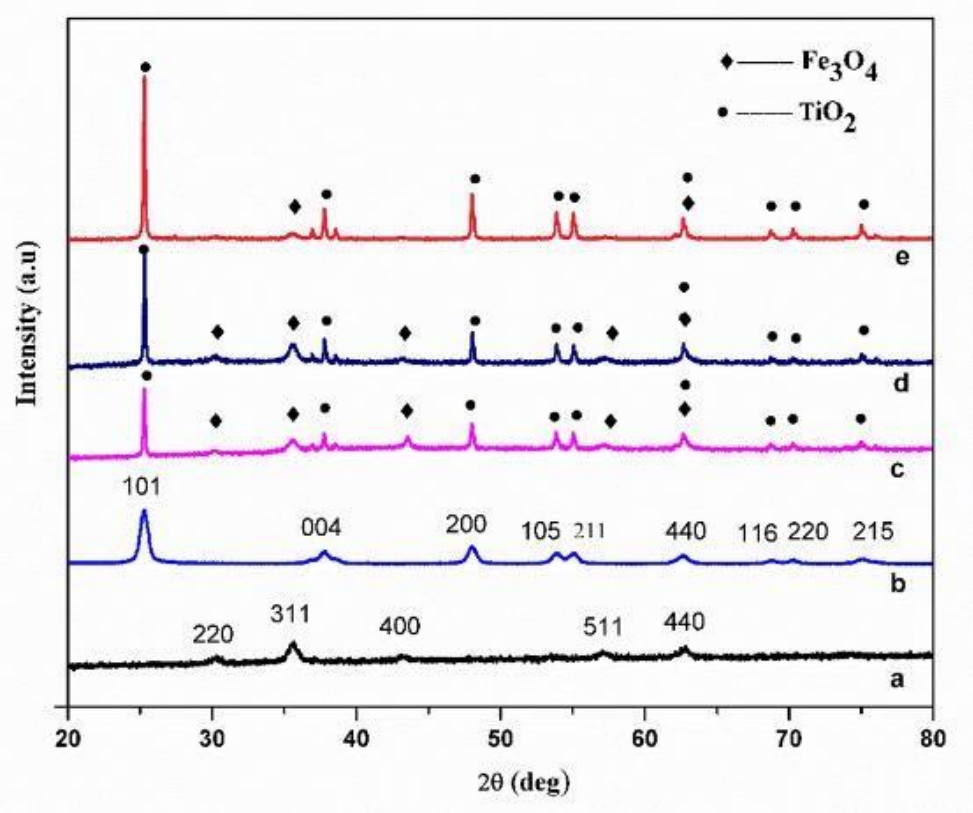

Figure 3.1 X-ray diffractograms of the synthesized materials: a) Fe_3O_4, b) TiO_2, c) T/M-0.2/0.8, d) T/M-0.5/0.5, and e) T/M-0.8/0.2.

The diffraction pattern of the synthesized magnetite shown in figure 3.1a showed peaks at 30.14°, 35.50°, 43.15°, 57.07°, and 62.67°, identified with the planes (220), (311), (400), (511), and (440), respectively, of the typical inverse cubic spinel structure of Fe_3O_4 (ICDD card no.71-6336). Figure 3.1b shows the diffraction pattern for TiO_2, where the position of the diffraction peaks at 25.28°, 37.80°, 48.04°, 53.88°, 55.06°, 62.68°, 68.76°, 70.30°, and 75.02°, corresponding

to planes (101), (004), (200), (105), (211), (204), (116), (220) and (215), respectively, of the tetragonal structure of TiO_2 (anatase ICDD card no. 21-1272). The results were well-matched with the previous reports [13] [14] [15] [16]. The sharp and intense peaks represented the high crystallinity of TiO_2 and Fe_3O_4. Figure 3.1 (c, d and e) represent the nanocomposite of TiO_2 / Fe_3O_4 with three different proportions 0.2/0.8, 0.5/0.5, and 0.8/0.2, respectively. The $(TiO_2)_{0.2}(Fe_3O_4)_{0.8}$ nanocomposite showed all the peaks of TiO_2 and Fe_3O_4. However, with the increase of TiO_2 content, the photocatalytic activity of the nanocomposite decreased [17] [18] [19] [20]. The crystallite size of the TiO_2 in the nanocomposites, for the weight ratios 0.8/0.2, 0.5/0.5, and 0.2/0.8, was estimated as 36.73, 31.82, and 29.50 nm, respectively. It was apparent that the crystallite size of TiO_2 decreases with the increase in Fe_3O_4 content, as shown in table 3.1

3.1.2 Morphological analysis

The scanning electron micrographs of the nanocomposites are shown in figure 3.2. The micrographs showed the broad distribution of the nanoparticles forming several clusters. The $(TiO_2)_{0.5}/(Fe_3O_4)_{0.5}$ nanocomposite showed a more homogeneous distribution [21] [22] [23]. We have also studied the synthesized magnetite crystals that were crushed using a pestle and mortar for comparison. The SEM images showed large pieces, chunks of several µm in dimensions, and finer particles and agglomerates of various sizes [24] [25]. Some of these chunks have also been noticed in the SEM images of the nanocomposite. It is likely that the drying process promoted agglomeration/aggregation of nanoparticles, especially with the magnetite nanoparticles due to dipole interactions [26] [9]. To determine and distinguish the nanoparticle distribution in the synthesized nanocomposites, we have carried out the STEM analysis on the best photocatalytic component $(TiO_2)_{0.2}/(Fe_3O_4)_{0.8}$ nanocomposites, using both bright and dark field imaging mode. As we can observe in the dark field image shown in figure 3.3, the denser Fe_3O_4 particles,

appearing darker, are surrounded by lighter TiO_2 nanoparticles [12]. The magnetite particles were of diverse sizes, ranging from a few hundred nanometers to several micrometers, and neighbored by nanoparticles of TiO_2 [27]. Finer nanocomposites that are specially composed of TiO_2 nanoparticles were significant for the higher photocatalytic activity, which is shown below. The STEM analysis confirmed the formation of the nanocomposites. The image analysis was performed using Gatan Inc., Digital Micrograph software [28].

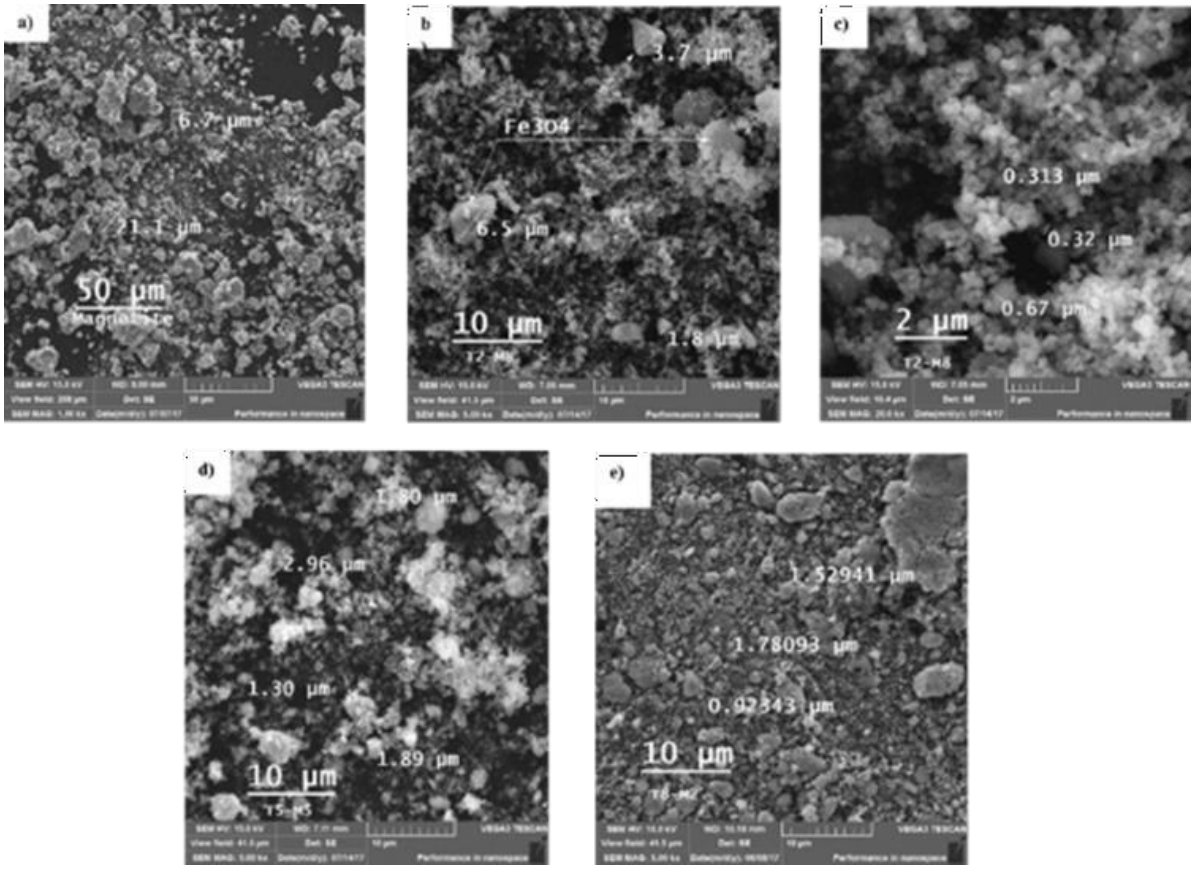

Figure 3.2 SEM images of a) crushed synthesized magnetite (Fe_3O_4) crystals, b) $(TiO_2)_{0.2}(Fe_3O_4)_{0.8}$ nanocomposites at 5 kx magnification, c) $(TiO_2)_{0.2}(Fe_3O_4)_{0.8}$ nanocomposites at 20 kx magnification, d) $(TiO_2)_{0.5}(Fe_3O_4)_{0.5}$, and e) $(TiO_2)_{0.8}(Fe_3O_4)_{0.2}$ at 5 kx magnification

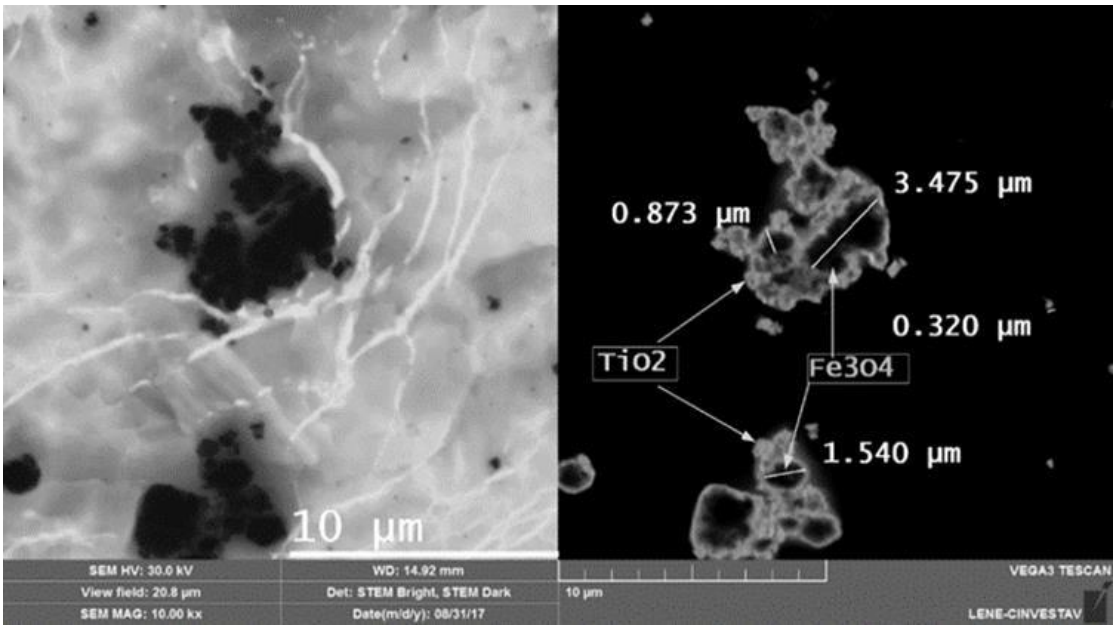

Figure 3.3 Image obtained by STEM of the nanocomposite material of $(TiO_2)_{0.2}$ $(Fe_3O_4)_{0.8}$

3.1.3 Raman analysis

According to the factor group analysis, TiO_2 has six modes of $A1_g+2B1_g+3E_g$ that are Raman active. In total, 15 normal modes of vibration were there for TiO_2. The Raman spectra of Fe_3O_4, TiO_2, and the nanocomposites are shown in figure 3.4. For the Raman spectrum of anatase, the Raman band frequencies were observed at 152, 206, 405, 523, and 647 cm^{-1}. The 152 cm^{-1} band was the strongest among all observed bands of anatase [29]. The three bands at 152, 206, and 647 cm^{-1} were assigned to the E_g modes, and the band at 405 cm^{-1} to the $B1_g$ mode, whereas the band 523 cm^{-1} was identified as the doublet of the $A1_g$ and $B1_g$ modes [30] [15]. Magnetite structure exhibits 14 Raman active modes ($3A_1+3E+8T_2$) and is detected by splitting E_g and T_{2g} modes. In the obtained spectrum, 226 cm^{-1} was assigned to the T_{2g} mode, and 306 cm^{-1} was assigned to the E_g mode [31] [32]. For magnetite, only two modes could be seen due to weak Raman scattering [33].

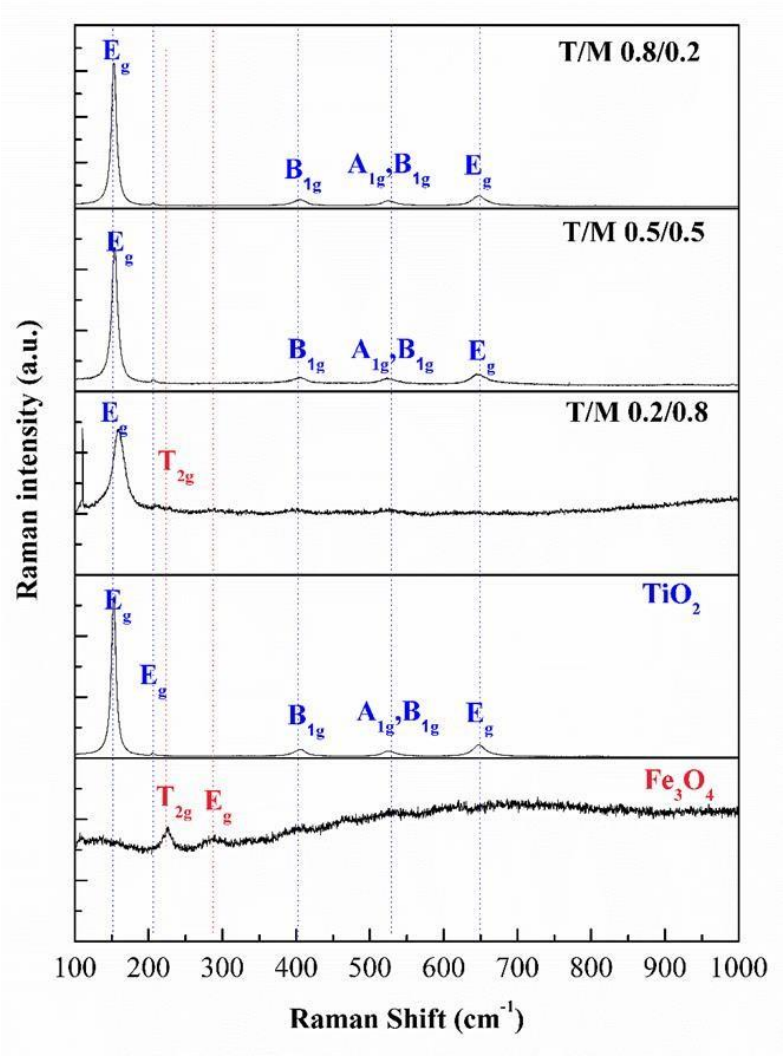

Figure 3.4 Raman analysis of Fe_3O_4, TiO_2, and $(TiO_2)_x$ $(Fe_3O_4)_{1-x}$ (x = 0.2, 0.5, and 0.8) (T/M) nanocomposites

3.1.4 UV- Visible diffuse reflectance spectrophotometric analysis

The optical studies of the synthesized nanocomposites were studied through UV-Visible DRS. By the calculated bandgap values, it was possible to understand the structural variation of the synthesized materials. The observed bandgap value of TiO_2 (anatase phase) is 3.2 eV, while for magnetite, 1.98 eV is observed, which is in agreement with the previously published results [34] [35].

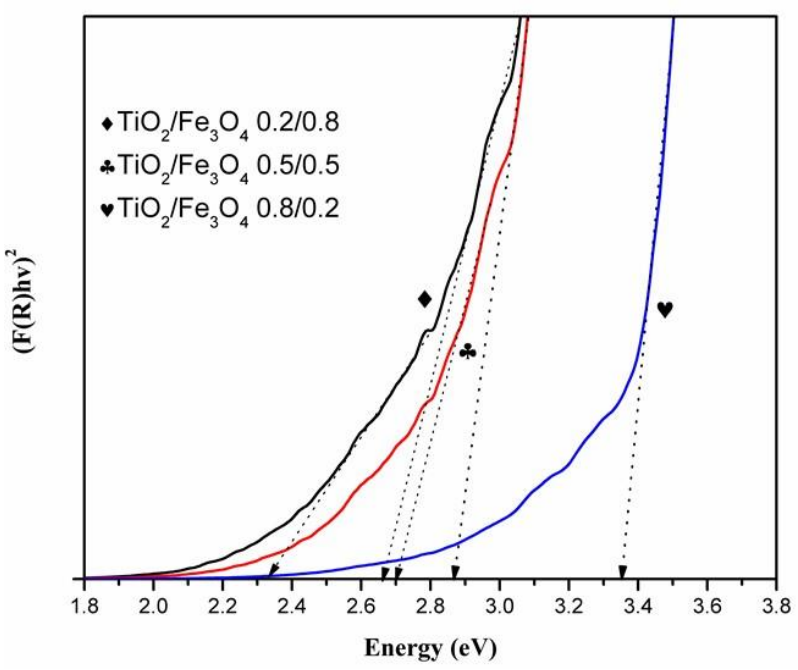

Figure 3.5 Diffuse reflectance spectra of $(TiO_2)_x (Fe_3O_4)_{1-x}$ (x = 0.2, 0.5 and 0.8) nanocomposites

Table 3.1The crystallographic direction, crystallite size and band gap of Fe_3O_4, TiO_2, and (TiO_2) x $(Fe_3O_4)_{1-x}$ (x = 0.2, 0.5 and 0.8) (T/M) nanocomposites

Materials	**Crystallite size (nm)**	**Bandgap (eV)**
TiO_2 (T)	17.62	3.2
Fe_3O_4 (M)	13	1.98
T/M 0.8/0.2	36.73	3.35
T/M 0.5/0.5	31.82	E_{g1}=2.70 E_{g2}=2.85
T/M 0.2/0.8	29.50	E_{g1}=2.35 E_{g2}=2.65

For the synthesized nanocomposite materials, the bandgap values were obtained by plotting $(F(R)*h\upsilon)^2$ vs. $h\upsilon$, considering an indirect transition (n=2) of the materials [36] [37]. The extrapolation of the $(TiO_2)_{0.8}/(Fe_3O_4)_{0.2}$ nanocomposite resulted in the bandgap of 3.35 eV. The other two nanocomposite ratios resulted in two different band gap values, which could be attributed to the spin-orbit splitting of the valence band [38] [22] [39], listed as Eg_1 and E_{g2} for lower and higher energies, respectively. The bandgap values of the synthesized nanocomposite materials, along with the precursors, are listed in table 3.1. It is observed that for all the nanocomposites with different ratios (0.2/0.8, 0.5/0.5, and 0.8/0.2), there is a shift in the bandgap values, shown in figure 3.5. The nanocomposite with high TiO_2 content, the obtained band gap values were almost close to the pure anatase. Reducing the TiO_2 content in the nanocomposite causes a shift towards the visible light range due increase in the magnetite content [40] [41]. Thus the bandgap of TiO_2/Fe_3O_4 shifts towards the visible region required for their efficient photocatalysis

3.2 Degradation of Orange G using TiO_2/Fe_3O_4 nanocomposites

The photocatalytic degradation studies for the Orange G were carried out using TiO_2, Fe_3O_4, and $(TiO_2)_x(Fe_3O_4)_{1-x}$ (x = 0.2, 0.5, and 0.8) nanocomposites, and it is shown in figure 3.6. For the experiments, a constant 50mg/L dye concentration, 1g/L dosage concentration, and pH=7 were maintained. The sample effect on orange G was observed. A detailed analytical description is mentioned in the experimental section (Chapter 2). The result shows that the $(TiO_2)_{0.2}(Fe_3O_4)_{0.8}$ nanocomposite showed the best photocatalytic property among all other materials. It is due to increasing the amount of Fe_3O_4 resulted in the reduction of the crystallite size and the bandgap energy of TiO_2 in the nanocomposite, leading to the increase in the photodegradation of Orange G. However, with the increase of TiO_2 content, the photocatalytic activity of the nanocomposite decreases [19]. As per the literature works, magnetite alone showed the photocatalytic activity in

the visible region, but magnetite nanoparticles' aggregation reduced the surface-active regions and prevented the light from passing through the material [42] [43]. Combining magnetite with TiO_2 reduces the recombination rate of titania and enhances photocatalytic activity [44]. The increase in the magnetite content increases the number of active sites on the nanocomposite surface and increases the generation of · OH radicals, and increases the dye removal. The same behavior was presented in literature which supports the argument [45] [46].

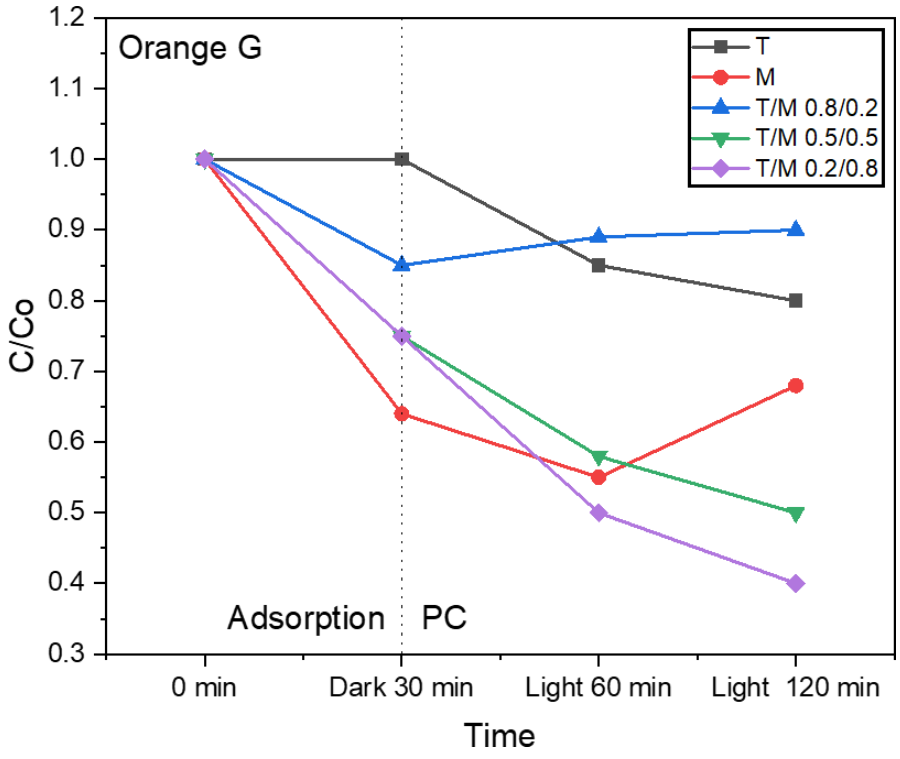

Figure 3.6 Photocatalytic degradation of Orange G using TiO_2, Fe_3O_4, and for the three TiO_2/Fe_3O_4 nanocomposite ratios

3.3. Photocatalytic mechanism

The degradation mechanism of the synthesized TiO_2/Fe_3O_4 involve:

$$TiO_2 + hu \rightarrow TiO_2\,(e^-_{CB} \ldots . h^+_{VB}) \quad \ldots\ldots 3.1$$

$TiO_2\,(e^-_{CB}) + Fe_3O_4 \rightarrow TiO_2 + Fe_3O_4\,(e^-_{CB})$ 3.2

$Fe_3O_4\,(e^-_{CB}) + O_2 \rightarrow TiO_2 + O^-_2$ 3.3

$O^-_2 + H_2O \rightarrow HO_2 + OH^-$ 3.4

$HO_2 + H_2O \rightarrow OH + H_2O_2$ 3.5

$H_2O_2 \rightarrow 2OH^-$ 3.6

$OH^- + Orange\ G \rightarrow H_2O + CO_2$ 3.7

$TiO_2(h^+_{VB}) + Orange\ G \rightarrow Degraded\ products$ 3.8

When a high energy photon is induced on a semiconductor photocatalyst, the electrons will be excited from the valence band (VB) to the conduction band (CB), leaving behind an electron vacancy or a hole in the valence band (equations. 3.1 and 3.2) [47] [48]. As a result, a reduction reaction between the electrons took place in the conduction band and electron acceptors, such as adsorbed O_2 molecules, which produce superoxide radical anions (equation. 3.3) [49]**.** The formed holes can either oxidize organic compounds directly or trap electron donors, and H_2O_2 is formed due to the recombination of these oxidant radicals (equations. 3.4 and 3.5) [50]. This H_2O_2 can react with the superoxide radical anion, thus regenerating hydroxyl radicals (equation 3.6). Both superoxide anion and hydroxyl radicals help in the decomposition of the toxic Orange G dye to non-toxic by-products (CO_2, H_2O, and mineral acids) on exposure to sunlight irradiation (equation. 3.7 and 3.8) [51] [20] [52] [53].

3.4 Conclusion

In this work, the Fe_3O_4 nanoparticles were synthesized by the co-precipitation method, and with the help of this, the $(TiO_2)_x\,(Fe_3O_4)_{1-x}$ (x = 0.2, 0.5 and 0.8) nanocomposites were synthesized.

The characterization results confirmed the successful synthesis of nanocomposites without any secondary phases. From XRD and UV-Vis analysis, it was inferred that the increasing amount of the magnetite decreased both the crystallite size and the bandgap value of TiO_2 in the nanocomposite.SEM analysis reveals the morphology of the synthesized materials aggregation that occurred in the magnetite particles. The addition of TiO_2 decreases the aggregation of magnetite, and the addition of magnetite to TiO_2 decreases its bandgap and increases its efficiency to the visible region. The $(TiO_2)_{0.2}(Fe_3O_4)_{0.8}$ nanocomposite shows good photocatalytic activity among other samples in the degradation of Orange G because of its small crystallite size, low bandgap value, and high surface area, which in turn increase the $OH^{\cdot}$ Radical generation. Even though degradation was achieved, it is less when compared to adsorption. When the same samples were tested for arsenic, it is not showing any photocatalytic activity. Hence not many studies were focused on the particular method apart from preliminary studies. Hence, another mechanical activation method was chosen, and its complete studies will be presented in chapters 4 and 5.

3.5 References

[1] J. Miao, R. Zhang, and L. Zhang, "Photocatalytic degradations of three dyes with different chemical structures using ball-milled TiO2," *Mater. Res. Bull.*, vol. 97, no. January 2017, pp. 109–114, 2018, doi: 10.1016/j.materresbull.2017.08.032.

[2] B. Lellis, C. Z. Fávaro-Polonio, J. A. Pamphile, and J. C. Polonio, "Effects of textile dyes on health and the environment and bioremediation potential of living organisms," *Biotechnol. Res. Innov.*, vol. 3, no. 2, pp. 275–290, Jul. 2019, doi: 10.1016/j.biori.2019.09.001.

[3] S. Sekar, M. Surianarayanan, V. Ranganathan, D. R. MacFarlane, and A. B. Mandal,

"Choline-based ionic liquids-enhanced biodegradation of azo dyes," *Environ. Sci. Technol.*, vol. 46, no. 9, pp. 4902–4908, 2012, doi: 10.1021/es204489h.

[4] Sumanjit, T. P. S. Walia, and R. Kaur, "Removal of health hazards causing acidic dyes from aqueous solutions by the process of adsorption," *Online J. Heal. Allied Sci.*, vol. 6, no. 3, 2007.

[5] B. Lellis, C. Z. Fávaro-Polonio, J. A. Pamphile, and J. C. Polonio, "Effects of textile dyes on health and the environment and bioremediation potential of living organisms," *Biotechnol. Res. Innov.*, vol. 3, no. 2, pp. 275–290, Jul. 2019, doi: 10.1016/j.biori.2019.09.001.

[6] T. A. Kurniawan, M. E. T. Sillanpää, and M. Sillanpää, "Nanoadsorbents for Remediation of Aquatic Environment: Local and Practical Solutions for Global Water Pollution Problems," *Crit. Rev. Environ. Sci. Technol.*, vol. 42, no. 12, pp. 1233–1295, Jun. 2012, doi: 10.1080/10643389.2011.556553.

[7] N. Chomchoey, D. Bhongsuwan, and T. Bhongsuwan, "Effect of calcination temperature on the magnetic characteristics of synthetic iron oxide magnetic nanoparticles for arsenic adsorption," *Chiang Mai J. Sci.*, vol. 45, no. 1, pp. 528–539, 2018.

[8] T. K. Ghorai, M. Chakraborty, and P. Pramanik, "Photocatalytic performance of nano-photocatalyst from TiO2 and Fe2O3 by mechanochemical synthesis," *J. Alloys Compd.*, vol. 509, no. 32, pp. 8158–8164, 2011, doi: 10.1016/j.jallcom.2011.05.069.

[9] J. Jia, J. C. Yu, X.-M. Zhu, K. M. Chan, and Y.-X. J. Wang, "Ultra-fast method to synthesize mesoporous magnetite nanoclusters as highly sensitive magnetic resonance probe," *J. Colloid Interface Sci.*, vol. 379, no. 1, pp. 1–7, Aug. 2012, doi: 10.1016/j.jcis.2012.04.035.

[10] Z. Li, L. Cheng, S. Zhang, Z. Wang, and C. Fu, “Enhanced photocatalytic and magnetic recovery performance of Co-doped BiFeO3 based on MOFs precursor,” *J. Solid State Chem.*, vol. 279, p. 120978, Nov. 2019, doi: 10.1016/j.jssc.2019.120978.

[11] Z.-J. Li *et al.*, “Enhanced Photocatalytic Removal of Uranium(VI) from Aqueous Solution by Magnetic TiO 2 /Fe 3 O 4 and Its Graphene Composite,” *Environ. Sci. Technol.*, vol. 51, no. 10, pp. 5666–5674, May 2017, doi: 10.1021/acs.est.6b05313.

[12] S. Mohammadi-Aghdam, B. Sarkhosh, and N. N. Tajoddin, “Recyclable Fe3O4/SiO2/TiO2/Cu nanocomposites: synthesis, characterization and investigation of the photocatalytic and magnetic property,” *J. Mater. Sci. Mater. Electron.*, vol. 28, no. 13, pp. 9456–9463, Jul. 2017, doi: 10.1007/s10854-017-6688-x.

[13] R. K. Wardani, K. Dahlan, S. T. Wahyudi, and S. G. Sukaryo, “Synthesis and characterization of nanoparticle magnetite for biomedical application,” 2019, vol. 2194, p. 020137, doi: 10.1063/1.5139869.

[14] S. Bagheri, K. Shameli, and S. B. Abd Hamid, “Synthesis and Characterization of Anatase Titanium Dioxide Nanoparticles Using Egg White Solution via Sol-Gel Method,” *J. Chem.*, vol. 2013, pp. 1–5, 2013, doi: 10.1155/2013/848205.

[15] M. C. Ceballos-Chuc, C. M. Ramos-Castillo, J. J. Alvarado-Gil, G. Oskam, and G. Rodríguez-Gattorno, “Influence of brookite impurities on the raman spectrum of TiO2 anatase nanocrystals,” *J. Phys. Chem. C*, vol. 122, no. 34, pp. 19921–19930, Aug. 2018, doi: 10.1021/acs.jpcc.8b04987.

[16] J. Zhu, S. Liu, J. Ge, X. Guo, X. Wang, and H. Wu, “Synthesis of Fe2O3-TiO2/fly-ash-cenosphere composite and its mechanism of photocatalytic oxidation under visible light,”

Res. Chem. Intermed., vol. 42, no. 4, pp. 3637–3654, 2016, doi: 10.1007/s11164-015-2236-6.

[17] A. Valério and S. L. Morelhão, "Usage of Scherrer's formula in X-ray diffraction analysis of size distribution in systems of monocrystalline nanoparticles."

[18] R. M. El-sherif, T. A. Lasheen, and E. A. Jebril, "Fabrication and characterization of CeO 2 -TiO 2 -Fe 2 O 3 magnetic nanoparticles for rapid removal of uranium ions from industrial waste solutions," *J. Mol. Liq.*, vol. 241, pp. 260–269, Sep. 2017, doi: 10.1016/j.molliq.2017.05.119.

[19] S. Zhu *et al.*, "Fe2O3/TiO2 photocatalyst of hierarchical structure for H2 production from water under visible light irradiation," *Microporous Mesoporous Mater.*, vol. 190, pp. 10–16, 2014, doi: 10.1016/j.micromeso.2014.01.018.

[20] A. M. Abdel-Wahab, A. S. Al-Shirbini, O. Mohamed, and O. Nasr, "Photocatalytic degradation of paracetamol over magnetic flower-like TiO2/Fe2O3 core-shell nanostructures," *J. Photochem. Photobiol. A Chem.*, vol. 347, pp. 186–198, 2017, doi: 10.1016/j.jphotochem.2017.07.030.

[21] K. K. Kefeni and B. B. Mamba, "Photocatalytic application of spinel ferrite nanoparticles and nanocomposites in wastewater treatment: Review," *Sustain. Mater. Technol.*, vol. 23, p. e00140, Apr. 2020, doi: 10.1016/j.susmat.2019.e00140.

[22] S. Salamat, H. Younesi, and N. Bahramifar, "Synthesis of magnetic core-shell Fe3O4@TiO2 nanoparticles from electric arc furnace dust for photocatalytic degradation of steel mill wastewater," *RSC Adv.*, vol. 7, no. 31, pp. 19391–19405, 2017, doi: 10.1039/c7ra01238a.

[23] H. Cui, Y. Liu, and W. Ren, “Structure switch between α-Fe2O3, γ-Fe2O3 and Fe3O4 during the large scale and low temperature sol–gel synthesis of nearly monodispersed iron oxide nanoparticles,” *Adv. Powder Technol.*, vol. 24, no. 1, pp. 93–97, Jan. 2013, doi: 10.1016/j.apt.2012.03.001.

[24] J. A. Gomes, M. S. Rahman, K. Das, S. Varma, and D. Cocke, “A Comparative Electrochemical Study on Arsenic Removal Using Iron, Aluminum, and Copper Electrodes,” *ECS Trans.*, vol. 25, no. 28, pp. 59–68, Dec. 2019, doi: 10.1149/1.3309678.

[25] H. Ijadpanah-Saravy, M. Safari, A. Khodadadi-Darban, and A. Rezaei, “Synthesis of Titanium Dioxide Nanoparticles for Photocatalytic Degradation of Cyanide in Wastewater,” *Anal. Lett.*, vol. 47, no. 10, pp. 1772–1782, 2014, doi: 10.1080/00032719.2014.880170.

[26] N. Ajinkya, X. Yu, P. Kaithal, H. Luo, P. Somani, and S. Ramakrishna, “Magnetic Iron Oxide Nanoparticle (IONP) Synthesis to Applications: Present and Future,” *Materials (Basel).*, vol. 13, no. 20, p. 4644, Oct. 2020, doi: 10.3390/ma13204644.

[27] M. M. Mohamed, W. A. Bayoumy, M. E. Goher, M. H. Abdo, and T. Y. Mansour El-Ashkar, “Optimization of α-Fe 2 O 3 @Fe 3 O 4 incorporated N-TiO 2 as super effective photocatalysts under visible light irradiation,” *Appl. Surf. Sci.*, vol. 412, pp. 668–682, Aug. 2017, doi: 10.1016/j.apsusc.2017.03.200.

[28] H. Gunda, S. K. Das, and K. Jasuja, “Simple, Green, and High-Yield Production of Boron-Based Nanostructures with Diverse Morphologies by Dissolution and Recrystallization of Layered Magnesium Diboride Crystals in Water,” *ChemPhysChem*, vol. 19, no. 7, pp. 880–891, 2018, doi: 10.1002/cphc.201701033.

[29] M. B., R. Hernandez-Maya, M. Solís-López, C. Th-Th, and V. S., “Photocatalytic

degradation of Orange G using TiO2/Fe3O4 nanocomposites," *J. Mater. Sci. Mater. Electron.*, vol. 29, no. 18, pp. 15436–15444, Sep. 2018, doi: 10.1007/s10854-018-9069-1.

[30] R. A. Solano, A. P. Herrera, D. Maestre, and A. Cremades, "Fe-TiO 2 Nanoparticles Synthesized by Green Chemistry for Potential Application in Waste Water Photocatalytic Treatment," *J. Nanotechnol.*, vol. 2019, pp. 1–11, Jan. 2019, doi: 10.1155/2019/4571848.

[31] P. Russo *et al.*, "Ultrafine Magnetite Nanopowder: Synthesis, Characterization, and Preliminary Use as Filler of Polymethylmethacrylate Nanocomposites," *J. Nanotechnol.*, vol. 2012, pp. 1–8, 2012, doi: 10.1155/2012/728326.

[32] G. Gouadec and P. Colomban, "Raman Spectroscopy of nanomaterials: How spectra relate to disorder, particle size and mechanical properties," *Prog. Cryst. Growth Charact. Mater.*, vol. 53, no. 1, pp. 1–56, 2007, doi: 10.1016/j.pcrysgrow.2007.01.001.

[33] P. P. Bergmann CP, "Raman Spectroscopy of Iron Oxide of Nanoparticles (Fe3O4)," *J. Mater. Sci. Eng.*, vol. 05, no. 01, p. 217, 2015, doi: 10.4172/2169-0022.1000217.

[34] L. Kernazhitsky *et al.*, "Laser-excited excitonic luminescence of nanocrystalline TiO2 powder," *Ukr. J. Phys.*, vol. 59, no. 3, pp. 246–253, 2014, doi: 10.15407/ujpe59.03.0246.

[35] R. Wang, X. Wang, X. Xi, R. Hu, and G. Jiang, "Preparation and Photocatalytic Activity of Magnetic Fe 3 O 4 /SiO 2 /TiO 2 Composites," *Adv. Mater. Sci. Eng.*, vol. 2012, pp. 1–8, 2012, doi: 10.1155/2012/409379.

[36] S. Valencia, J. M. Marín, and G. Restrepo, "Study of the bandgap of synthesized titanium dioxide nanoparticules using the sol-gel method and a hydrothermal treatment," *Open Mater. Sci. J.*, vol. 4, pp. 9–14, 2010, doi: 10.2174/1874088X01004020009.

[37] R. López and R. Gómez, “Band-gap energy estimation from diffuse reflectance measurements on sol–gel and commercial TiO2: a comparative study,” *J. Sol-Gel Sci. Technol.*, vol. 61, no. 1, pp. 1–7, Jan. 2012, doi: 10.1007/s10971-011-2582-9.

[38] Z. L. Bushell *et al.*, “Giant bowing of the band gap and spin-orbit splitting energy in GaP1−xBix dilute bismide alloys,” *Sci. Rep.*, vol. 9, no. 1, p. 6835, Dec. 2019, doi: 10.1038/s41598-019-43142-5.

[39] A. Del and I. Politécnico, “" Síntesis y caracterización de materiales nanoestructurados de BiVO 4 dopado con metales.”

[40] M. Stefan *et al.*, “Synthesis and characterization of Fe 3 O 4 –TiO 2 core-shell nanoparticles,” *J. Appl. Phys.*, vol. 116, no. 11, p. 114312, Sep. 2014, doi: 10.1063/1.4896070.

[41] S. Bagheri and N. M. Julkapli, “Magnetite hybrid photocatalysis: advance environmental remediation,” *Rev. Inorg. Chem.*, vol. 36, no. 3, pp. 135–151, Jan. 2016, doi: 10.1515/revic-2015-0014.

[42] P. J. Vikesland, R. L. Rebodos, J. Y. Bottero, J. Rose, and A. Masion, “Aggregation and sedimentation of magnetite nanoparticle clusters,” *Environ. Sci. Nano*, vol. 3, no. 3, pp. 567–577, Jun. 2016, doi: 10.1039/c5en00155b.

[43] J. Liu, C. Dai, and Y. Hu, “Aqueous aggregation behavior of citric acid coated magnetite nanoparticles: Effects of pH, cations, anions, and humic acid,” *Environ. Res.*, vol. 161, pp. 49–60, Feb. 2018, doi: 10.1016/j.envres.2017.10.045.

[44] J. Zhang and Y. Nosaka, “Mechanism of the OH radical generation in photocatalysis with

TiO 2 of different crystalline types," *J. Phys. Chem. C*, vol. 118, no. 20, pp. 10824–10832, 2014, doi: 10.1021/jp501214m.

[45] Y. Zhong *et al.*, "The constraints of transition metal substitutions (Ti, Cr, Mn, Co and Ni) in magnetite on its catalytic activity in heterogeneous Fenton and UV/Fenton reaction: From the perspective of hydroxyl radical generation," *Appl. Catal. B Environ.*, vol. 150–151, pp. 612–618, May 2014, doi: 10.1016/j.apcatb.2014.01.007.

[46] A. Lasia, *Electrochemical Impedance Spectroscopy and its Applications*, vol. 9781461489. New York, NY: Springer New York, 2014.

[47] S. J. A. Moniz, S. A. Shevlin, X. An, Z. X. Guo, and J. Tang, "Fe2O3-TiO2 nanocomposites for enhanced charge separation and photocatalytic activity," *Chem. - A Eur. J.*, vol. 20, no. 47, pp. 15571–15579, 2014, doi: 10.1002/chem.201403489.

[48] J. Zhang, P. Zhou, J. Liu, and J. Yu, "New understanding of the difference of photocatalytic activity among anatase, rutile and brookite TiO 2," *Phys. Chem. Chem. Phys.*, vol. 16, no. 38, pp. 20382–20386, Aug. 2014, doi: 10.1039/C4CP02201G.

[49] A. Ibhadon and P. Fitzpatrick, "Heterogeneous Photocatalysis: Recent Advances and Applications," *Catalysts*, vol. 3, no. 1, pp. 189–218, Mar. 2013, doi: 10.3390/catal3010189.

[50] M. M. Mohamed, W. A. Bayoumy, M. E. Goher, M. H. Abdo, and T. Y. Mansour El-Ashkar, "Optimization of α-Fe 2 O 3 @Fe 3 O 4 incorporated N-TiO 2 as super effective photocatalysts under visible light irradiation," *Appl. Surf. Sci.*, vol. 412, no. January, pp. 668–682, 2017, doi: 10.1016/j.apsusc.2017.03.200.

[51] A. T. Babu, M. Sebastian, O. Manaf, and R. Antony, "Heterostructured Nanocomposites of

Ag Doped Fe3O4 Embedded in ZnO for Antibacterial Applications and Catalytic Conversion of Hazardous Wastes," *J. Inorg. Organomet. Polym. Mater.*, vol. 30, no. 6, pp. 1944–1955, Jun. 2020, doi: 10.1007/s10904-019-01366-y.

[52] Y. Li, N. Zhang, J. Chen, R. Li, L. Li, and K. Li, "Fabrication of α-Fe2O3/TiO2 bi-functional composites with hierarchical and hollow structures and their application in water treatment," *J. Nanoparticle Res.*, vol. 18, no. 2, p. 36, Feb. 2016, doi: 10.1007/s11051-016-3336-y.

[53] D. Beydoun, R. Amal, G. K. C. Low, and S. McEvoy, "Novel Photocatalyst: Titania-Coated Magnetite. Activity and Photodissolution," *J. Phys. Chem. B*, vol. 104, no. 18, pp. 4387–4396, May 2000, doi: 10.1021/jp992088c.

4. CHAPTER 4 - BALL MILLING PARAMETRIC INFLUENCE ON TiO_2/γ-Fe_2O_3 NANOCOMPOSITE AND ARSENIC ADSORPTION

4. Brief Description

The ball milling method offers a comparative means of NCs synthesis. This would modulate the properties of nanostructured materials [1]. Constriction of the balls provides the necessary friction to produce fine nanomaterials, and the generated heat during the milling contributes effectively to reaction, essentially resulting in a reactive milling process [2] [3]. The process's effectiveness depends on the factors that include the ball to powder ratio (BPR) and milling time, which determines the synthesized nanostructures' properties [4]. The variation of the parameters such as milling time and ball-to-powder (BPR) ratio allowed to modification of the properties of the T/M NCs during the synthesis [5] [6]. One of the most commonly employed approaches for removing arsenic from water is adsorption due to its advantages like high removal efficiency, simplicity, easy operation, wide pH range, low generation of harmful by-products, and low-cost [7] [8]. As pollutants widely affect developing countries, the treatment technique must be cost-effective and easy to operate [9]. Because of the low-cost, high adsorption capacity, and affinity towards As, the metal oxides, including γ-Fe_2O_3, TiO_2, CeO_2, CuO, ZrO_2, have been extensively employed in aqueous media [10] [11] [12] [13]. In order to enhance the adsorption behavior, two or more metal oxides are combined in an NC [14] [15] [16]. Here, one of the most suitable iron-oxide adsorbent, maghemite (γ-Fe_2O_3), which is more stable than magnetite (Fe_3O_4) is combined

with TiO_2 anatase to overcome the adsorption limitations of TiO_2 towards As (III) and As (V) [17]. In this work, the TiO_2 anatase and maghemite are synthesized by the sol-gel and co-precipitation method. Hence, the previous study's magnetite is not a stable phase; here, a stable maghemite phase is used for the studies. The TiO_2/γ-Fe_2O_3 nanocomposite (T/M NCs) were synthesized using the mechanochemical route. The T/M NCs were synthesized by varying BPR (10:1, 20:1, and 30:1) and different milling time (2 and 6 h) by mixing appropriate quantities of TiO_2 and γ-Fe_2O_3 and processed using a planetary ball mill with constant RPM of 300. The effect of BPR and milling time on T/M NCs and its effect on arsenic adsorption will be presented.

4.1 Results and Discussion

4.1.1 X-ray diffraction

The structural analysis using X-ray diffraction confirmed the successful synthesis of tetragonal TiO_2 anatase structure through the sol-gel method and cubic spinel γ-Fe_2O_3 structure from the co-precipitation method, with no secondary phases or impurities is shown in figure 4.1**.** A comparison of the lattice parameters of the synthesized nanostructures, calculated using equations 2.4 and 2.5, with the ICDD reference (No.00-064-0863-anatase, 00-039-1346-maghemite). Table 4.1 resulted in the comparable lattice parameters between the synthesized nanostructures and the referenced materials [18] [19] [20] [21]. The average crystallite size of TiO_2 and γ-Fe_2O_3 nanomaterials was estimated using equation 2.2, which is presented in table 4.2**.** Moreover, the associated dislocation density (δ) was estimated from the Dp (equation 2.6) and strain (equation 2.7). The calculated dislocation densities and the microstrain of the synthesized nanomaterials showed comparative values to those reported in the literature, which may be due to some interatomic diffusion that modifies the atomic lattice of the materials [19] [18].

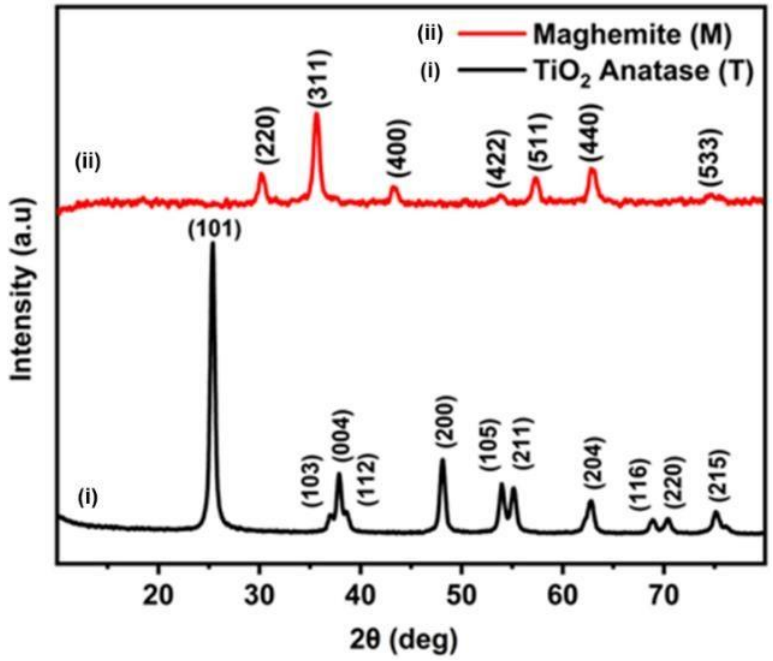

Figure 4.1 X-ray diffractograms of anatase (TiO_2) and maghemite spinel cubic structures obtained by sol-gel and co-precipitation methods, respectively.

Table 4.1 Comparison of the lattice parameters of synthesized TiO_2 and γ-Fe_2O_3 against the corresponding ICDD reference data.

Samples	**Experiment**					**Reference**				
	2θ	**d (Å)**	**a (Å)**	**c (Å)**	**c/a**	**2θ**	**d (Å)**	**a (Å)**	**c (Å)**	**c/a**
Anatase (TiO_2)	25.36	3.5091	3.7792	9.4872	2.5104	25.30	3.5163	3.7854	9.4937	2.7000
Maghemite (γ-Fe_2O_3)	35.65	2.5161	8.3431	-	-	35.66	2.517	8.3515	-	-

Table 4.2 The calculated crystallite parameters from XRD studies; crystallite sizes, dislocation densities, and strain of anatase and cubic maghemite.

Samples	2θ	FWHM	Dp (nm)	Error in Dp (nm)	Average δ ($x10^{-3}$ nm^{-2})	ε x 10^{-3}
Anatase (TiO_2)	25.36	0.5776	14	2.95	4.81	6.51
Maghemite (γ-Fe_2O_3)	35.65	0.7434	12	0.69	8.62	8.14

The synthesized TiO_2 and γ-Fe_2O_3 were processed by ball milling with varying milling time and BPR parameters. Composite of T/M NCs with BPR 10:1 milled for 2 h, figure 4.2a showed the prominent peaks corresponding to TiO_2 anatase and γ-Fe_2O_3 maghemite phases. By increasing the BPR (20:1) more friction between the balls was created, and thus generating more heat reaction during the milling [22] [22] [23]. This heat accounted for the decrease of the TiO_2 anatase peak and transformation of the γ-Fe_2O_3 to hematite (Fe_2O_3) and pseudorutile phases. Further increase in the BPR (30:1) presumably generated more heat and friction, resulting in the further decrement of the TiO_2 anatase peak and the rise of the secondary phases (hematite and pseudorutile). Milling for 6 h with the BPR of 10:1 showed similar results than their counterpart at 2 h in terms of TiO_2 phases, but with slightly reduced peak intensities attributed to the heat generated over a longer duration from attrition which is shown in figure 4.2b. Increasing the BPR (20:1) for 6 h showed a higher decay of the TiO_2 anatase phase with the appearance of the sharper and more intense peak of the pseudorutile phase along with the small shoulder peaks of the rutile phase. Similarly, the intensity of the maghemite peaks decayed, with more intense peaks of

hematite appearing. These changes in the peak intensities were ascribed to a change in the phases from anatase to pseudorutile for TiO_2 and γ-Fe_2O_3 to hematite phases when the milling time was prolonged at higher BPR due to the attrition effects. The same behavior of phase changes appeared using increased BPR (30:1) for 6 h, in which pseudorutile and hematite phases were the most prominent ones [6] [24].

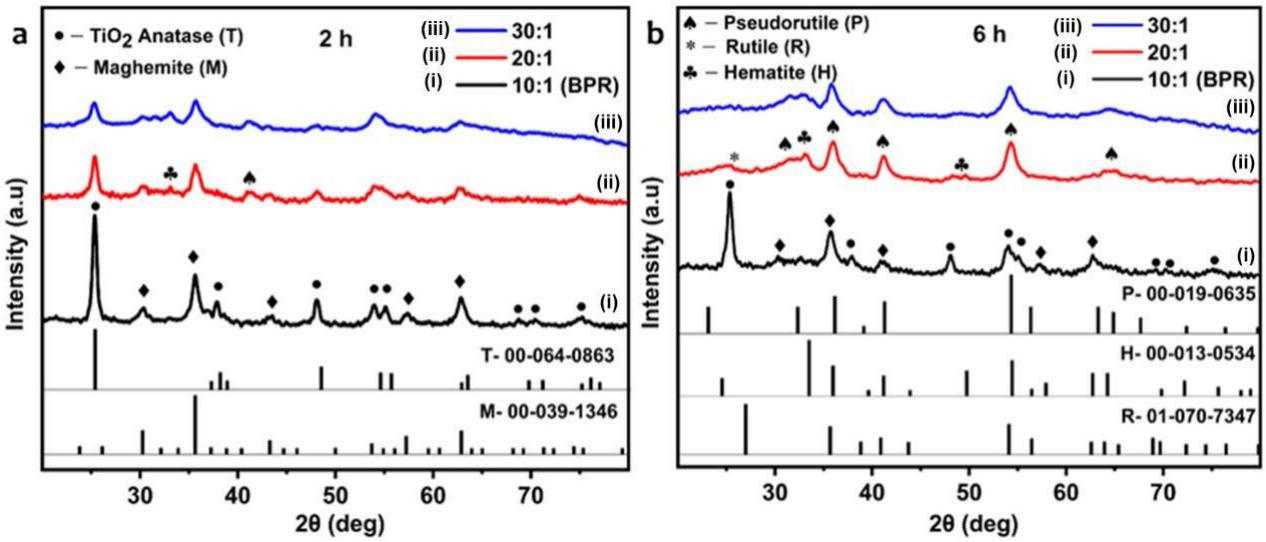

Figure 4.2 X-ray diffractograms of TiO_2: Maghemite (T/M) nanocomposite at different BPR for (a) 2 h and (b) 6 h (T-TiO_2 Anatase, M-Maghemite, H-Hematite, P-Pseudorutile, and R-Rutile)

The calculated crystallite sizes of the T/M NCs were taken from the most intense peaks corresponding to anatase (101) [25]. Results are shown in table 4.3, exhibiting a slight increase in crystallite size, from BPR 10:1 to 20:1, and then a decrease in BPR of 30:1. The same behavior was observed in samples milled through 6 h. The associated strain and dislocation densities followed a similar variation pattern compared with the XRD peaks and decreased and later increased. These changes in the structural phases of the synthesized composite structure may affect the adsorption process's performance. The intensity ratios of the prominent peaks of TiO_2 and γ-

Fe_2O_3, $I_{(101)}/I_{(311)}$ were calculated for all the T/M NCs synthesis, which is shown in figure 4.3. A higher fraction of anatase TiO_2 and γ-Fe_2O_3 phases above the ratio 1.2 were determined to be more suitable for the adsorption process, which was observed for BPR of 10:1 for both 2 and 6 h .

Table 4.3 The calculated crystallite parameters from XRD studies; crystallite size, dislocation densities, and strain for the different BPR and milling times

	2 h milling					**6 h milling**				
BPR	**2θ (degrees)**		**Dp (nm)**	**Δ ($x10^{-3}$ nm^{-2})**	**ε x 10^{-3}**	**2θ (degrees)**		**Dp (nm)**	**δ (x 10^{-3} nm^{-2})**	**ε x 10^{-3}**
	TiO_2	**Fe_2O_3**				**TiO_2**	**Fe_2O_3**			
10:1	25.36	35.63	13	5.71	9.04	25.36	35.69	12	7.17	11.0
20:1	25.36	35.67	15	4.56	8.89	25.34	35.99	14	5.47	9.40
30:1	25.30	35.69	11	8.03	11.6	25.38	35.75	9	11.8	10.9

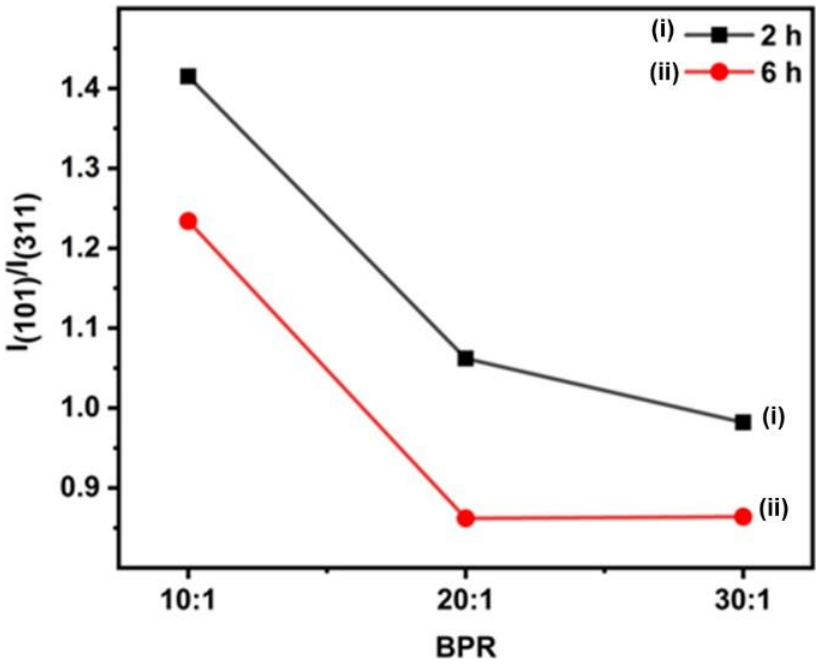

Figure 4.3 Comparison of the ratio of $I_{(101)}/I_{(311)}$ against the BPR for different milling times

4.1.2 UV-Visible diffuse reflectance studies

Generally, the bandgap is the energy difference between the valence band and the conduction band. Two different semiconducting materials which have unequal band gap forms a junction called heterojunction. These formations of heterojunction may form surface defects and create new states, which will change the materials' bandgap. These structural changes may occur without the induction of light also. Hence, bandgap studies were performed for the T/M NCs synthesized with different BPR and milling time. The obtained bandgap properties are correlated with the above XRD and RAMAN studies. The synthesized TiO_2 material has a bandgap of 3.2 eV, while the measured bandgap of the γ-Fe_2O_3 material was 1.95 eV which is shown in figure 4.4.

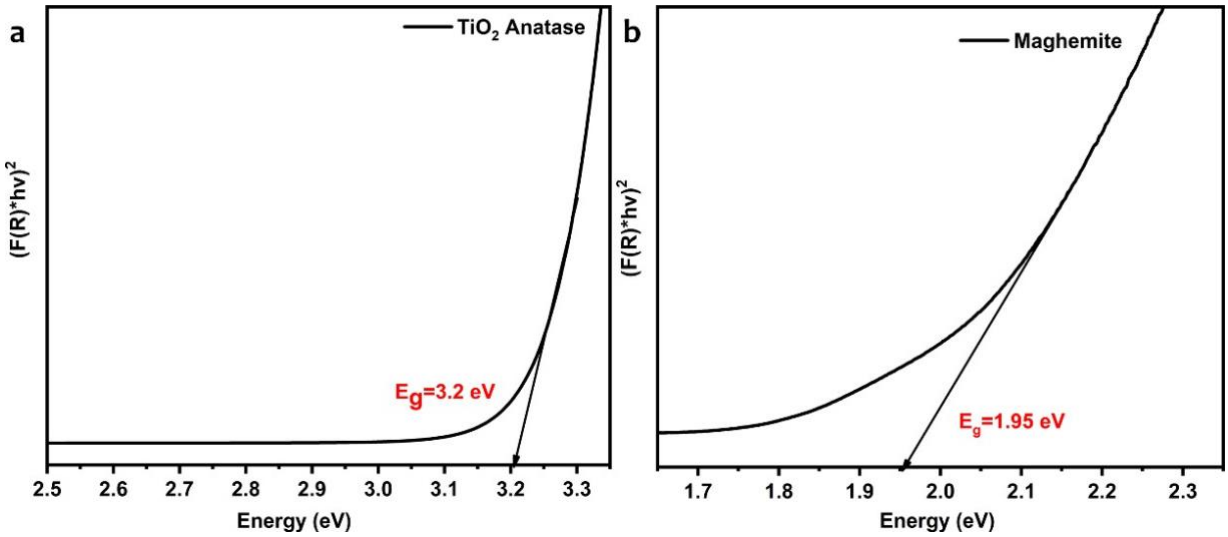

Figure 4.4 The bandgap of (a) TiO_2 and (b) Maghemite

The variation in band gap values for the different T/M NCs was associated with the aforementioned electron transfer, which seems to differ with the diverse phases of the NCs. The bandgap of ratios milled for 2 and 6 h shown in figure 4.5a exhibited minor variations, between 2.06 eV to 2.10 eV, respectively, being the BPR 20:1 sample with the lower value. The bandgap for milling at a BPR of 30:1 was increased to 2.10 eV. The bandgap of composites formed after 6

h of milling shown in figure 4.5b, increasing from 2.08 eV to 2.16 eV as the BPR raised. Thus, it is possible to allude that changes in the phases, from anatase to pseudorutile and from maghemite to hematite, caused the bandgap energy increment [26]. These bandgap results also follow a similar pattern to XRD and RAMAN; the change in the structural properties affects the bandgap of the material [27] [28]. The change in the bandgap is indirect evidence of T/M nanocomposite formation. The ionic radius of Fe^{3+} is 0.64 Å, and for Ti^{4+}, it is 0.745 Å. The bandgap's obtained change provides an indirect evidence of T/M NCs formation, i.e. Fe^{3+} is substitutes the Ti^{4+} sites [29] [27] [30] [31]. And further supports the Titania maghemite bond formation. In order to understand the clear charge transfer mechanism and band alignment between titania and maghemite, electrochemical and Mott-Schottky measurement has to be performed.

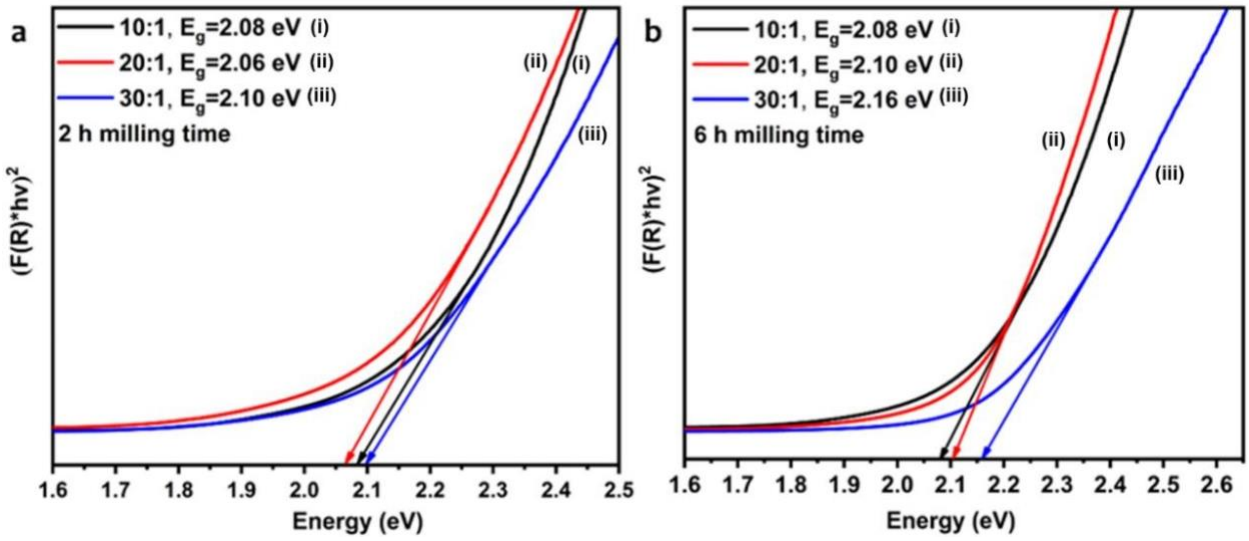

Figure 4.5 The bandgap energies of TiO_2 /maghemite composites for different ratios after milled for (a) 2 h and (b) 6 h

4.1.3 Raman spectroscopy

The Raman spectra for the NCs milled for 2 h with BPR of 10:1 shown in figure 4.6a, showed a broad peak centered at 153.6 cm^{-1} corresponding to the E_g vibrational mode of the TiO_2 anatase

phase [32], and smaller peaks at 195.6 cm^{-1} belonging to the γ-Fe_2O_3 phase [33]. The spectra of the material corresponding to a BPR of 20:1 showed the increased intensity of γ-Fe_2O_3 vibrational mode with a broad peak at 192.2 cm^{-1} and a small peak at 219.7 cm^{-1}, belonging to vibrations in the hematite phase. The changes in peak intensities could be due to the transformation in the composition, structure, and crystallinity of the material [34] [16], which is similar to the observations made by XRD. Increasing the BPR caused the increase in heat content during milling, and thus the alterations of the structure and composition of the materials. Further increase in BPR to 30:1 showed decreased peak intensity of the γ-Fe_2O_3 vibration mode and a shoulder peak at 218.9 cm^{-1}, corresponding to hematite. Therefore, an increase in BPR boosted the γ-Fe_2O_3 phase, with a reduction and apparent disappearance of the peaks belonging to the anatase TiO_2 vibration mode [25].

The Raman spectra for the different BPR millings at 6 h presented in figure 4.6b showed broad peaks at 152.0 cm^{-1} corresponding to the anatase vibrations. In addition to vibration modes for γ-Fe_2O_3 at 193.9 cm^{-1}, a small peak at 218.1 cm^{-1}, which may be attributed to the hematite phase was observed. Further increase in the BPR (20:1) showed an increased intensity of peaks belonging to γ-Fe_2O_3 vibrations (193. 9 cm^{-1}) and the disappearance of peaks corresponding to anatase TiO_2. The presence of peaks corresponding to hematite (219.7 cm^{-1}) suggested the conversion of γ-Fe_2O_3 to the hematite phase as BPR increased. Milling with a BPR of 30:1 caused a total change from TiO_2 anatase into rutile phase, which was evidenced by the B_{1g} vibration mode at 146.1 cm^{-1} [35], mostly in the 6h-30:1 sample, and the presence of hematite vibration modes at 191.4 cm^{-1}. These observations are similar to those reported in XRD analysis, which might be attributed to reactive heating accompanying the longer milling durations. These spectra support the observations from

XRD that milling with a BPR of 10:1 for 2 h or 6 h maintained both anatase and γ-Fe_2O_3 phases, while higher BPR produced the phase transformations.

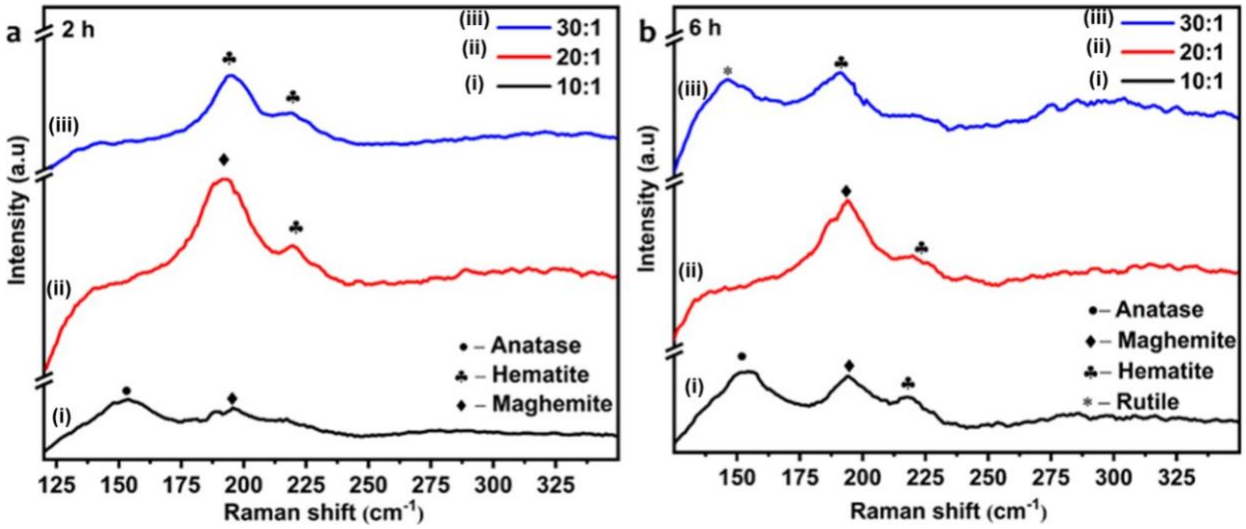

Figure 4.6 Raman spectra of TiO_2/maghemite composites for different ratios after milling for (a) 2 h and (b) 6 h

4.1.4 Morphological analysis

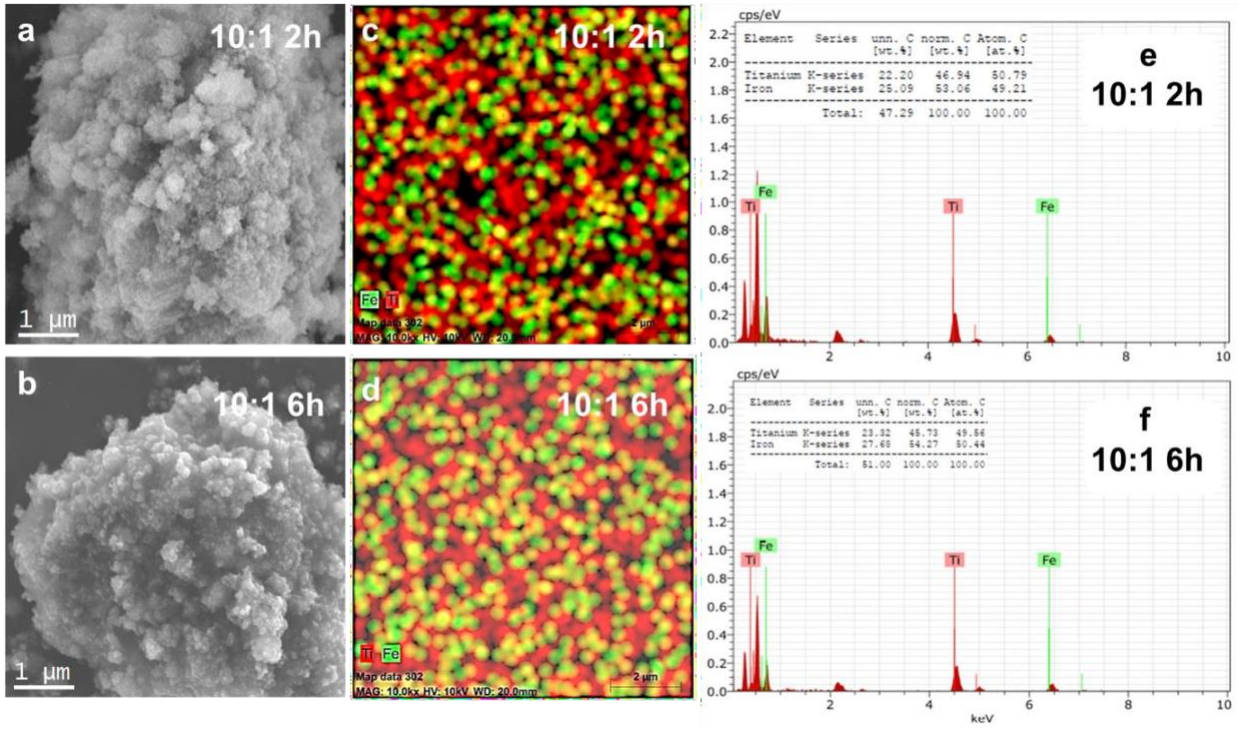

Figure 4.7 SEM images, elemental mapping and compositions of ball milled T/M NCs

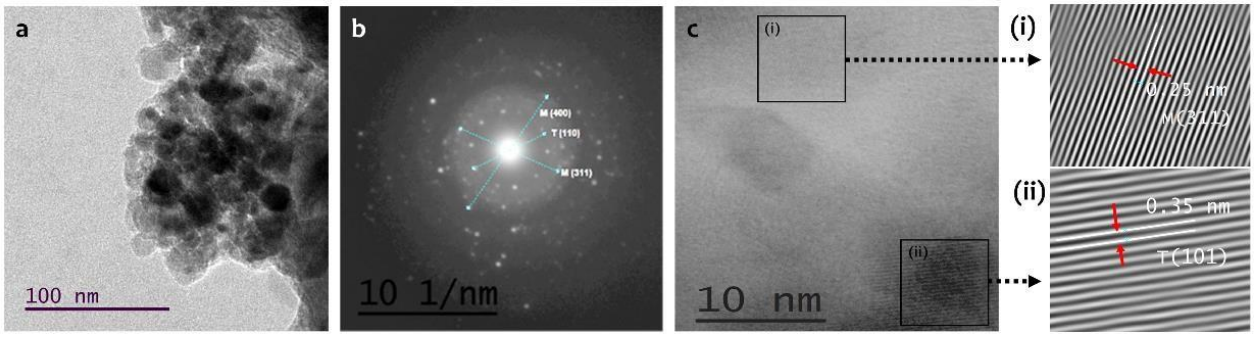

Figure 4.8 HRTEM micrographs of samples of T/M NCs with a BPR of 10:1 for 2 h showing the (a) particle size distribution, (b) SAED pattern, (c) fringes corresponding to inter-planar spacing, (i) Fe & (ii) Ti

Table 4.4 The elemental compositions of the ball milled T/M NCs

	2 h Milling		**6 h Milling**	
BPR	**%Fe**	**%Ti**	**%Fe**	**%Ti**
10:1	46.19	53.81	49.07	50.93
20:1	56.29	43.71	50.14	49.86
30:1	49.61	50.39	47.96	52.04

The SEM images, mapping, and EDS of the T/M NCs (10:1 - 2 & 6 h) are represented in figure 4.7 (a-f)**.** Figure 4.7 (a and b) shows the presence of nearly spherical-shaped nanoparticles with aggregation ascribed to attractive van der Waals forces occurring during the synthesis of NCs [36] [37]. The NCs were smaller in both the cases and thus possess higher relative surface area [38] [39]. Figure 4.7 (c and d) depicts the homogeneously distributed iron (Fe) and titanium (Ti) elements. The homogeneity is further confirmed from the elemental composition graph from figure 4.7 (e and f). The EDS spectrum of T/M NCs (10:1) demonstrated that Fe and Ti's atomic composition was 46.19 and 53.81% for the material milled for 2 h, and 49.07 and 50.93 % when milling took 6 h. This is very close to the desired stoichiometry for the ball milling process. The average elemental composition of all the samples is shown in table 4.3. The NCs synthesized using a BPR of 10:1 for 2 h showed the presence of spherical-shaped nanoparticles [40] [41] from the TEM micrograph, with the particle sizes ranging from 12 - 25 nm, which is shown in figure 4.8a. The SAED analysis of atomic arrangements [42] shown in figure 4.8b verified both Fe and Ti observations in the fringes and confirmed the presence of both phases in the nanocomposite. The d-spacing of the image shown in figure 4.8c (i and ii) were measured using inverse FFT, showing

fringes of 0.35 nm and 0.25 nm, which is consistent with the prominent (101) peaks of anatase TiO_2 and (311) cubic γ-Fe_2O_3 phases observed in XRD analysis which is presented in table 4.1.

4.1.5 XPS studies

XP spectra representing the binding energy (BE) of the synthesized anatase-TiO_2 and γ-Fe_2O_3 nanomaterials shown in figure 4.9a, showed the presence of the Ti 2s photoelectron spectrum at 565eV, and the Ti 2p peaks at 458 and 464 eV, corresponding to Ti $2p_{3/2}$ and Ti$2p_{1/2}$, respectively [43] [44]. The difference between the two peaks (ΔBE) was 6 eV, which is characteristic of Ti (IV) [45]. The Fe 2p spectrum showed two BE peaks at 710 eV and 723.5 eV, corresponding to Fe $2p_{3/2}$ and Fe $2p_{1/2}$, respectively. The difference between the two peaks (ΔBE) was 13.5 eV, which is the characteristic of Fe (III) ions present in maghemite [44] [46]. Spectral analysis of the T/M composites synthesized with a BPR of 10:1 for 2 and 6 hours shown in figure 4.9b, resulted in a ΔBE between Ti $2p_{1/2}$ (463 eV) and Ti $2p_{3/2}$ (468 eV) of ~5 eV. Similarly, the ΔBE between Ti $2p_{1/2}$ (460 eV) and Ti $2p_{3/2}$ (465 eV) for materials milled through 6 hours was ~5 eV, which is lesser than the value of the pure TiO_2. The decrease in ΔBE for Ti (IV) provided indirect evidence of Ti–O-Fe bond formation since the internal electric field promotes the transfer of electrons from Fe_2O_3 to TiO_2 [47]. The O 1s spectrum of TiO_2 and FeO appeared at 530 eV, corresponding to the lattice oxygen and O–H bond. The presence of H in the bond may be due to brief exposure to the ambiance. In the NCs, the BE of the O–H bond was less than that in TiO_2, which further supports the formation of the Ti–O–Fe bond in the nanocomposite [48].

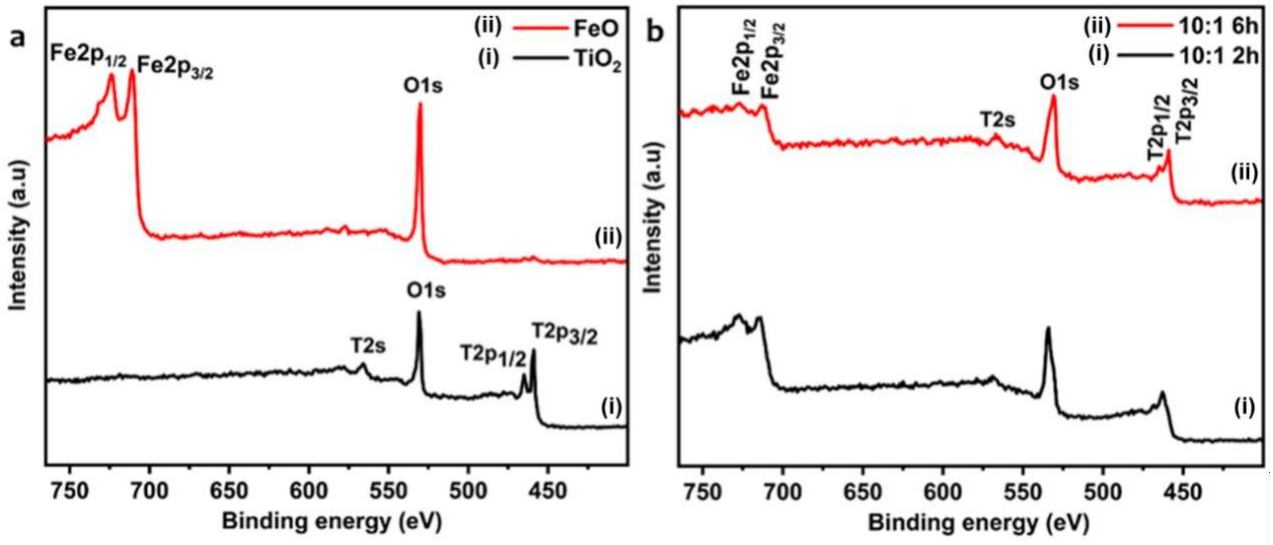

Figure 4.9 XPS spectra for (a) synthesized TiO_2 and maghemite nanostructures, and (b) T/M composites with BPR of 10:1, milled for 2 and 6 h

4.2 Adsorption of As (III) and (V) using T/M nanocomposites

Batch adsorption experiments were performed for the removal of As (III) and As (V). The experimental parameters used for the study are mentioned in chapter 2. The average percentage of As (III) and As (V) removal using the as-synthesized γ-Fe_2O_3 and TiO_2 is reported in table 4.5, where maghemite showed more removal than TiO_2. This was due to the high surface area and the availability of the functional groups present in γ-Fe_2O_3.

Table 4.5 The average removal of As (III) and As (V) (in percentage) using TiO_2 and maghemite

Samples	**As (III)**	**As (V)**
	% Removal	**% Removal**
TiO_2 Anatase	26 ± 1.18	18 ± 1.01
Maghemite	38 ± 0.8	25 ± 1.24

According to the literature, the iron oxide nanoparticle possesses a highly porous structure, a high-affinity hydroxyl-covered surface, and a high specific area of 10 to 450m^2 /g^{-1} [49] [50]. Under neutral pH, the iron oxide nanoparticles have the ability to remove both As (III) and As (V) [51]. Moreover, without the peroxidation and the pH adjustment, these iron oxide nanoparticles could effectively remove both As (III) and As(V) from groundwater [50]. Individual TiO_2 anatase also shows adsorption for both As (III) and (V); this is due to bidentate and monodentate inner-sphere complexes were formed with the TiO_2 surface during the adsorption [52]. It indicates that As (III) is not oxidized to As (V) during the adsorption process. Only the metal oxide and hydroxyl groups on the anatase nano-adsorbent are responsible for the heavy metal adsorption [53]. The nano adsorbents surface groups can react with heavy metals and directly form a stable inner-sphere and outer-sphere complex through electrostatic binding [54]. It forms superficial monodentate and bidentate complexes. However, the iron oxide nanoparticles are corrosive, and their surface area may decrease due to aggregation [55]. Hence both these excellent nano adsorbents were combined, and their adsorption properties towards arsenic were studied.

The average adsorption for As (III) using the different T/M NCs ratios synthesized for 2 h and 6 h are presented in figure 4.10**.** The obtained results are indirectly proportional to the performance as the BPR increased. The percentage removal for T/M NCs synthesis with BPR of 10:1 and 2 hours milling presented in figure 4.10a showed a better performance in As (III) removal, with an average value of 50%. In the case of 20:1 BPR, a larger crystallite size may affect the effective surface area, resulting in lesser adsorption. A further decline in the performance of 30:1 BPR may be attributed to the decrease in phase content and even lower (I_{101}/I_{311}) intensity ratio. The T/M NCs synthesized for 6 h presented in figure 4.10b showed a similar trend in declining performance

with increasing BPR due to the synthesized nanomaterials' properties. A comparison of the As (III) removal yields showed that NCs milled for 6 h appear to have a comparatively better performance than their 2 h counterparts. This relative improvement in performance could be due to their smaller crystallite size, leading to more crystallites in a given volume which may provide a larger surface area [56] [57].

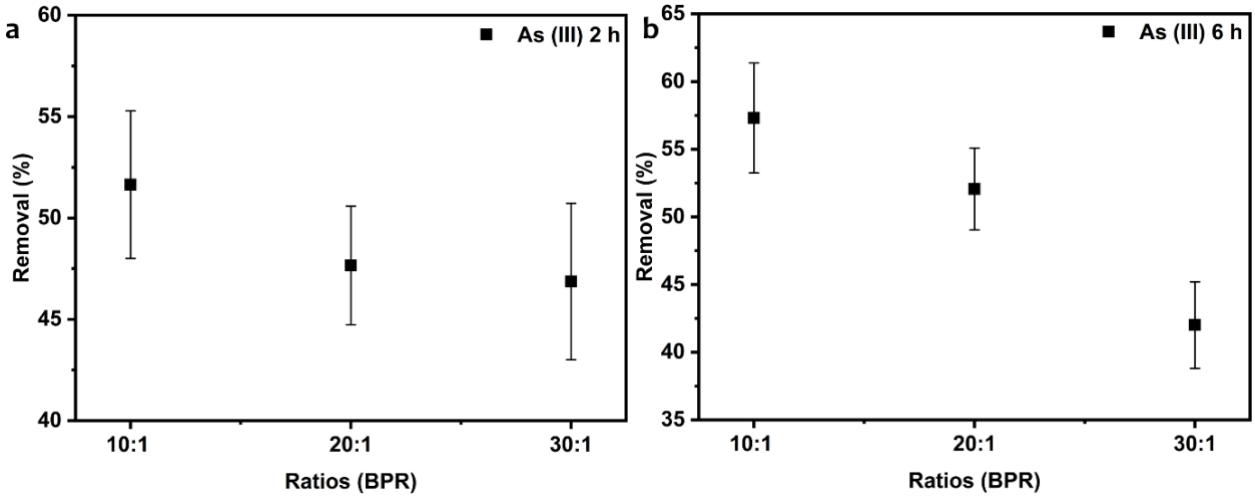

Figure 4.10 The removal % of As (III) with different BPR ratios (a) 2 h and (b) 6 h milling

The adsorption processes for removing As (V) using the NCs in both 2 h and 6 h presented in figure 4.11 showed reduced performances with increasing BPR. The T/M NCs with BPR 10:1 showed ~90% removal of As (V), which decreased with increased BPR ratios for both synthesis times. Since both NCs show similar performance with BPR 10:1 (2 and 6 h), an optimum time of 2 h could be employed for scaling-up the synthesis for industrial applications to As (V) removal. We carried out the adsorption processes for only 5 mins to verify the viability of materials synthesized using ball milling and optimizing the milling parameters in removing both As (III)

and As (V). The next phase of the study will be focused on modulating other parameters in adsorption tests (e.g., pH, temperature, dosage, concentration).

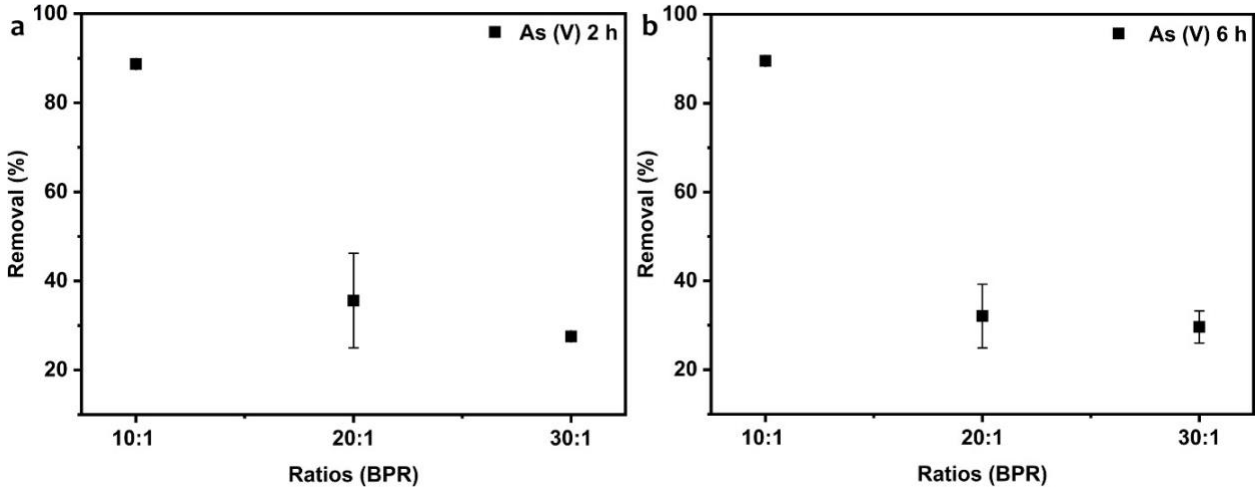

Figure 4.11 The removal % of As (V) with different BPR ratios (a) 2 h and (b) 6 h milling

4.4 Conclusion

In this work, the TiO_2 anatase and maghemite are successfully synthesized by sol-gel and co-precipitation method. Hence the magnetite is not a stable phase; here, a stable maghemite phase and synthesized TiO_2 are used for the studies. There are no secondary phases observed in the XRD. It shows the purity of the synthesis. The TiO_2 anatase nanoparticle with 14 nm and maghemite with 12nm were obtained. The difference in the binding energies obtained from XPS studies, 13.5 eV for maghemite and 5eV for anatase, confirmed the nanomaterials' successful synthesis. The TiO_2/γ-Fe2O3 nanocomposite (T/M NCs) were produced using the facile mechano-chemical route using the synthesized nanomaterials. The T/M NCs were synthesized by varying BPR (10:1, 20:1, and 30:1) and different milling time (2 and 6 h) on T/M NCs, and its effect on arsenic adsorption is presented. Synthesis XRD results showed the T/M NC with a BPR of 10:1 for both 2 and 6 h showed the presence of desired anatase and maghemite phases with the most intense peak ratio

above 1.2, showing desirable performance in As removal. For 20:1 and 30:1 BPR with 2 hour milling time, some phase changes in the anatase and maghemite were observed. For 20:1 and 30:1 BPR with 6 hour milling time, there is a complete phase change; the anatase phase was changed entirely to rutile, whereas the maghemite phase was changed entirely to hematite decreases the adsorption of arsenic. The Raman and UV-Vis analysis showed the same consistent behavior in accordance with XRD. Electron microscopy studies on the sample synthesized with a 10:1 for both 2 h (best ratio) presented particle shapes corresponding to the anatase TiO_2 phase. Studies using Raman spectroscopy for the vibration modes confirmed the structure's anatase and maghemite phases' presence and their respective transformations. XPS studies show a decrease in ΔBE for Ti (IV), which provided indirect evidence of Ti–O-Fe bond nanocomposite formation. The adsorption performed using the synthesized nanocomposites sowed better result for 10:1 BPR with 2 and 6 hours, milling time. These ratios have desired anatase and maghemite phases. Increasing the BPR and milling time causes phase change which is decreasing the adsorption of arsenic. The adsorption studies showed above 50% removal of As (III) and ~ 90 % performance in the removal of As (V) using nanomaterials synthesized using a BPR of 10:1 for both 2 and 6 h, respectively. Since 6h is a longer duration and there is not much difference between 2h and 6h. The T/M NCs with BPR 10:1 and 2 hour milling time are optimized as the best ratio and used in the next experiments.

4.5 References

[1] J.-L. Do and T. Friščić, "Mechanochemistry: A Force of Synthesis," *ACS Cent. Sci.*, vol. 3, no. 1, pp. 13–19, Jan. 2017, doi: 10.1021/acscentsci.6b00277.

[2] M. Rohini *et al.*, "Parametric optimization of mechanochemical process for synthesis of Cu(In, Ga) 0.5 Se 2 nanoparticles," *Mater. Sci. Semicond. Process.*, vol. 37, pp. 151–158, Sep. 2015, doi: 10.1016/j.mssp.2015.02.046.

[3] M. Cantarella *et al.*, “Mechanical milling: a sustainable route to induce structural transformations in MoS2 for applications in the treatment of contaminated water,” *Sci. Rep.*, vol. 9, no. 1, p. 974, Dec. 2019, doi: 10.1038/s41598-018-37798-8.

[4] J. F. De Carvalho, S. N. De Medeiros, M. A. Morales, A. L. Dantas, and A. S. Carriço, “Synthesis of magnetite nanoparticles by high energy ball milling,” *Appl. Surf. Sci.*, vol. 275, pp. 84–87, 2013, doi: 10.1016/j.apsusc.2013.01.118.

[5] W. Yang, S. J. Dong, A. Z. YangLi, and Z. X. Xie, “Synthesis of Al2O3-TiB2 composite powder by planetary milling from Al-TiO2-B2O3-Ni mixture,” *Appl. Mech. Mater.*, vol. 401–403, no. 2, pp. 734–737, 2013, doi: 10.4028/www.scientific.net/AMM.401-403.734.

[6] C. Suryanarayana, E. Ivanov, R. Noufi, M. A. Contreras, and J. J. Moore, “Phase selection in a mechanically alloyed Cu2013;In–Ga–Se powder mixture,” *J. Mater. Res.*, vol. 14, no. 2, pp. 377–383, Feb. 1999, doi: 10.1557/JMR.1999.0055.

[7] M. Tuzen, D. Çitak, D. Mendil, and M. Soylak, “Arsenic speciation in natural water samples by coprecipitation-hydride generation atomic absorption spectrometry combination,” *Talanta*, vol. 78, no. 1, pp. 52–56, 2009, doi: 10.1016/j.talanta.2008.10.035.

[8] T. Sumathi and G. Alagumuthu, “Adsorption studies for arsenic removal using activated Moringa oleifera,” *Int. J. Chem. Eng.*, vol. 2014, no. Table 1, pp. 1–7, 2014, doi: 10.1155/2014/430417.

[9] P. Z. Ray and H. J. Shipley, “Inorganic nano-adsorbents for the removal of heavy metals and arsenic: a review,” *RSC Adv.*, vol. 5, no. 38, pp. 29885–29907, 2015, doi: 10.1039/C5RA02714D.

[10] S. I. Siddiqui and S. A. Chaudhry, “Iron oxide and its modified forms as an adsorbent for arsenic removal: A comprehensive recent advancement,” *Process Saf. Environ. Prot.*, vol. 111, pp. 592–626, 2017, doi: 10.1016/j.psep.2017.08.009.

[11] T. A. Kurniawan, M. E. T. Sillanpää, and M. Sillanpää, “Nanoadsorbents for Remediation of Aquatic Environment: Local and Practical Solutions for Global Water Pollution Problems,” *Crit. Rev. Environ. Sci. Technol.*, vol. 42, no. 12, pp. 1233–1295, Jun. 2012, doi: 10.1080/10643389.2011.556553.

[12] D. D. La, T. A. Nguyen, L. A. Jones, and S. V. Bhosale, “Graphene-Supported spinel CuFe2O4 composites: Novel adsorbents for arsenic removal in aqueous media,” *Sensors (Switzerland)*, vol. 17, no. 6, 2017, doi: 10.3390/s17061292.

[13] J. A. Gomes, M. S. Rahman, K. Das, S. Varma, and D. Cocke, “A Comparative Electrochemical Study on Arsenic Removal Using Iron, Aluminum, and Copper Electrodes,” *ECS Trans.*, vol. 25, no. 28, pp. 59–68, Dec. 2019, doi: 10.1149/1.3309678.

[14] D. D. La, J. M. Patwari, L. A. Jones, F. Antolasic, and S. V. Bhosale, “Fabrication of a GNP/Fe-Mg Binary Oxide Composite for Effective Removal of Arsenic from Aqueous Solution,” *ACS Omega*, vol. 2, no. 1, pp. 218–226, 2017, doi: 10.1021/acsomega.6b00304.

[15] E. jbes Kowsari, “Semiconductor Nanocomposites for application of Photocatalysis,” pp. 203–249, 2016, doi: 10.1007/978-3-319-62446-4.

[16] S. U. N. Jiulong, “Development of Inorganic-Organic Hybrid Materials for Waste Water Treatment,” no. 1, pp. 36–37, 2014.

[17] S. Ashraf, A. Siddiqa, S. Shahida, and S. Qaisar, “Titanium-based nanocomposite materials

for arsenic removal from water: A review," *Heliyon*, vol. 5, no. 5, p. e01577, 2019, doi: 10.1016/j.heliyon.2019.e01577.

[18] M. C. Ceballos-Chuc, C. M. Ramos-Castillo, J. J. Alvarado-Gil, G. Oskam, and G. Rodríguez-Gattorno, "Influence of Brookite Impurities on the Raman Spectrum of TiO 2 Anatase Nanocrystals," *J. Phys. Chem. C*, vol. 122, no. 34, pp. 19921–19930, Aug. 2018, doi: 10.1021/acs.jpcc.8b04987.

[19] A. C. Khot *et al.*, "Bipolar resistive switching and memristive properties of hydrothermally synthesized TiO2 nanorod array: Effect of growth temperature," *Mater. Des.*, vol. 151, no. April, pp. 37–47, Aug. 2018, doi: 10.1016/j.matdes.2018.04.046.

[20] M. Aliahmad and N. Nasiri Moghaddam, "Synthesis of maghemite (γ-Fe2O3) nanoparticles by thermal-decomposition of magnetite (Fe3O4) nanoparticles," *Mater. Sci.*, vol. 31, no. 2, pp. 264–268, Apr. 2013, doi: 10.2478/s13536-012-0100-6.

[21] M. M. A. El-Latif, A. M. Ibrahim, M. S. Showman, and R. R. A. Hamide, "Alumina/Iron Oxide Nano Composite for Cadmium Ions Removal from Aqueous Solutions," *Int. J. Nonferrous Metall.*, vol. 02, no. 02, pp. 47–62, 2013, doi: 10.4236/ijnm.2013.22007.

[22] J. Marino-Salguero, J. Jorge, J. M. Menendez-Aguado, B. Alvarez-Rodriguez, and J. J. de Felipe, "Heat generation model in the ball-milling process of a tantalum ore," *Miner. Metall. Process.*, vol. 34, no. 1, pp. 10–19, Feb. 2017, doi: 10.19150/mmp.7244.

[23] M. I. Dar and S. A. Shivashankar, "Single crystalline magnetite, maghemite, and hematite nanoparticles with rich coercivity," *RSC Adv.*, vol. 4, no. 8, pp. 4105–4113, 2014, doi: 10.1039/C3RA45457F.

[24] J. A. Castrillón Arango, A. A. Cristóbal, C. P. Ramos, P. G. Bercoff, and P. M. Botta, "Mechanochemical synthesis and characterization of nanocrystalline Ni1-xCoxFe2O4 ($0 \leq x \leq 1$) ferrites," *J. Alloys Compd.*, vol. 811, p. 152044, Nov. 2019, doi: 10.1016/j.jallcom.2019.152044.

[25] J. I. Peña-Flores, A. F. Palomec-Garfias, C. Márquez-Beltrán, E. Sánchez-Mora, E. Gómez-Barojas, and F. Pérez-Rodríguez, "Fe effect on the optical properties of TiO2:Fe2O3 nanostructured composites supported on SiO2 microsphere assemblies," *Nanoscale Res. Lett.*, vol. 9, no. 1, p. 499, 2014, doi: 10.1186/1556-276X-9-499.

[26] C. Xia, Y. Jia, M. Tao, and Q. Zhang, "Tuning the band gap of hematite α-Fe2O3 by sulfur doping," *Phys. Lett. Sect. A Gen. At. Solid State Phys.*, vol. 377, no. 31–33, pp. 1943–1947, 2013, doi: 10.1016/j.physleta.2013.05.026.

[27] M. I. Danish, I. A. Qazi, A. Zeb, A. Habib, M. A. Awan, and Z. Khan, "Arsenic Removal from Aqueous Solution Using Pure and Metal-Doped Titania Nanoparticles Coated on Glass Beads: Adsorption and Column Studies," *J. Nanomater.*, vol. 2013, pp. 1–17, 2013, doi: 10.1155/2013/873694.

[28] F. E. Bortot Coelho, V. M. Candelario, E. M. R. Araújo, T. L. S. Miranda, and G. Magnacca, "Photocatalytic Reduction of Cr(VI) in the Presence of Humic Acid Using Immobilized Ce–ZrO2 under Visible Light," *Nanomaterials*, vol. 10, no. 4, p. 779, Apr. 2020, doi: 10.3390/nano10040779.

[29] M. Ji *et al.*, "Effective adsorption of Cr(VI) on mesoporous Fe-functionalized Akadama clay: Optimization, selectivity, and mechanism," *Appl. Surf. Sci.*, vol. 344, pp. 128–136, Jul. 2015, doi: 10.1016/j.apsusc.2015.03.006.

[30] M. R. Awual, M. A. Shenashen, T. Yaita, H. Shiwaku, and A. Jyo, “Efficient arsenic(V) removal from water by ligand exchange fibrous adsorbent,” *Water Res.*, vol. 46, no. 17, pp. 5541–5550, 2012, doi: 10.1016/j.watres.2012.07.038.

[31] R. A. Solano, A. P. Herrera, D. Maestre, and A. Cremades, “Fe-TiO 2 Nanoparticles Synthesized by Green Chemistry for Potential Application in Waste Water Photocatalytic Treatment,” *J. Nanotechnol.*, vol. 2019, pp. 1–11, Jan. 2019, doi: 10.1155/2019/4571848.

[32] L. Stagi, C. M. Carbonaro, R. Corpino, D. Chiriu, and P. C. Ricci, “Light induced TiO2 phase transformation: Correlation with luminescent surface defects,” *Phys. Status Solidi Basic Res.*, vol. 252, no. 1, pp. 124–129, 2015, doi: 10.1002/pssb.201400080.

[33] V. L. Skvortsova, M. I. Samoylovich, and A. F. Belyanin, “Studies of phase composition of contact sites of diamond crystals and the surrounding rocks,” *Dokl. Earth Sci.*, vol. 465, no. 1, pp. 1187–1190, Nov. 2015, doi: 10.1134/S1028334X15110215.

[34] M. Rezaee, S. M. Mousavi Khoie, and K. H. Liu, “The role of brookite in mechanical activation of anatase-to-rutile transformation of nanocrystalline TiO2: An XRD and Raman spectroscopy investigation,” *CrystEngComm*, vol. 13, no. 16, pp. 5055–5061, 2011, doi: 10.1039/c1ce05185g.

[35] S. Challagulla, K. Tarafder, R. Ganesan, and S. Roy, “Structure sensitive photocatalytic reduction of nitroarenes over TiO2,” *Sci. Rep.*, vol. 7, no. 1, pp. 1–11, 2017, doi: 10.1038/s41598-017-08599-2.

[36] X. Deng, Z. Huang, W. Wang, and R. N. Davé, “Investigation of nanoparticle agglomerates properties using Monte Carlo simulations,” *Adv. Powder Technol.*, vol. 27, no. 5, pp. 1971–1979, 2016, doi: 10.1016/j.apt.2016.06.029.

[37] J. Jia, J. C. Yu, X.-M. Zhu, K. M. Chan, and Y.-X. J. Wang, “Ultra-fast method to synthesize mesoporous magnetite nanoclusters as highly sensitive magnetic resonance probe,” *J. Colloid Interface Sci.*, vol. 379, no. 1, pp. 1–7, Aug. 2012, doi: 10.1016/j.jcis.2012.04.035.

[38] M. T. Rahman, M. Asadul Hoque, G. T. Rahman, M. A. Gafur, R. A. Khan, and M. K. Hossain, “Study on the mechanical, electrical and optical properties of metal-oxide nanoparticles dispersed unsaturated polyester resin nanocomposites,” *Results Phys.*, vol. 13, no. January, p. 102264, Jun. 2019, doi: 10.1016/j.rinp.2019.102264.

[39] Z. Wei *et al.*, “The effect of pH on the adsorption of arsenic(III) and arsenic(V) at the TiO 2 anatase [1 0 1] surface,” *J. Colloid Interface Sci.*, vol. 462, pp. 252–259, Jan. 2016, doi: 10.1016/j.jcis.2015.10.018.

[40] C. Y. Li, J. Bin Wang, and Y. Q. Wang, “Microstructure and photocatalytic activity of titanium dioxide nanoparticles,” *Chinese Phys. B*, vol. 21, no. 9, pp. 1–5, 2012, doi: 10.1088/1674-1056/21/9/098102.

[41] H. Cui, Y. Liu, and W. Ren, “Structure switch between α-Fe2O3, γ-Fe2O3 and Fe3O4 during the large scale and low temperature sol–gel synthesis of nearly monodispersed iron oxide nanoparticles,” *Adv. Powder Technol.*, vol. 24, no. 1, pp. 93–97, Jan. 2013, doi: 10.1016/j.apt.2012.03.001.

[42] J. Liu *et al.*, “Facet-Activity Relationship of TiO2 in Fe2O3/TiO2 Nanocatalysts for Selective Catalytic Reduction of NO with NH3: In Situ DRIFTs and DFT Studies,” *J. Phys. Chem. C*, vol. 121, no. 9, pp. 4970–4979, 2017, doi: 10.1021/acs.jpcc.6b11175.

[43] D. Chakrabortty and S. Sen Gupta, “Photo-catalytic decolourisation of toxic dye with N-doped titania: A case study with Acid Blue 25,” *J. Environ. Sci.*, vol. 25, no. 5, pp. 1034–

1043, May 2013, doi: 10.1016/S1001-0742(12)60108-9.

[44] T. Radu, C. Iacovita, D. Benea, and R. Turcu, “X-Ray Photoelectron Spectroscopic Characterization of Iron Oxide Nanoparticles,” *Appl. Surf. Sci.*, vol. 405, pp. 337–343, May 2017, doi: 10.1016/j.apsusc.2017.02.002.

[45] X. Zhang, J. Zhou, Y. Gu, and D. Fan, “Visible-Light Photocatalytic Activity of N-Doped TiO2 Nanotube Arrays on Acephate Degradation,” *J. Nanomater.*, vol. 2015, 2015, doi: 10.1155/2015/527070.

[46] D. D. La, J. M. Patwari, L. A. Jones, F. Antolasic, and S. V. Bhosale, “Fabrication of a GNP/Fe–Mg Binary Oxide Composite for Effective Removal of Arsenic from Aqueous Solution,” *ACS Omega*, vol. 2, no. 1, pp. 218–226, Jan. 2017, doi: 10.1021/acsomega.6b00304.

[47] D. Briggs, “X-ray photoelectron spectroscopy (XPS),” *Handb. Adhes. Second Ed.*, pp. 621–622, 2005, doi: 10.1002/0470014229.ch22.

[48] O. Akhavan, “Thickness dependent activity of nanostructured TiO 2 /α- Fe 2 O 3 photocatalyst thin films,” *Appl. Surf. Sci.*, vol. 257, no. 5, pp. 1724–1728, 2010, doi: 10.1016/j.apsusc.2010.09.005.

[49] A. P. Vieira *et al.*, “Adsorption of cysteine on hematite, magnetite and ferrihydrite: FT-IR, Mössbauer, EPR spectroscopy and X-ray diffractometry studies,” *Amino Acids*, vol. 40, no. 1, pp. 205–214, Jan. 2011, doi: 10.1007/s00726-010-0635-y.

[50] M. R. Awual *et al.*, “Efficient detection and adsorption of cadmium(II) ions using innovative nano-composite materials,” *Chem. Eng. J.*, vol. 343, no. January, pp. 118–127,

Jul. 2018, doi: 10.1016/j.cej.2018.02.116.

[51] S. Lata and S. R. Samadder, “Removal of arsenic from water using nano adsorbents and challenges: A review,” *J. Environ. Manage.*, vol. 166, pp. 387–406, Jan. 2016, doi: 10.1016/j.jenvman.2015.10.039.

[52] Y. Gao, R. Wahi, A. T. Kan, J. C. Falkner, V. L. Colvin, and M. B. Tomson, “Adsorption of Cadmium on Anatase NanoparticlesEffect of Crystal Size and pH,” *Langmuir*, vol. 20, no. 22, pp. 9585–9593, Oct. 2004, doi: 10.1021/la049334i.

[53] F. Beduk, “Superparamagnetic nanomaterial Fe 3 O 4 –TiO 2 for the removal of As(V) and As(III) from aqueous solutions,” *Environ. Technol.*, vol. 37, no. 14, pp. 1790–1801, Jul. 2016, doi: 10.1080/09593330.2015.1132777.

[54] M. D’Arcy, D. Weiss, M. Bluck, and R. Vilar, “Adsorption kinetics, capacity and mechanism of arsenate and phosphate on a bifunctional TiO2–Fe2O3 bi-composite,” *J. Colloid Interface Sci.*, vol. 364, no. 1, pp. 205–212, Dec. 2011, doi: 10.1016/j.jcis.2011.08.023.

[55] P. J. Vikesland, R. L. Rebodos, J. Y. Bottero, J. Rose, and A. Masion, “Aggregation and sedimentation of magnetite nanoparticle clusters,” *Environ. Sci. Nano*, vol. 3, no. 3, pp. 567–577, Jun. 2016, doi: 10.1039/C5EN00155B.

[56] C. Bueno-Ferrer, S. Parres-Esclapez, D. Lozano-Castelló, and A. Bueno-López, “Relationship between surface area and crystal size of pure and doped cerium oxides,” *J. Rare Earths*, vol. 28, no. 5, pp. 647–653, Oct. 2010, doi: 10.1016/S1002-0721(09)60172-1.

[57] M. H. Stietiya and J. J. Wang, “Zinc and Cadmium Adsorption to Aluminum Oxide

Nanoparticles Affected by Naturally Occurring Ligands," *J. Environ. Qual.*, vol. 43, no. 2, pp. 498–506, Mar. 2014, doi: 10.2134/jeq2013.07.0263.

5. CHAPTER 5 EFFECTIVE REMOVAL OF ARSENIC SPECIES USING MAGNETICALLY SEPARABLE TiO_2/Fe_2O_3 NANO-ADSORBENT

5. Brief Description

Among many currently available techniques, the adsorption technique for arsenic removal is considered one of the most promising because of its low cost, high efficiency, and ease of operation. The comparison of the adsorption technique with others is mentioned in chapter 1. The separation of arsenic contaminants after adsorption is a significant challenge in the drinking water treatment process. In recent days magnetic iron oxide-based materials are widely used in adsorption experiments for separating adsorbent and adsorbate from the water medium. It also provides a high affinity for both As (III) and (V). It only requires a low external magnetic medium to separate the contaminants. Only the aggregation limits its use; hence TiO_2, another promising adsorbent as discussed earlier, is combined with iron oxide, and its adsorption towards arsenic is studied.

From the previous studies, it is observed that the ball milling method is working well for arsenic removal. Using the optimized conditions (BPR and milling time) from the previous study, five different T/M NCs ratios are synthesized. The T/M ratios effect on arsenic adsorption is presented. After optimizing the ratio, a methodical adsorption study was performed. The World Health Organization's (WHO) maximum contaminant levels (MCL) of arsenic is 0.01 ppm [1] [2]. To achieve that limit, this work promotes a methodical adsorption study by optimizing the different parameters that affect the arsenic removal using $TiO_2/\gamma\text{-}Fe_2O_3$ nanocomposites (T/M NCs) through

a green, facile, and cost-effective ball milling method [3] [4]. The effect of adsorption factors, such as adsorbent dosage, contact time, initial concentration of arsenic, and pH, was studied extensively to obtain optimized conditions for the complete removal of this pollutant. It also offers the additional advantage of reusability and magnetic separation. To the best of our knowledge, the obtained results presented in the study are novel and with the synthesized NCs showing complete (100%) removal of As (III) and As (V).

Table 5.1 shows the arsenic removal by adsorption by different adsorbents synthesized by different methods. It is observed that, compared to the other synthesis methods, the ball milling mechanical technique provides complete removal for both As (III) and (V). This technique's further advantages include a greener and facile synthesis method, and it may not require any solvents or surfactants during synthesis [5] [6]. The milling process yields a more considerable amount of desired product with short processing time at ambient conditions. It is very attractive for industrial production. It eliminates waste generation from multi-step procedures, high temperature, and pressure requirements with no hazardous and expensive chemicals. The relatively low installation cost, use of a low-powered grinding medium, and offers availability for both batch and continuous operation make it suitable for large-scale industrial production [7] [8] [9] [10].

Table 5.1 Comparison of As removal with adsorbing nanomaterials reported in the literature and their synthesis methodology.

Adsorbing material	**Method of synthesis**	**Percentage removal**	**Reference**
GO-Fe_2O_3/TiO_2	Sol-gel method	As(III)~92% As(V)~92%	[11]
GNPs/$CuFe_2O_4$	one-pot hydrothermal method	As(V)~98%	[12]

TiO_2 anatase	Hydrothermal method	As(III)~70% As(V)~70%	[13]
Fe_3O_4	AACVD technique	As(III)~88% As(V)~100%	[14]
GNPs/Fe−Mg	One-pot hydrothermal method	As(V)~98%	[15]
Concrete/maghemite	Simple mixing method	As(V)~98%	[16]
Chitosan magnetic GO	Co-precipitation	As(III)~61%	[17]
chitosan/GO-Gd nanorods	Co-precipitation hydrothermal method	As(V)~99%	[18]
FeOOH/CuO@WBC	Two-step hydrothermal process	As(III)~75%	[19]
Fe_3O_4–TiO_2	Co-precipitation	As(III)~93% As(V)~94%	[20]
TiO_2/γ-Fe_2O_3	Ball-milling	As(III) and As(V)~100%	This work*

GO – graphene oxide, TiO_2 – titanium oxide, Fe_2O_3 – hematite, Fe_3O_4 – magnetite, γ-Fe_2O_3 – maghemite, GNPs – gold nanoparticles, $CuFe_2O_4$ – copper iron-oxide, Mg – magnesium, Gd – gadolinium, FeOOH – iron oxyhydroxide, CuO – copper oxide, WBC – water bamboo cellulose.

5.1. Results and discussion

5.1.1 Structural studies using XRD

The X-ray diffractograms for the different ratio of T/M NCs is shown in figure 5.1. The prominent peaks of anatase TiO_2 (ICDD 00-064-0863) increased proportionately from 1/9, moving to 9/1, as appeared the peaks of cubic spinel structured γ-Fe_2O_3 (ICDD 00-039-1346) depreciates

[21]. The peak positions of TiO_2 shifted towards lower 2θ values (25.46 to 25.34) as the ratio increased with the decrement of γ-Fe_2O_3. The milled NCs showed neither phase changes nor the presence of any secondary phases, which shows the purity of the synthesis. The calculated crystallite sizes for the T/M NCs by considering the most intense peaks, mentioned in table 5.2, showed an increment in the crystallite size as the TiO_2 composition increased, which is consistent with the observation that TiO_2 had a larger crystallite size than γ-Fe_2O_3 [21] [22]. The prominent peaks' ratios ($\mathbf{I_{(101)}/I_{(311)}}$) also showed a consistent variation, which decreased while the γ-Fe_2O_3 composition increased.

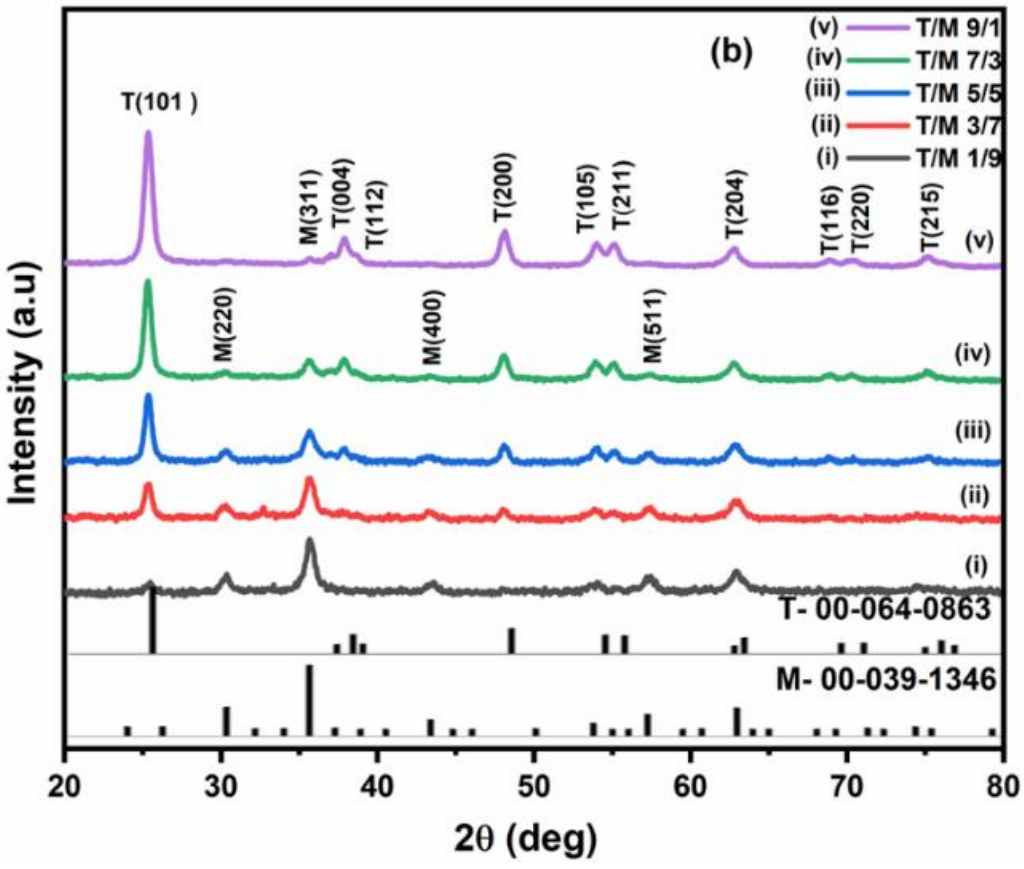

Figure 5.1 X-ray diffractograms of T/M nanocomposites at different ratios: 1/9, 3/7, 5/5, 7/3, and 9/1

Table 5.2 The calculated crystallite parameters from XRD studies for the different ratios

T/M NCs ratios	2θ (degrees)		Average Dp (nm)	$I_{(101)}/I_{(311)}$
	TiO_2	Fe_2O_3		
9/1	25.34	35.69	13	6.94
7/3	25.34	35.57	14	2.46
5/5	25.38	35.67	13	1.42
3/7	25.40	35.73	12	0.95
1/9	25.46	35.67	10	0.76

5.1.2 Morphological studies

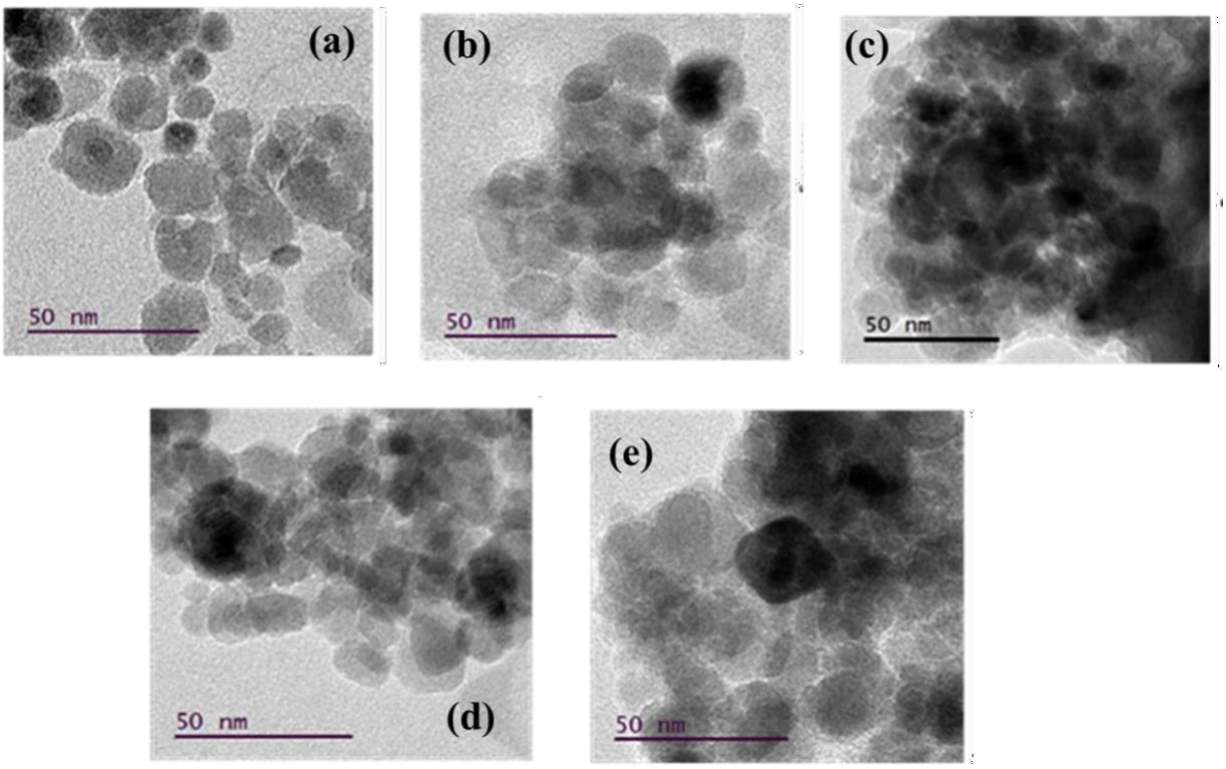

Figure 5.2 Micrographs obtained from the HRTEM image analysis for different ratios of T/M NCs

The morphology of the synthesized T/M NCs shown in figure 5.2 was studied using HRTEM characterizations that showed nearly spherical-shaped nanoparticles [23], with size distribution and reduced aggregation. The particle-size distribution histograms fitted with log-normal function for peak values. Figure 5.3 shows that the average particle size ranged between 15 and 20 nm. The distribution showed that average particle sizes increased with increasing TiO_2 ratios, corroborated with XRD.

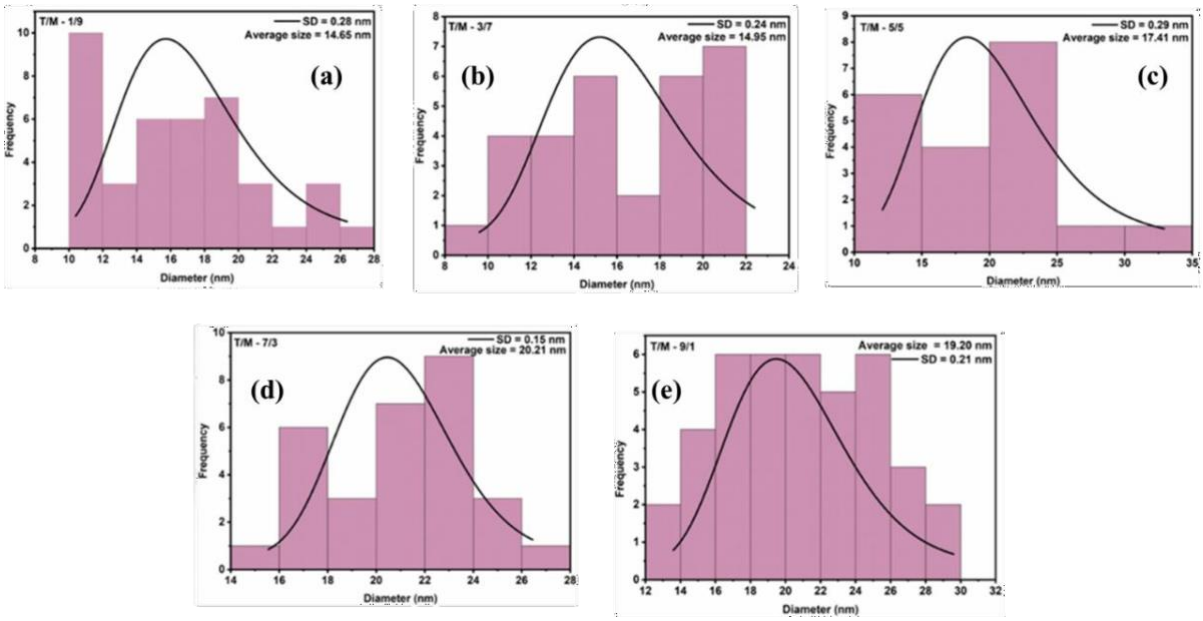

Figure 5.3 Particle size distribution from the HRTEM image using the log-normal function for average size estimations

The estimation of the *d*-spacing using the image from T/M (5/5) NC shown in figure 5.4 was measured using an inverse Fast Fourier Transform (FFT). It showed fringes of 0.35 nm and 0.25 nm, corresponding to the prominent (101) peaks of anatase TiO_2 and (311) cubic for γ-Fe_2O_3 [24] [25]. These results also verified the observations on the presence of both phases in the nanocomposite.

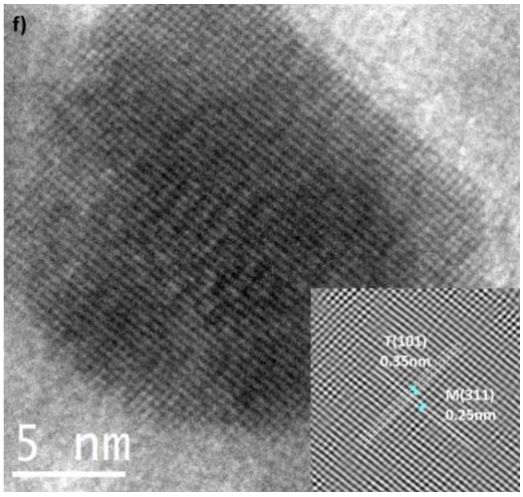

Figure 5.4 HRTEM micrograph of T/M (5/5) NCs fringes corresponding to the inter-planar spacing

5.1.3 UV-Visible diffuse reflectance analysis

The bandgap studies were performed for the different ratios of synthesized T/M NCs, which is shown in figure 5.5. These studies support the structural variations of T/M NCs observed in the XRD. The bandgap values obtained for the synthesized anatase-TiO_2 is 3.2 eV, and γ-Fe_2O_3 is 1.95 eV from previous studies. For the T/M NCs with more TiO_2 content shows a bandgap almost equal to titania; increasing the maghemite content decreases the bandgap of the material. For the higher maghemite content, the bandgap is almost 2eV. The ionic radius of Fe^{3+} is 0.64 Å, and for $Ti^{4+,}$ it is 0.745 Å. The change in the bandgap's obtained change provides indirect evidence of T/M NCs formation, i.e., Fe^{3+} substitutes the Ti^{4+} sites [26] [27] [28]. The obtained results followed a similar pattern consistent with XRD; increasing the maghemite content decreases the crystallite size and bandgap of T/M NCs and it is shown in table 5.3.

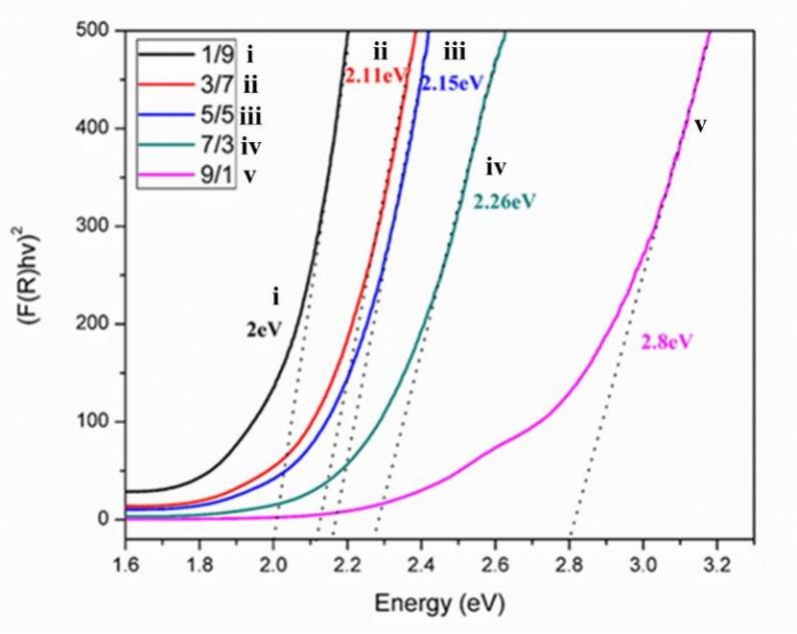

Figure 5.5 Bandgap energy estimations for the different T/M NCs ratios

(1/9, 3/7, 5/5, 7/3, and 9/1)

Table 5.3 Compiled and comparison table of average crystallite, particle sizes, and bandgap of different T/M NCs

Ratios (T/M NCs)	**Crystallite size (nm)**	**Particle size (nm)**	**Bandgap (eV)**
9/1	13	19	2.8
7/3	14	20	2.26
5/5	13	17	2.15
3/7	12	15	2.11
1/9	10	15	2

5.2 Adsorption using the synthesized T/M NCs with different ratios

The adsorption studies of As (III) and (V9 using the different NCs ratios (1/9, 3/7, 5/5, 7/3, and 9/1) and varying parameters were evaluated to optimize the best ratio for the effective removal of As species. The adsorption studies of As (III) and As (V) using the various T/M NCs ratios were determined with a constant dosage of 0.5 g/L, pH = 7, 2 ppm arsenic initial concentration, and 5 mins of contact time. Figure 5.6a shows an optimal As (V) removal with the T/M composition of 5/5; however, the removal of As (III) was marginally better with the material displaying a 3/7 composition. This performance is attributed to higher γ-Fe_2O_3 composition in the composite, which may be due to more adsorption sites and reduction in the agglomeration of TiO_2.

A higher composition of γ-Fe_2O_3 (i.e., 1/9) may produce aggregation during the adsorption processes. Contrarily, the material with higher loading of TiO_2 presented lower performances because of the agglomerations. Similarly, a plot of the ppm concentration against the various ratios Figure 5.6b showed a minimal value with 5/5 ratios for As (V) removal and comparatively better performance with 3/7 composition for As (III) removal. Generally, the NCs at all the ratios showed better As (V) removal compared with that obtained for As (III). This is consistent with the literature work that As (V) is simpler to remove than As (III) [29].

The choice of 5/5 ratio offered almost equivalent compositions of Fe and Ti in the NCs shown in table 5.1 and the parameters desirable for adsorption properties, tapping almost equivalent distribution of the physical properties of both TiO_2 and γ-Fe_2O_3. The ratio also offered the potential to optimally remove both As (III) and As (V) simultaneously. Thus, the subsequent adsorption processes and optimizations in this study were mainly focused on the 5/5 ratio of T/M NCs ratio based on the preliminary data.

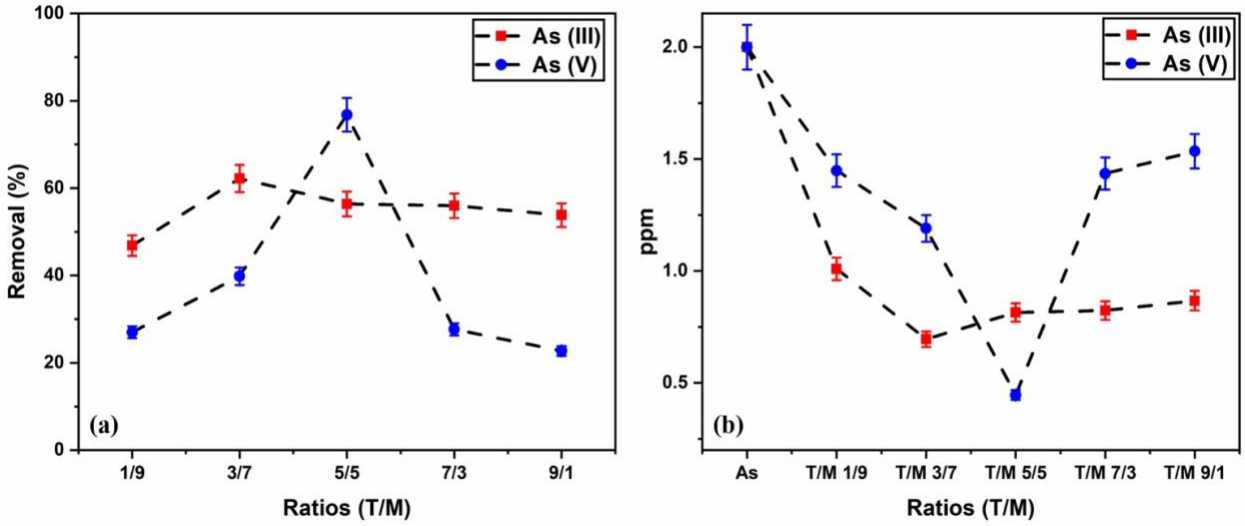

Figure 5.6 As (III) and (V) removal in (a) percentage and (b) ppm concentration, using a constant 0.5 g/L dosage, pH 7, and 2 ppm concentration for 5 mins for various T/M NCs ratios

5.3 Study on adsorption parameters using optimized T/M NC

The performance of the fabricated nanomaterials for As removal depends on certain prevalent ambient conditions, for example, pH, initial concentration of the adsorbate, stirring time, and dosage of the adsorbent. Thus, the systematic study of these conditions will provide an in-depth understanding of the nano adsorbent's better-operating conditions. Furthermore, efficient applications can allow for better utilization and reusability of the adsorbing materials. Therefore, this study aims to elucidate various factors and their influence on As adsorption using the nano-adsorbents.

5.3.1 Effect of the nano-adsorbent dosage

The dosage is an important parameter, and it refers to the nano adsorbents concentration used in the adsorption process. Here in this study, the different adsorbent dosages (0.5, 2, 4, 6, and 8 g/L) were studied by keeping the other parameters as constant such as pH-7, contact time- 5 min, and As (III) and (V) concentration 2ppm. The arsenic concentration (ppm) vs. adsorbent dosage

graph is plotted to show the maximum contamination limit (MCL) values for varying the adsorption parameters. In figure 5.7a, it is observed that increasing the adsorbent dosage amount increases the adsorption of both As(III) and (V). Increasing the dosage increases the active site's availability and, therefore, the presence of surface functional groups' providing active exchangeable adsorption sites in the NCs. The observed effect is consistent with the literatures [30] [31] [32] [33] [34]. Therefore, there is a vital need to optimize the dose of an adsorbent to achieve effective removal. An optimal dosage of 8 g/L provided As (III) removal shown in figure 5.7b, below the MCL set by the WHO [35]. Hence it is observed that with neutral pH and less contact time 5 min, it is possible to achieve arsenic removal with WHO standard. As (V) also shows almost 75% removal, the observed performance in As (V) removal may be due to pH or inefficient contact time for optimal removal. Therefore the need for other optimization parameters was carried out.

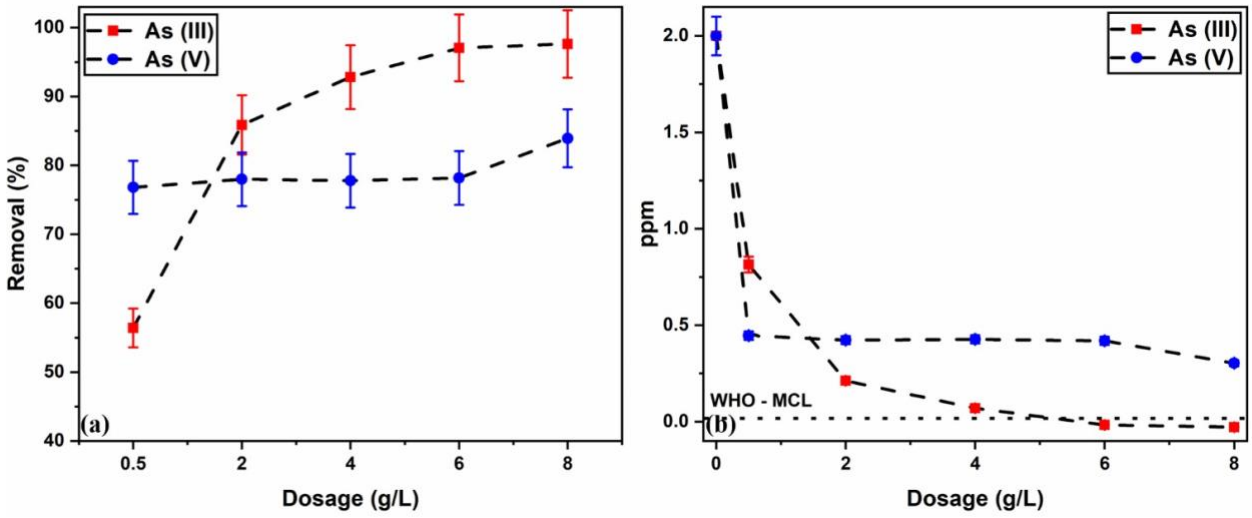

Figure 5.7 As (III) and As (V) removal using various dosages in (a) percentage and (b) ppm with pH 7, 5 mins contact time and 2ppm arsenic concentration

5.3.2 Effect of contact time

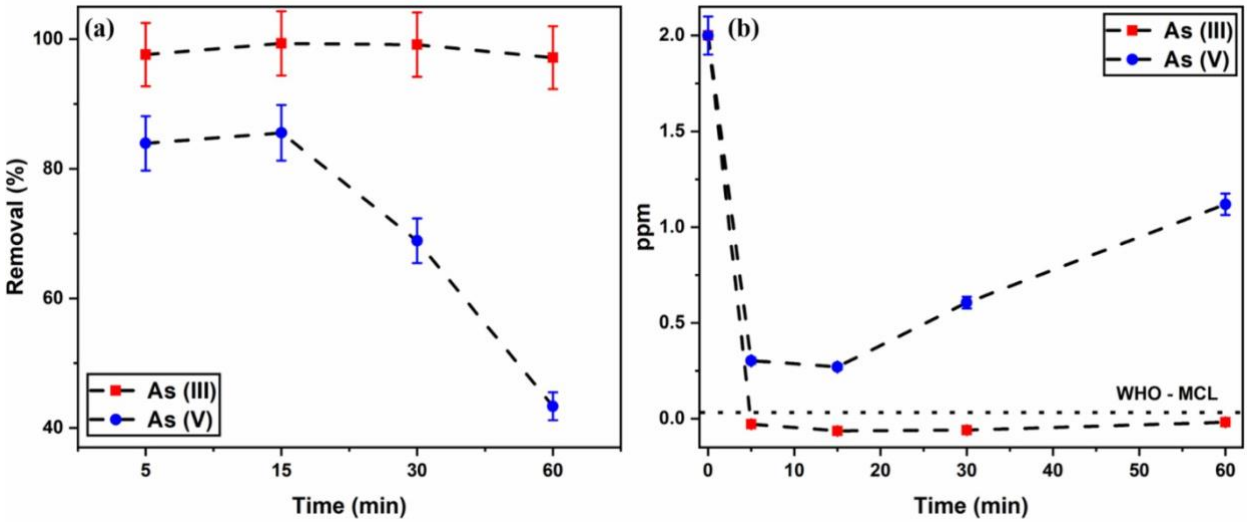

Figure 5.8 As (III) and As (V) removal using various time in (a) percentage and (b) ppm with pH-7, dosage 8g/L and arsenic concentration 2ppm

The contact time is an essential factor affecting the adsorption process. It can also influence the economic efficiency of the process and the adsorption kinetics [36]. Therefore, the effects of time on adsorption were carried out for different time durations. From figure 5.8, the highest removal rate was observed in the initial stages of the experiment (between 5 and 15 mins) because of the many adsorption sites' availability [36]. Further increase in the duration produced a marginal decrease in the adsorption efficiencies for As (III) and even lower in the case of As (V). It proves that the consideration of contact time remains vital in adsorption studies and processes to control the effects of saturation of the adsorbents' active sites, thereby avoiding potential leaching of the As species back into the media. As the time prolonged, the adsorbent sites are filled and saturated with more adsorbates which may reduce the adsorption of arsenic. Hence, As (III) and As (V) into the media at longer periods (30 mins and beyond) may account for the observed decrease in the

removal percentage [37]. From the results, the contact time of 5 and 15 minutes yielded an optimal removal of As (III) and (V), respectively. Hence 15 minutes is optimized as the best contact time.

5.3.3 Effect of the initial concentration of Arsenic

An initial concentration of arsenic is another important parameter that significantly influences the removal of the arsenic species. Hence the concentration is varied (2, 4, and 6ppm) by keeping the pH-7, optimized time-5min, optimized dosage-8g/L as constant. It is observed that at low arsenic concentrations, the arsenic removal was high. Because at low concentrations of the adsorbate, the surface area, adsorption sites, and availability of the adsorbents are relatively high, allowing for instantaneous adsorption [38]. However, for the higher concentrations (2 and 6ppm), all the available adsorption sites are less, thus decreasing the removal percentage, which is shown in figure 5.9a. Consequently, the removal percentage of an adsorption process purely depends upon the ratio of the number of adsorbate moiety to the adsorbent's available active sites in a particular environment [39]. This ratio also relates to the adsorbent's surface coverage (number of active sites occupied/number of active sites available), increasing the number of adsorbate moiety per unit volume of solution at a fixed dose of an adsorbent. A lesser ratio depicts more sites' availability, which gradually increases with the decrease in adsorbates resulting in the increased removal. In this study, a maximum of (~100%) As (III) removal for all the initial concentrations (i.e., 2, 4, and 6 ppm), the WHO MCL level is reached for all the concentrations, which is shown in figure 5.9b. The decrease in the As (V) adsorption performance is due to the speciation of As (V) under neutral pH [38] [39]. Hence in this study, 2ppm is optimized as the best concentration because it shows maximum removal for both As(III) and (V). In order to achieve complete removal for arsenic, pH studies were carried out, and it is presented below.

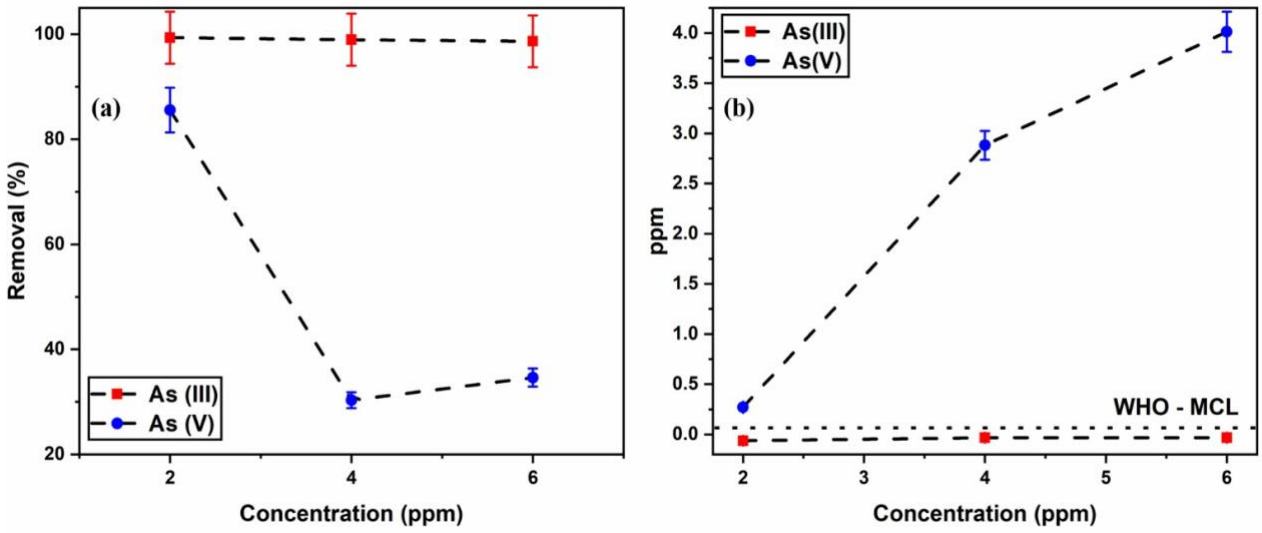

Figure 5.9 As (III) and As (V) removal using various concentrations in (a) percentage and (b) ppm with pH 7, 5 mins contact time, and 8g/L dosage

5.3.4 Effect of pH

The pH remains a critical variable affecting the speciation of As, and it also modifies the adsorbent's surface and the charge present functional groups, e.g., OH^- [40]. Hence the varying pH are varying between acidic (pH 4), neutral (pH 7), and alkaline (pH 10) media by keeping the optimized time-5min, dosage-8g/L, and concentration 2ppm as constant, which is shown in figure 5.10a. The constraints posed by pH in the aqueous media significantly affect the degree of speciation of As species and the charge of the adsorbent surface. The adsorption of arsenic on metal oxides involves interactions between the adsorbate and the functional group. At low pH, the hydroxyl groups at the iron oxide surface are doubly protonated [41]. At a neutral pH, the hydroxyl group is protonated with only one proton, and thus, the net surface charge of the iron oxide surface is neutral [42] [41]. This pH is termed as a point of zero charges (PZC). It ranges between 5.5 and 9. At pH values above the PZC, the hydroxyl group is deprotonated, and consequently, the iron oxide surface bears a negative charge [43] [44]. This favors the maximum adsorption of arsenic at

acidic pH values (around 4). At these pH values, the electrostatic attraction between the negative oxyanion and the positive charge of the adsorbent surface favors adsorption. At pH values above the point of zero charge, the adsorbent surface is negatively charged and repels the negatively charged arsenic species [45]. The modifications due to Fe-Ti oxides combination provided other functional groups at the surface and possibly acquired more positive charges at various pH, thereby maximum adsorption capacity for As (III) and As (V) using the binary composite oxide [46] [47]. The optimal results at pH 4, well the WHOs MCL limit was achieved for both As(III) and (V), and it is shown in figure 5.10b. It showed the NCs efficiently remove both As (III) and (V) contaminants present in water. Thus the acidic pH (around 4.0) favors maximum adsorption capacity for arsenic due to their anionic forms, which is consistent with the reported literature results [48] [47] [49] [50] [51]. These assumptions are based on the literatures. In order to understand the exact mechanism between the adsorbate and adsorbent, electrochemical or FTIR studies has to be studied.

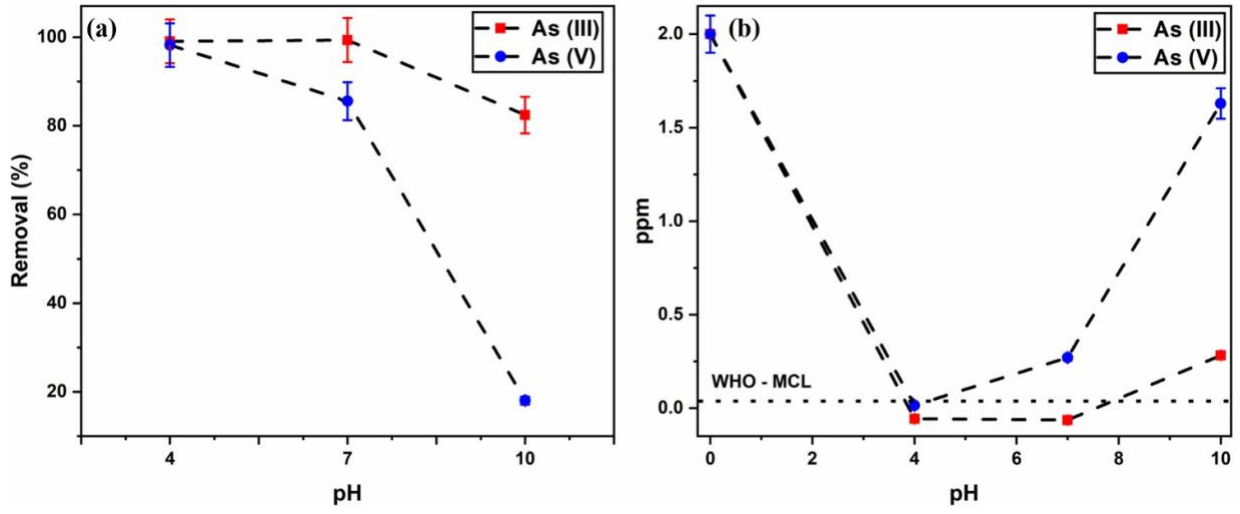

Figure 5.10 As (III) and As (V) removal using various pH in (a) percentage and (b) ppm with 8g/L dosage, 5 mins contact time and 2ppm arsenic concentration

5.3.5 Reusability test

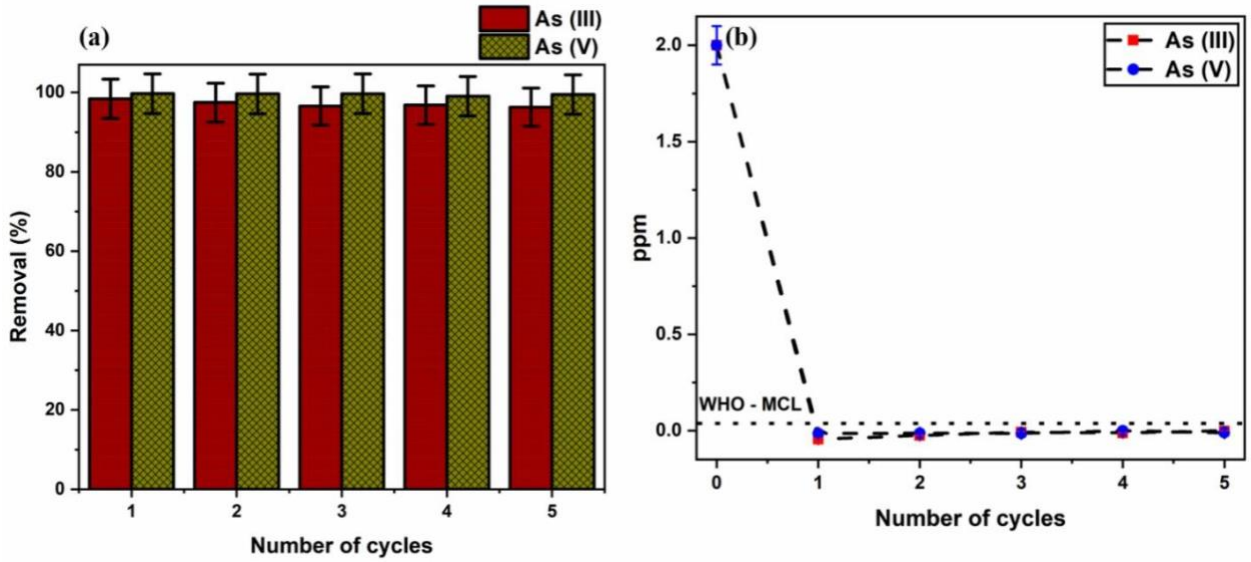

Figure 5.11 Reusability studies using the optimized T/M NCs

From the above adsorption parameters studies, the achieved optimum conditions were 8 g/L adsorbent dosage, 15 mins contact time, 2 ppm concentration, and pH 4. Based on this, the NCs' reusability test has to be performed, especially for industrial or practical applications. Reusability can reduce the cost of material synthesis and increase the process's economic value without compromising the results' quality [52]. The reusability test of the T/M NCs performed after each adsorption process involved the separation of the adsorbent using a strong magnet and then directly reused for the next sorption without any regeneration [46]. After five treatment cycles, the concentrations of As (III) and (V) were still below the 0.001 ppm prescribed by the WHO which is shown in figure 5.11, indicating that the T/M NCs adsorbent could be safely reused several times without regeneration, and a single step of purification would be feasible using this

adsorbent. It also prevents the generation of residual sludge, potentially reducing the overall cost of the water treatment process [51].

5.4. Conclusion

In this work, the TiO_2/γ-Fe_2O_3 (T/M) nanocomposites were synthesized using facile ball-milling using optimized BPR and milling time. The milled nanocomposites' structural studies showed no phase changes or presence of any secondary phases for all the synthesized ratios. The morphological studies showed spherical particles' presence, with d-spacing values of 0.35 nm and 0.25 nm corresponding to the (101) and (311) planes belonging to the anatase TiO_2 and cubic γ-Fe_2O_3 phases. The studies also showed variation in the crystallite and particle sizes, which decreases with increasing the maghemite content and the bandgap of the nanocomposites. The adsorption studies reveled the T/M 5/5 ratio works good for both As (III) and (V). An optimal T/M (5/5) NC ratio employed for the adsorption studies focused on optimizing the factors which may affect arsenic removal; dosage, time, concentration, and pH. The variation of each parameter was performed by keeping the other things as constant. The optimized results are adsorbent dosage 8g/L, contact time 15 minutes, pH-7, and concentration 2ppm. With these optimized conditions, 100% removal, well below the WHOs recommended permissible concentration (0.01 ppm) for As (III) and (V) was reached. Further reusability test showed the synthesized NC offers additional advantages since the T/M NC are magnetic separable and reusable for several cycles, making it more economical for water treatment. To the best of our knowledge, the obtained results presented in the study are novel. It proves the synthesized nanocomposite can be a potential candidate for effective removal of arsenic and can be implemented in large-scale applications currently underway.

5.5 References

[1] S. Iftekhar, D. L. Ramasamy, V. Srivastava, M. B. Asif, and M. Sillanpää, "Understanding the factors affecting the adsorption of Lanthanum using different adsorbents: A critical review," *Chemosphere*, vol. 204, pp. 413–430, Aug. 2018, doi: 10.1016/j.chemosphere.2018.04.053.

[2] R. W. Herschy, "Water Quality for Drinking: WHO Guidelines," in *Encyclopedia of Earth Sciences Series*, 2012, pp. 876–883.

[3] T. A. Kurniawan, M. E. T. Sillanpää, and M. Sillanpää, "Nanoadsorbents for Remediation of Aquatic Environment: Local and Practical Solutions for Global Water Pollution Problems," *Crit. Rev. Environ. Sci. Technol.*, vol. 42, no. 12, pp. 1233–1295, Jun. 2012, doi: 10.1080/10643389.2011.556553.

[4] S. Afroze and T. K. Sen, "A Review on Heavy Metal Ions and Dye Adsorption from Water by Agricultural Solid Waste Adsorbents," *Water, Air, Soil Pollut.*, vol. 229, no. 7, p. 225, Jul. 2018, doi: 10.1007/s11270-018-3869-z.

[5] T. T. Bui, X. Q. Le, D. P. To, and V. T. Nguyen, "Investigation of typical properties of nanocrystalline iron powders prepared by ball milling techniques," *Adv. Nat. Sci. Nanosci. Nanotechnol.*, vol. 4, no. 4, p. 045003, Aug. 2013, doi: 10.1088/2043-6262/4/4/045003.

[6] R. A. Solano, A. P. Herrera, D. Maestre, and A. Cremades, "Fe-TiO 2 Nanoparticles Synthesized by Green Chemistry for Potential Application in Waste Water Photocatalytic Treatment," *J. Nanotechnol.*, vol. 2019, pp. 1–11, Jan. 2019, doi: 10.1155/2019/4571848.

[7] J. A. Castrillón Arango, A. A. Cristóbal, C. P. Ramos, P. G. Bercoff, and P. M. Botta, "Mechanochemical synthesis and characterization of nanocrystalline Ni1-xCoxFe2O4 (0 ≤

x ≤ 1) ferrites," *J. Alloys Compd.*, vol. 811, p. 152044, Nov. 2019, doi: 10.1016/j.jallcom.2019.152044.

[8] J. Hu, X. Geng, Y. Duan, W. Zhao, M. Zhu, and S. Ren, "Effect of Mechanical–Chemical Modification Process on Mercury Removal of Bromine Modified Fly Ash," *Energy & Fuels*, vol. 34, no. 8, pp. 9829–9839, Aug. 2020, doi: 10.1021/acs.energyfuels.0c01509.

[9] J. Jiang and J. Li, "Mechanically Induced N -arylation of Amines with Diaryliodonium Salts," *ChemistrySelect*, vol. 5, no. 2, pp. 542–548, Jan. 2020, doi: 10.1002/slct.201904188.

[10] J.-L. Do and T. Friščić, "Mechanochemistry: A Force of Synthesis," *ACS Cent. Sci.*, vol. 3, no. 1, pp. 13–19, Jan. 2017, doi: 10.1021/acscentsci.6b00277.

[11] C. M. Babu *et al.*, "Characterization of reduced graphene oxide supported mesoporous Fe2O3/TiO2 nanoparticles and adsorption of As(III) and As(V) from potable water," *J. Taiwan Inst. Chem. Eng.*, vol. 62, pp. 199–208, May 2016, doi: 10.1016/j.jtice.2016.02.005.

[12] D. La, T. Nguyen, L. Jones, and S. Bhosale, "Graphene-Supported Spinel CuFe2O4 Composites: Novel Adsorbents for Arsenic Removal in Aqueous Media," *Sensors*, vol. 17, no. 6, p. 1292, Jun. 2017, doi: 10.3390/s17061292.

[13] Z. Wei *et al.*, "The effect of pH on the adsorption of arsenic(III) and arsenic(V) at the TiO 2 anatase [1 0 1] surface," *J. Colloid Interface Sci.*, vol. 462, pp. 252–259, Jan. 2016, doi: 10.1016/j.jcis.2015.10.018.

[14] B. E. Monárrez-Cordero, P. Amézaga-Madrid, C. C. Leyva-Porras, P. Pizá-Ruiz, and M. Miki-Yoshida, "Study of the Adsorption of Arsenic (III and V) by Magnetite Nanoparticles Synthetized via AACVD," *Mater. Res.*, vol. 19, no. suppl 1, pp. 103–112, Dec. 2016, doi:

10.1590/1980-5373-mr-2015-0667.

[15] D. D. La, J. M. Patwari, L. A. Jones, F. Antolasic, and S. V. Bhosale, “Fabrication of a GNP/Fe–Mg Binary Oxide Composite for Effective Removal of Arsenic from Aqueous Solution,” *ACS Omega*, vol. 2, no. 1, pp. 218–226, Jan. 2017, doi: 10.1021/acsomega.6b00304.

[16] H. Hernández-Flores, N. Pariona, M. Herrera-Trejo, H. M. Hdz-García, and A. I. Mtz-Enriquez, “Concrete/maghemite nanocomposites as novel adsorbents for arsenic removal,” *J. Mol. Struct.*, vol. 1171, pp. 9–16, Nov. 2018, doi: 10.1016/j.molstruc.2018.05.078.

[17] A. I. A. Sherlala, A. A. A. Raman, M. M. Bello, and A. Buthiyappan, “Adsorption of arsenic using chitosan magnetic graphene oxide nanocomposite,” *J. Environ. Manage.*, vol. 246, no. January, pp. 547–556, Sep. 2019, doi: 10.1016/j.jenvman.2019.05.117.

[18] J.-S. Choi, L. P. Lingamdinne, J.-K. Yang, Y.-Y. Chang, and J. R. Koduru, “Fabrication of chitosan/graphene oxide-gadolinium nanorods as a novel nanocomposite for arsenic removal from aqueous solutions,” *J. Mol. Liq.*, vol. 320, p. 114410, Dec. 2020, doi: 10.1016/j.molliq.2020.114410.

[19] H. Liu, P. Li, F. Qiu, T. Zhang, and J. Xu, “Controllable preparation of FeOOH/CuO@WBC composite based on water bamboo cellulose applied for enhanced arsenic removal,” *Food Bioprod. Process.*, vol. 123, pp. 177–187, Sep. 2020, doi: 10.1016/j.fbp.2020.06.018.

[20] F. Beduk, “Superparamagnetic nanomaterial Fe 3 O 4 –TiO 2 for the removal of As(V) and As(III) from aqueous solutions,” *Environ. Technol.*, vol. 37, no. 14, pp. 1790–1801, Jul. 2016, doi: 10.1080/09593330.2015.1132777.

[21] M. B., R. Hernandez-Maya, M. Solís-López, C. Th-Th, and V. S., "Photocatalytic degradation of Orange G using TiO2/Fe3O4 nanocomposites," *J. Mater. Sci. Mater. Electron.*, vol. 29, no. 18, pp. 15436–15444, Sep. 2018, doi: 10.1007/s10854-018-9069-1.

[22] Z.-J. Li *et al.*, "Enhanced Photocatalytic Removal of Uranium(VI) from Aqueous Solution by Magnetic TiO 2 /Fe 3 O 4 and Its Graphene Composite," *Environ. Sci. Technol.*, vol. 51, no. 10, pp. 5666–5674, May 2017, doi: 10.1021/acs.est.6b05313.

[23] C. Y. Li, J. Bin Wang, and Y. Q. Wang, "Microstructure and photocatalytic activity of titanium dioxide nanoparticles," *Chinese Phys. B*, vol. 21, no. 9, pp. 1–5, 2012, doi: 10.1088/1674-1056/21/9/098102.

[24] R. Wang, X. Wang, X. Xi, R. Hu, and G. Jiang, "Preparation and Photocatalytic Activity of Magnetic Fe 3 O 4 /SiO 2 /TiO 2 Composites," *Adv. Mater. Sci. Eng.*, vol. 2012, pp. 1–8, 2012, doi: 10.1155/2012/409379.

[25] R. M. El-sherif, T. A. Lasheen, and E. A. Jebril, "Fabrication and characterization of CeO 2 -TiO 2 -Fe 2 O 3 magnetic nanoparticles for rapid removal of uranium ions from industrial waste solutions," *J. Mol. Liq.*, vol. 241, pp. 260–269, Sep. 2017, doi: 10.1016/j.molliq.2017.05.119.

[26] N. Sangiorgi, L. Aversa, R. Tatti, R. Verucchi, and A. Sanson, "Spectrophotometric method for optical band gap and electronic transitions determination of semiconductor materials," *Opt. Mater. (Amst).*, vol. 64, pp. 18–25, Feb. 2017, doi: 10.1016/j.optmat.2016.11.014.

[27] N. Nasralla *et al.*, "Structural and spectroscopic study of Fe-doped TiO2 nanoparticles prepared by sol-gel method," *Sci. Iran.*, vol. 20, no. 3, pp. 1018–1022, 2013, doi: 10.1016/j.scient.2013.05.017.

[28] B. Prajapati, S. Kumar, M. Kumar, S. Chatterjee, and A. K. Ghosh, “Investigation of the physical properties of Fe:TiO 2 -diluted magnetic semiconductor nanoparticles,” *J. Mater. Chem. C*, vol. 5, no. 17, pp. 4257–4267, 2017, doi: 10.1039/C7TC00233E.

[29] P. Z. Ray and H. J. Shipley, “Inorganic nano-adsorbents for the removal of heavy metals and arsenic: a review,” *RSC Adv.*, vol. 5, no. 38, pp. 29885–29907, 2015, doi: 10.1039/C5RA02714D.

[30] C. Kütahyali, Ş. Sert, B. Çetinkaya, S. Inan, and M. Eral, “Factors Affecting Lanthanum and Cerium Biosorption on Pinus brutia Leaf Powder,” *Sep. Sci. Technol.*, vol. 45, no. 10, pp. 1456–1462, Jun. 2010, doi: 10.1080/01496391003674266.

[31] A. Esposito, F. Pagnanelli, A. Lodi, C. Solisio, and F. Vegliò, “Biosorption of heavy metals by Sphaerotilus natans: an equilibrium study at different pH and biomass concentrations,” *Hydrometallurgy*, vol. 60, no. 2, pp. 129–141, Apr. 2001, doi: 10.1016/S0304-386X(00)00195-X.

[32] N. Das and D. Das, “Recovery of rare earth metals through biosorption: An overview,” *J. Rare Earths*, vol. 31, no. 10, pp. 933–943, Oct. 2013, doi: 10.1016/S1002-0721(13)60009-5.

[33] J. Xie, Y. Lin, C. Li, D. Wu, and H. Kong, “Removal and recovery of phosphate from water by activated aluminum oxide and lanthanum oxide,” *Powder Technol.*, vol. 269, pp. 351–357, Jan. 2015, doi: 10.1016/j.powtec.2014.09.024.

[34] M. Torab-Mostaedi, M. Asadollahzadeh, A. Hemmati, and A. Khosravi, “Biosorption of lanthanum and cerium from aqueous solutions by grapefruit peel: equilibrium, kinetic and thermodynamic studies,” *Res. Chem. Intermed.*, vol. 41, no. 2, pp. 559–573, Feb. 2015, doi:

10.1007/s11164-013-1210-4.

[35] D. Sinha and P. Prasad, “Health effects inflicted by chronic low-level arsenic contamination in groundwater: A global public health challenge,” *J. Appl. Toxicol.*, vol. 40, no. 1, pp. 87–131, Jan. 2020, doi: 10.1002/jat.3823.

[36] V. Srivastava, Y. C. Sharma, and M. Sillanpää, “Green synthesis of magnesium oxide nanoflower and its application for the removal of divalent metallic species from synthetic wastewater,” *Ceram. Int.*, vol. 41, no. 5, pp. 6702–6709, Jun. 2015, doi: 10.1016/j.ceramint.2015.01.112.

[37] S. Yadav, D. K. Tyagiand, and O. P. Yadav, “Equilibrium and kinetic studies on adsorption of Congo red dye from aqueous solution onto rice husk carbon,” *Nat. Environ. Pollut. Technol.*, vol. 10, no. 4, pp. 551–558, 2011.

[38] M. M. A. El-Latif, A. M. Ibrahim, M. S. Showman, and R. R. A. Hamide, “Alumina/Iron Oxide Nano Composite for Cadmium Ions Removal from Aqueous Solutions,” *Int. J. Nonferrous Metall.*, vol. 02, no. 02, pp. 47–62, 2013, doi: 10.4236/ijnm.2013.22007.

[39] P. Mondal, C. B. Majumder, and B. Mohanty, “Effects of adsorbent dose, its particle size and initial arsenic concentration on the removal of arsenic, iron and manganese from simulated ground water by Fe3+ impregnated activated carbon,” *J. Hazard. Mater.*, vol. 150, no. 3, pp. 695–702, Feb. 2008, doi: 10.1016/j.jhazmat.2007.05.040.

[40] B. Z. Can, R. Boncukcuoglu, A. E. Yilmaz, and B. A. Fil, “Effect of some operational parameters on the arsenic removal by electrocoagulation using iron electrodes,” *J. Environ. Heal. Sci. Eng.*, vol. 12, no. 1, p. 95, Dec. 2014, doi: https://doi.org/10.1007/s40097-021-00388-8.

[41] E. Weidner and F. Ciesielczyk, “Removal of Hazardous Oxyanions from the Environment Using Metal-Oxide-Based Materials,” *Materials (Basel).*, vol. 12, no. 6, p. 927, Mar. 2019, doi: 10.3390/ma12060927.

[42] M. Z. López Paraguay, J. A. Cortes, J. F. Pérez-Robles, and M. T. Alarcón-Herrera, “Adsorption of Arsenite from Groundwater Using Titanium Dioxide,” *CLEAN - Soil, Air, Water*, vol. 42, no. 6, pp. 713–721, Jun. 2014, doi: 10.1002/clen.201200489.

[43] D. Harikishore Kumar Reddy, K. Vijayaraghavan, J. A. Kim, and Y.-S. Yun, “Valorisation of post-sorption materials: Opportunities, strategies, and challenges,” *Adv. Colloid Interface Sci.*, vol. 242, pp. 35–58, Apr. 2017, doi: 10.1016/j.cis.2016.12.002.

[44] J. A. Gomes, M. S. Rahman, K. Das, S. Varma, and D. Cocke, “A Comparative Electrochemical Study on Arsenic Removal Using Iron, Aluminum, and Copper Electrodes,” *ECS Trans.*, vol. 25, no. 28, pp. 59–68, Dec. 2019, doi: 10.1149/1.3309678.

[45] R. Cornell and U. Schwertmann, “Colour Plates,” in *The Iron Oxides*, Wiley, 2003.

[46] Y. Wei *et al.*, “Deep oxidation and removal of arsenite in groundwater by rationally positioning oxidation and adsorption sites in binary Fe-Cu oxide/TiO2,” *Chem. Eng. J.*, vol. 354, no. July, pp. 825–834, Dec. 2018, doi: 10.1016/j.cej.2018.08.101.

[47] S. A. Chaudhry, M. Ahmed, S. I. Siddiqui, and S. Ahmed, “Fe(III)–Sn(IV) mixed binary oxide-coated sand preparation and its use for the removal of As(III) and As(V) from water: Application of isotherm, kinetic and thermodynamics,” *J. Mol. Liq.*, vol. 224, pp. 431–441, Dec. 2016, doi: 10.1016/j.molliq.2016.08.116.

[48] S. Lin, J. Jin, S. Sun, and J. Yu, “Removal of arsenic contaminants using a novel porous

nanoadsorbent with superior magnetic recovery," *Chem. Eng. Sci. X*, vol. 8, p. 100069, Nov. 2020, doi: 10.1016/j.cesx.2020.100069.

[49] T. Basu and U. C. Ghosh, "Influence of groundwater occurring ions on the kinetics of As(III) adsorption reaction with synthetic nanostructured Fe(III)–Cr(III) mixed oxide," *Desalination*, vol. 266, no. 1–3, pp. 25–32, Jan. 2011, doi: 10.1016/j.desal.2010.07.064.

[50] G. Zhang, Z. Ren, X. Zhang, and J. Chen, "Nanostructured iron(III)-copper(II) binary oxide: A novel adsorbent for enhanced arsenic removal from aqueous solutions," *Water Res.*, vol. 47, no. 12, pp. 4022–4031, Aug. 2013, doi: 10.1016/j.watres.2012.11.059.

[51] C. Zhang, C. Shan, Y. Jin, and M. Tong, "Enhanced removal of trace arsenate by magnetic nanoparticles modified with arginine and lysine," *Chem. Eng. J.*, vol. 254, pp. 340–348, Oct. 2014, doi: 10.1016/j.cej.2014.05.133.

[52] G. Ungureanu, S. Santos, R. Boaventura, and C. Botelho, "Arsenic and antimony in water and wastewater: Overview of removal techniques with special reference to latest advances in adsorption," *J. Environ. Manage.*, vol. 151, pp. 326–342, Mar. 2015, doi: 10.1016/j.jenvman.2014.12.051.

6. CHAPTER – 6 CONCLUSIONS AND PROSPECTS

6.1 General Conclusions

In order to enhance the photocatalytic activity of TiO_2 to the visible region spectrum, the three different ratios of $(TiO_2)_x (Fe_3O_4)_{1-x}$ (x = 0.2, 0.5, and 0.8) nanocomposites were synthesized by the ultrasonication method. From XRD and UV-Vis analysis, it was inferred that the increasing amount of the magnetite decreases both the crystallite size and the bandgap value of the synthesized nanocomposites. SEM analysis shows the surface morphology of the synthesized materials and the agglomerations of magnetite nanoparticles. The addition of TiO_2 decreases the aggregation of magnetite, and the addition of magnetite to TiO_2 decreases its bandgap and increases its efficiency to the visible region. It was observed from the degradation studies. Among the other ratios, the $(TiO_2)_{0.2}(Fe_3O_4)_{0.8}$ nanocomposite shows good photocatalytic activity for the Orange G because of its small crystallite size and low bandgap value compared to the other materials. But the magnetite phase is easily oxidized, which reduces its activity towards arsenic. Hence, both TiO_2 anatase and stable maghemite nanomaterials are synthesized by sol-gel and co-precipitation methods. The TiO_2 anatase nanoparticle with 14 nm and maghemite with 12nm were obtained. The presence of no secondary shows the purity of the synthesis.

The synthesized anatase and maghemite phases were used to form TiO_2/γ-Fe_2O_3 (T/M) nanocomposites using the facile mechano-chemical route. The important parameters which affect the nanomaterial properties, such as the BPR and milling time, were studied. XRD results showed the T/M NC with a BPR of 10:1 for both 2 and 6 h showed the presence of desired anatase and maghemite phases with the most intense peak ratio above 1.2, showing desirable performance in As removal. For 20:1 and 30:1 BPR with 2 hour milling time, some phase changes in the anatase and maghemite were observed.

For 20:1 and 30:1 BPR with 6 hour milling time, there is a complete phase change; the anatase phase was changed entirely to rutile, whereas the maghemite phase was changed entirely to hematite decreases the adsorption of arsenic. The Raman and UV-Vis analysis showed the same consistent behavior in accordance with XRD. XPS studies showed a decrease in binding energies and provided an indirect Ti–O-Fe bond formation. The adsorption studies showed above 50% removal of As (III) and ~ 90 % performance in the removal of As (V) using nanomaterials synthesized using a BPR of 10:1 for both 2 and 6 h, respectively. The T/M NCs with BPR 10:1 and 2 hour milling time are optimized as the best ratio.

The ratio of the titania and maghemite is an important parameter that determines the arsenic adsorption. Hence using the optimized BPR and milling time, five different ratios of TiO_2/γ-Fe_2O_3 (T/M) nanocomposites were synthesized using the facile ball-milling method. The XRD results show the desired anatase and maghemite peaks, whereas the morphological studies showed spherical particles and d-spacing values of 0.35 nm and 0.25 nm corresponding to the (101) and (311) planes belonging to the anatase TiO_2 and cubic γ-Fe_2O_3 phases. Increasing the maghemite content decreases the crystallite size, particle size, and bandgap of the nanocomposite and further supports the T/M nanocomposite formation. Among the other ratios, the T/M 5/5 ratio works well for both As (III) and (V). This is because increasing certain content maximum in nanocomposite results in agglomerations, which results in less arsenic removal. The sufficient incorporation of maghemite to arsenic reduces agglomerations and provides active sites to adsorb both As (III) and (V).

Hence an optimal T/M (5/5) NC ratio is employed for the adsorption studies focused on optimizing the factors which will affect arsenic removal, such as dosage, time, concentration, and pH. Increasing adsorbent dosage provides more adsorption sites which are increasing arsenic adsorption. At less time, the adsorption is maximum. Increasing time reduces the active sites of adsorbent, which reduces the arsenic adsorption. The pH, modifies the speciation of arsenic and modifies the adsorbent charges, which

enhances arsenic adsorption. For less arsenic concentration, the active sites were more, increasing the concentration of arenic decreases adsorption. The optimized results obtained by these studies for the effective removal of arsenic are adsorbent dosage 8g/L, contact time 15 minutes, pH-4, and concentration 2ppm. With these optimized conditions, 100% removal, below the WHOs recommended permissible concentration (0.01 ppm) for As (III) and (V) was reached. Further reusability test showed the synthesized NC offers additional advantages, the T/M NC are magnetic separable and reusable for several cycles and making it more economical for the water treatment. To the best of our knowledge, the obtained results presented in the study are novel. With some further studies, it can be implemented for large-scale industrial applications.

6.2 Future prospects

- With the promising outcomes obtained from the above studies, the future work is aimed to assess these nanoparticle systems to other heavy metals such as Cd, Pb, Cr, Cu, Hg, and Ni.
- The synthesized nanomaterials are planning to functionalize with non-conventional industrial waste materials, such as red clay and fly ash, to make them more cost-effective.
- Their adsorption properties of functionalized low-cost materials and their heavy metals removing studies are going to be studied.
- Incorporating all the results in the laboratory pilot plant and testing real water samples are the future plans of this work.

PUBLICATIONS AND CONFERENCES

Publications in peer-reviewed journals

- **Mercyrani Babudurai**, Onyekachi Nwakanma, Araceli Romero-Nunez, Ravichandran Manisekaran, Velumani Subramaniam, Homero Castaneda, Anish Jantrania. "Mechanical activation of TiO_2/Fe_2O_3 nanocomposite for arsenic adsorption: effect of ball-to-powder ratio and milling time" Journal of Nanostructure in Chemistry, https://doi.org/10.1007/s40097-021-00388-8
- **Mercyrani Babudurai**, Roberto Hernandez maya, Myriam solis lopez, Christeena Theresa Thomas, Velumani Subramaniam. "Photocatalytic degradation of Orange G using TiO_2/Fe_3O_4 nanocomposites", Journal of Materials Science: Materials in Electronics, September 2018, Volume 29, Issue 18, pp 15436–15444, https://doi.org/10.1007/s10854-018-9069-1

Article under preparation

- **Mercyrani Babudurai**, Karthick Sekar, Oneyekachi Nwakanma, Ravichandran Manisekaran, Velumani Subramaniam. "High-performance activity of magnetically separable TiO_2/Fe_2O_3 nano-adsorbent for effective removal of arsenic species."

Conference presentations

- **"ORGANIC COMPOUND DEGRADATION IN AQUEOUS PHASE BY THE USE OF TiO_2/Fe_3O_4 NANOCOMPOSITE HETEROSTRUCTURE"** held in XXVI International Materials Research Congress, Cancun, Mexico, from August (20 – 25) 2017.
- **"ARSENIC REMOVAL BY TiO_2/γ-Fe_2O_3 NANOCOMPOSITE OBTAINED BY BALL MILLING"** held in XXVIII International Materials Research Congress, Cancun, Mexico, from August (18 - 23), 2019.
- **"MECHANICAL ACTIVATION OF TiO_2/γ-Fe_2O_3 NANOCOMPOSITE FOR ARSENIC ADSORPTION"** held in Taller de Tratamiento de Aqua con Tecnologias Sustentables, CINVESTAV, Mexico, from August (25 - 26), 2020.
- **"EFFECT OF BPR AND MILLING TIME ON TiO_2/γ-Fe_2O_3 NANOCOMPOSITE FOR ARSENIC ADSORPTION"** held in International e-conference of advanced functional materials and optoelectronic devices, center for renewable energy, U.P, India from June (13 - 15), 2020. (online conference).